Preparation and magnetic properties of layered rare-earth ferrites

You Jin Kim

2020

Contents

Chapter 1: General introduction
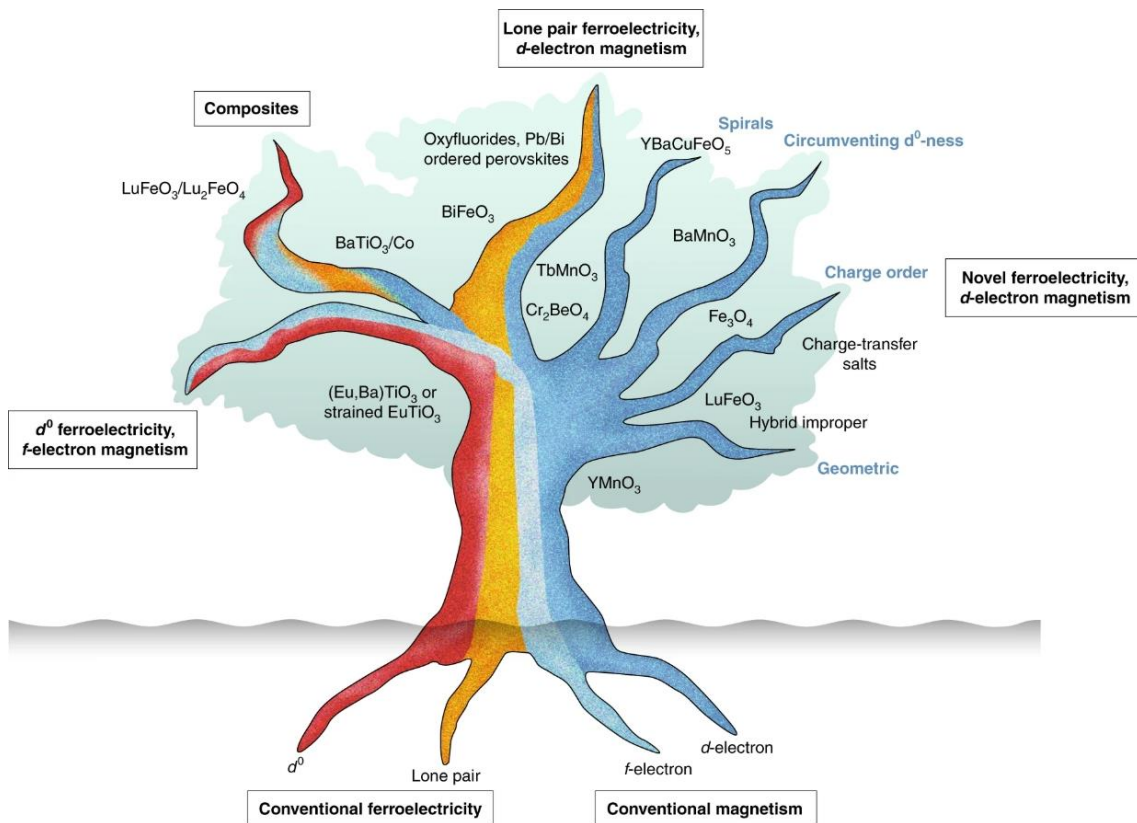
1.1 Multiferroics

The era of information technology (IT) has begun at the turn of the 20th century, and as a result, the request for the development of technology to achieve mass storage and fast processing of information is rapidly increasing.[1] In most conventional electronic devices, information is encoded as a form of electron charge, electric dipole and spin in specific materials, especially, in ferroelectric and ferromagnets. Ferroelectrics are the materials with a spontaneous electric polarization that can be reversed by an electric field.[2,3] On the other hand, Ferromagnets show stable and switchable spontaneous magnetization which stems from a quantum mechanical phenomenon, that is, an exchange interaction.[4] Recently, multiferroics, *i.e.*, materials which possess both dielectric and magnetic ordered structures, for instance, a combination of ferroelectricity and ferromagnetism, have attracted great attentions.

At the beginning of research, multiferroics have been limited to materials which exhibit two or more ferroic order parameters (ferroelectricity, ferromagnetism, and ferroelasticity, as illustrated in figure 1.1) in one phase.[5] However, the definition has been modified to include the non-primary magnetic ordering like antiferromagnetism (AFM) as well as composites of individual ferroics in recent years.[6] Among them, the combination of ferroelectric and magnetic properties holds promise for device architectures like next-generation memory and spin-transistor because even a single device component can perform more than one task, *i.e.*, electric (magnetic) fields control of magnetism

(dielectricity).[7,8] For this reason, searching for new multiferroic materials is one of the most important and epoch-making research topics. However, very few multiferroic materials exist due to their intrinsically mutual exclusive mechanism between ferroelectricity (favored by empty d-shell for the off-centering distortion of transition metal ions) and magnetism (favored by partially filled d-orbitals) in a conventional system.[9] In addition, even for the materials in which both properties are observed, the onset temperature of magnetoelectric (ME) coupling is substantially lower than room temperature.[6,9–12] To overcome this problem, recent developments have focused on the mechanism of improper ferroelectricity with conventional magnetism (Figure 1.2).[13] In the following, I briefly explain two ferroelectric origins, that is, proper and improper ferroelectricity.
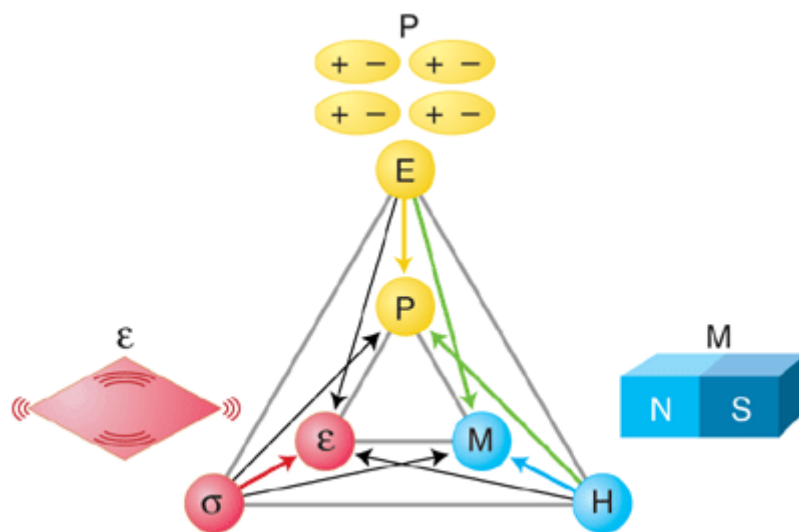
Figure 1.1. Phase control in ferroics and multiferroics. Each notation means that the electric field (E), magnetic field (H), stress (σ), electric polarization (P), magnetization (M), and strain (ε), respectively.[12]

Figure 1.2. Multiferroic family tree. Roots indicate the conventional mechanisms of ferroelectricity and magnetism, and branches are formed by combining and interweaving electronic origins in various ways from different roots.[13]

1.2 Origin of ferroelectricity in multiferroics

1.2.1 Proper ferroelectricity

Ferroelectricity stems from two primary origins: proper and improper ferroelectricity. Proper ferroelectricity is originated by the 'ferroelectric active' ions having empty d-orbital or $6s^2$ lone pair. However, because such ions do not possess magnetic moments magnetic property should be given by transition metal ions and/or rare-earth ions as observed for some materials like perovskite $BiFeO_3$ (BFO),[14] oxyfluorides such as $PbFeO_2F$ and $PbScO_2F$,[15–17] (Eu,Ba)TiO_3 alloys,[18] and strained $EuTiO_3$.[19] Among these compounds, BFO is considered as a prototypical multiferroic material where large spontaneous polarization and high Curie temperature (~90 μC cm^{-2}, T_c = 1103 K) are induced by the stereochemical activity of Bi^{3+} with $6s^2$ lone pair and the robust AFM (T_N = 643 K) is led by the 3d electrons of Fe^{3+} even above room temperature.[20] In other words, magnetism and ferroelectricity come independently from individual origins. The structure and physical properties of bulk BFO have been extensively studied,[21–24] and it is known that the cubic structure is rhombohedrally distorted ($a = b = c = 5.63$ Å, $\alpha = \beta = \gamma = 59.4°$) at room temperature. Apart from bulk forms, after the first report on a BFO thin film on an Si substrate made by Palkar et al.,[25] BFO thin films have been prepared and demonstrated to show substantially enhanced physical properties. For instance, a super-tetragonal 'T-like' structure has been observed as a stable phase with a huge spontaneous polarization of ~150 μC cm^{-2} along or close to the [001] direction under a large compressive strain (~-5 %).[26] Besides, under a biaxial tensile strain, an orthorhombic phase has been stabilized for a BFO thin film deposited on an $NdScO_3$ (110) substrate

and the thin films has proved a ferroelectric polarization within the in-plane direction.[27] These results indicate that the structure of BFO is sensitive to the strain induced by substrate structures and a change of structure leads to a drastic modification of physical properties. In addition to the ferroelectric and magnetic properties, nanostructured forms and nanoparticles of BFO exhibit other interesting and unprecedented physical behaviors such as the photovoltaic effect,[28] gas-sensing behavior,[29] photocatalysis,[30] and so on.

1.2.2 Improper ferroelectricity

Unlike the proper ferroelectrics, most improper ferroelectric materials manifest multiferroicity where the magnetic property depends on the conventional d-electron magnetism and the ferroelectricity is induced by an unconventional route to lift an inversion center. Hence, strong magnetoelectric coupling can be anticipated. These improper ferroelectric materials can be sorted by three origins, and details are as follows.

Geometrically driven multiferroics

For geometric ferroelectrics, a small A-cation in perovskite structures allows the rotation of its surrounding coordination polyhedra like $BaNiF_4$,[31] or collaboration with multiple nonpolar modes permits lattice distortion as in $YMnO_3$.[32,33] In these materials, the primary order parameter is the mode of rotation rather than the polar ferroelectric distortion. The anticipated advantage is that the polarization can be strongly coupled to the canted magnetic moments which are also induced by rotation and the observed magnitude of polarization is robust. In addition to the above-mentioned examples, so-

called hybrid improper ferroelectrics in layered perovskites can yield a net spontaneous polarization by the combination of non-polar rotations.[34–36] Meanwhile, the known geometrically ferroelectric materials which have been discovered so far show some difficulties. The first one is that ferroelectric domain switching is a challenge since the primary order parameter is the degree of rotational order rather than the ferroelectric polar distortion and the electric field is not a conjugate field for the polyhedral rotations. Also, the observed unusual domain structures might induce topological protection of domains that cannot be overcome by an appropriate conjugate field.[37,38] In this sense, the understanding of fundamental mechanism of polarization switching might be the next step for the development of application.

Magnetic ordering

A non-centrosymmetric magnetic ordering (some special magnetic orders like spin spiral structure) breaks the inversion symmetry and leads to spontaneous polarization. In other words, spin-orbit coupling and/or spin-lattice coupling induces the displacement of electron clouds and/or ions. A representative example having magnetic ordering is $TbMnO_3$.[39] In this compound, magnetic spirals are often stabilized by competition between the nearest- and next-nearest neighbor exchange interactions, and hence the ferroelectric transition temperature is always the same as the magnetic ordering temperature in this case. On the other hand, a new mechanism for stabilizing magnetic spirals has been recently proposed for a layered perovskite-related material $YBaCuFeO_5$[40], which shows relatively high multiferroic ordering temperature that is close to room

temperature. This mechanism may be effective for development of new multiferroic materials with transition temperatures higher than room temperature.

<u>Charge ordering</u>

Electronic ferroelectricity relies on the charge ordering (CO) of ions with different electronic configurations that manipulates magnetic and dielectric properties at the same time. Many transition metal ions possess multiple valence states within some special crystal lattices that make CO between two valence states. Typically, $LuFe_2O_4$[41] and Fe_3O_4 (magnetite)[42] are compounds in which CO determines physical properties including electrical conduction, dielectricity, and magnetism, although a problem as to what kinds of dielectric properties are governed by CO in $LuFe_2O_4$ is still controversial.[43] I focus on $LuFe_2O_4$ in the following part. On the other hand, magnetite is not appropriate for application of its multiferroic property because CO makes a small bandgap, high conductivity, and poor ferroelectric hysteresis.[44] In addition to these transition metal oxides, several organic charge-transfer complexes exhibit spin-induced electric polarization or ferroelectricity-induced spin alignment.[45] The coexistence of magnetic order and robust ferroelectric polarization near the room temperature in organic charge-transfer salts[46] or metal-organic frameworks[47] are also critical for the advancement in multiferroic materials via this mechanism.

1.3 Magnetoelectric coupling

Although the definition between magnetoelectirc (ME) coupling and multiferroics are

not completely the same (Figure 1.3),[8] the coupling between magnetism and ferroelectricity in multiferroic materials is the most important requisite for an application to new memory devices. Hence, in this section, I briefly discuss the ME effect. ME effect in a single-phase material is a linear effect that can be described by Landau theory.[48,49] When nonferroic materials are considered, free energy can be represented for an infinite, homogeneous, and stress-free medium by using the Einstein summation convention as follows:[8]

$$-F(E,H) = \frac{1}{2}\varepsilon_0\varepsilon_{ij}E_iE_j + \frac{1}{2}\mu_0\mu_{ij}H_iH_j + \alpha_{ij}E_iH_j$$

$$+ \frac{\beta_{ijk}}{2}E_iH_jH_k + \frac{\gamma_{ijk}}{2}H_iE_jE_k + \cdots, \qquad (1.1)$$

where F is the free energy of the present system, H_i is the applied magnetic field with i-th component, E_i is the applied electric field with i-th component, ε is the dielectric permittivity, μ is the magnetic susceptibility, and the tensors of α, β, and γ represent the n-th-order ME coefficients, respectively.

Using the present scheme, the polarization (P_i) and the magnetization (μ_0M_i) can be acquired by the differentiation of Equation 1.1.

$$P_i = \alpha_{ij}H_j + \frac{\beta_{ijk}}{2}H_jH_k + \cdots \qquad (1.2)$$

$$\mu_0M_i = \alpha_{ji}E_j + \frac{\gamma_{ijk}}{2}E_jE_k + \cdots \qquad (1.3)$$

Unlike the considered nonferroic materials, ferroic materials display field hysteresis and can be better parameterized. This is because the significant depolarizing and demagnetizing factors can be accountable in finite media, and also the coupling constant

might be a function of temperature alone. Actually, the resultant electric and magnetic

fields sometimes can be approximated by the magnetization and polarization,

respectively.[50]
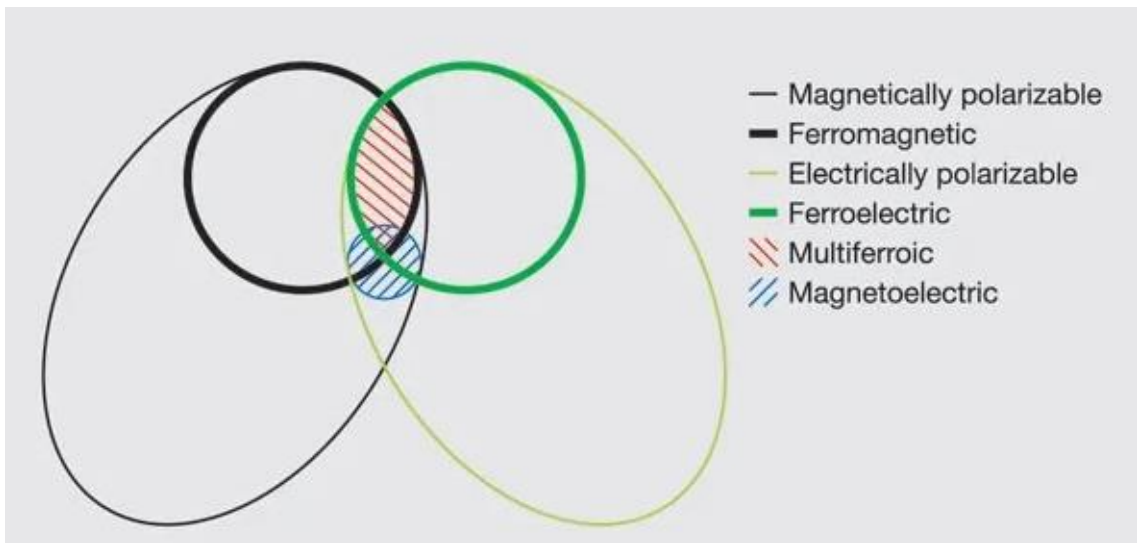
Figure 1.3. Relationship between multiferroic and magnetoelectric coupling.[8]

1.4 Layered rare-earth ferrites

There are many ABO_3-type transition metal oxides adopting the perovskite crystal structure, which is characterized by a small B-site cation at the center of an oxygen octahedron with a large A-site cation. Physical properties of most ABO_3 compounds reflect strong electronic correlation among A-site cation, B-site cation, and oxide ion. Especially, in ferroelectric materials, the spontaneous polarization is typically derived by a structural distortion to a lower-symmetry phase accompanied by a shift of a small cation at the Curie temperature (T_C).[51] However, a small A-site ion sometimes induces a change in crystal structure that is not a perovskite-type, and hence, physical properties are drastically altered as well. This is because the relative ratio of ionic radius among A-site cation, B-site cation, and oxide ion have influence on the crystal structure as naturally expected from the ionic model. To be more specific, the small radius of A-site cation might increase the degree of rotation of B-site octahedra and the distortion of crystal structure from cubic to lower symmetry, and the relation between ionic radii and crystal structure for ABO_3 compounds can be explained by using Goldschmidt tolerance factor as follows: $t = (r_A + r_O)/\sqrt{2}(r_B + r_O)$, where r_A, r_B, and r_O represent the ionic radii of A-site cation, B-site cation, and O^{2-}, respectively. The tolerance factor assesses whether or not the A-site cation can fit the cavity in the BO_6 framework and determines the crystal structure via the value of t. When $t = 1$, a perfect cubic structure is allowed, and the perovskite-type structures are generally formed in a range from 0.8 to 1. Meanwhile, when t is smaller than 0.8 or larger than 1, the alternative structures are adopted.[52,53]

1.4.1 Hexagonal RFeO₃ (R = Sc, Y, and Ho-Lu) compounds

As mentioned above, small A-site cations can generate different crystal structures from the distorted perovskite compounds. Representatively, hexagonal RMnO₃ (h-RMnO₃, R = rare-earth element) compounds correspond to this case and attract many interests due to their ferroelectric properties that coexist with magnetic behavior. In general, the structure of RMnO₃ depends on the radii of rare-earth elements. Orthorhombic RMnO₃ (o-RMnO₃) with *Pbnm* symmetry is possible for large R ionic radius (R = La-Dy),[4,54] and h-RMnO₃ allows for small R ionic radius (R = Sc, Y, and Ho-Lu) with $P6_3cm$ space group.[55–57] The o-RMnO₃ manifests the room temperature AFM with very weak electric polarization, while h-RMnO₃ has been anticipated as a promising multiferroic material due to the high-temperature ferroelectricy (T_C ~900 K) induced by their noncentrosymmetry with polar structure and the ME effect mediated by magnetoelastic coupling.[55–57] However, the onset temperature of magnetic ordering is much lower than room temperature (T_N ~below 100 K) since Mn^{3+} spins on the two-dimensional triangular lattices hinder the long-range magnetic ordering,[58,59] so that, h-RMnO₃ compounds are difficult to apply for a practical device.

Recent *ab initio* calculations suggested that the isostructural iron-based material (h-RFeO₃) might exhibit enhanced magnetic properties against the Mn-based counterparts due to the intensified correlation strength, larger magnetic moments in accordance with high-spin state of Fe^{3+} compared to Mn^{3+}, and the difference in the local electronic anisotropy.[60] Therefore, h-RFeO₃ is expected to manifest higher magnetization and magnetic ordering temperature, which are important for device applications. However,

unfortunately, the most stable phase of RFeO$_3$ belongs to the orthorhombic structure for all the rare-earth elements,[61,62] and o-RFeO$_3$ series are non-ferroelectric at room temperature like o-RMnO$_3$, except for the observed improper ferroelectricity in SmFeO$_3$.[63] To stabilize the metastable hexagonal phase, several preparation methods have been executed. They are a wet-chemical method,[64–67] under-cooling from a melt,[68–70] thin film growth on trigonal substrates,[71–74] and incorporation of dopants into either the R or Fe-sites.[75–77] Thus far, many studies have been mainly limited to h-LuFeO$_3$ thin films and only few reports dealt with a bulk form.

Crystal structure and ferroelectricity

When the ionic radius of R is small (R = Sc, Y, Ho-Lu), RFeO$_3$ crystallizes in a hexagonal structure with $P6_3cm$ space group at room temperature, as shown in Figure 1.4. The unit cell can be divided into two RO$_2$ layers and two FeO layers. In this structure, each R ion is surrounded by eight oxide ions, forming [RO$_8$] local environment. On the other hand, Fe ions are located on the triangular lattices and surrounded by five oxide ions, forming [FeO$_5$] trigonal bipyramids mutually connected on their two-dimensional corners. In connection with the triangular lattice structure, h-RFeO$_3$ experiences characteristic distortions that cause ferroelectricity.[32,60] The distortion leads to a tilting of the [FeO$_5$] bipyramid units and as a result, a mirror image disappears on the ab-plane. That is, the displacement of Fe ions along the c-axis results in spontaneous polarization. From a point of view of crystal symmetry, a $P6_3/mmc$ structure changes into $P6_3cm$ structure that is associated with three frozen phonon modes, Γ_2^-, K$_1$, and K$_3$ (in Figure 1.5)

14

around 1050 $\pm$ 50 K.[78] Among these modes, the K_3 mode corresponds to a collective

rotation of [FeO$_5$] trigonal bipyramids and a driving force for the structural transition that

is relevant to the nonzero displacement of Γ_2^- mode.[32,60] Thus, h-RFeO$_3$ belongs to

improper geometric ferroelectrics where the primary order parameter is a structural tilted

trimerization of [FeO$_5$] polyhedra.

Magnetic property

The magnetic moments of h-RFeO$_3$ mainly come from Fe^{3+} spins, and the effective

spin Hamiltonian can be represented as:

$$H = \sum_{ij} J_{ij} S_i \bullet S_j + \sum_{ij} D_{ij} \bullet S_i \times S_j + \sum_i S_i \bullet \widehat{\tau}_i \bullet S_i, \qquad (1.4)$$

where J_{ij} is the symmetric exchange interaction, D_{ij} is the Dzyaloshinskii-Moriya

(DM) antisymmetric exchange vectors, and $\widehat{\tau}_i$ is the single-ion anisotropy (SIA) tensor,

respectively.[60] The first term is related to the exchange interaction within Fe-O layer and

the interlayer interaction in neighboring Fe-O planes. When the spins are aligned along

the c-axis, the interaction is frustrated due to the two-dimensional triangular lattice

structure and the dominated AFM interaction between Fe sites. On the other hand, when

the frustration is lifted by the spin alignment within Fe-O plane, so-called 120° magnetic

ordering is generated like h-RFeO$_3$ system. In this structure, magnetic moments within

the same Fe-O layer collectively rotate in ab-plane with the degree of freedom (ϕ). As a

result of the spin alignments in one Fe-O layer with two independent directions ($\phi = 0$

and 90°) along with the mutual relation of spins between two neighboring Fe-O layers

with two different alignments (parallel and antiparallel), spins might follow four independent magnetic orderings (Γ_1 to Γ_4, see Figure 1.6).[75] Among these magnetic configurations, the Γ_2 ordering only allows a net magnetization along the *c*-axis. Other two terms of the Equation (1.4) are attributed to DM interaction and SIA tensor, which are induced by the [FeO$_5$] trimer distortion. Unlike the relatively well-studied ferroelectricity and structure of this material, the magnetic property still remains an open issue and the onset temperature of magnetic ordering is particularly controversial. Wang et al. suggested that the magnetic transition with Γ_2 structure occurs around 440 K based on the experimental result of *h*-LuFeO$_3$ thin film, which might be a candidate for the room temperature multiferroic compound.[73] However, Disseler et al. claimed that the observed 440 K transition corresponds to a structural transition and the real Néel temperature (T_N) is about 130 K allowing a complete AFM ordering with Γ_1 structure.[74] Therefore, there exists ambiguity on the magnetic ordering temperature and the study on spin configuration in thin film and bulk forms is now in progress.
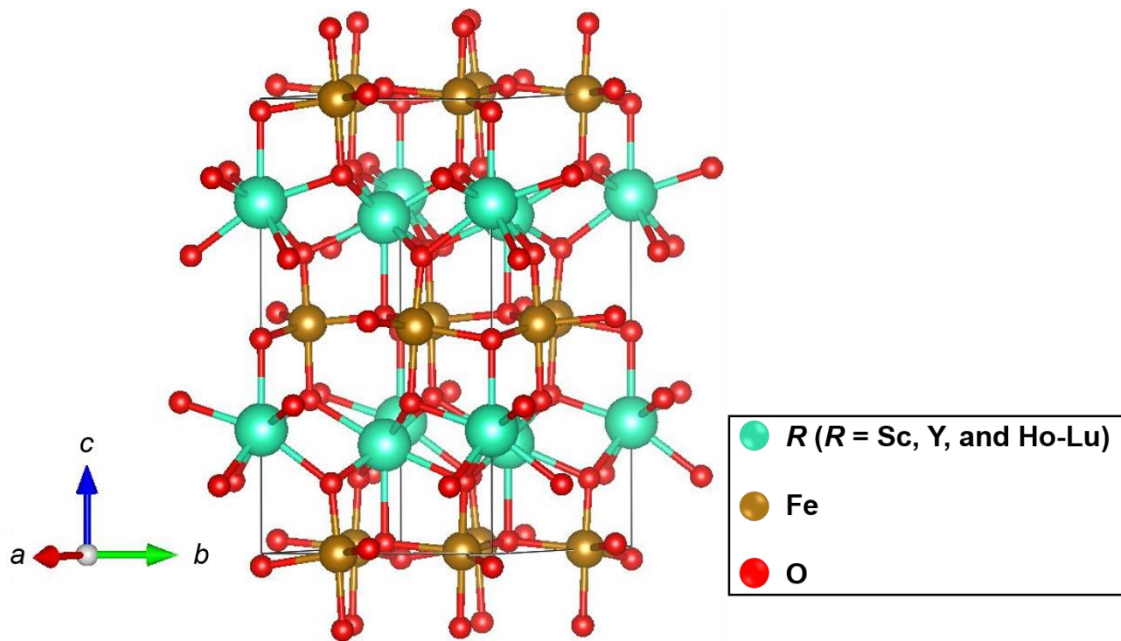
Figure 1.4. Unit cell of *h-R*FeO$_3$ (*R* = Sc, Y, and Ho-Lu) in a hexagonal setting.
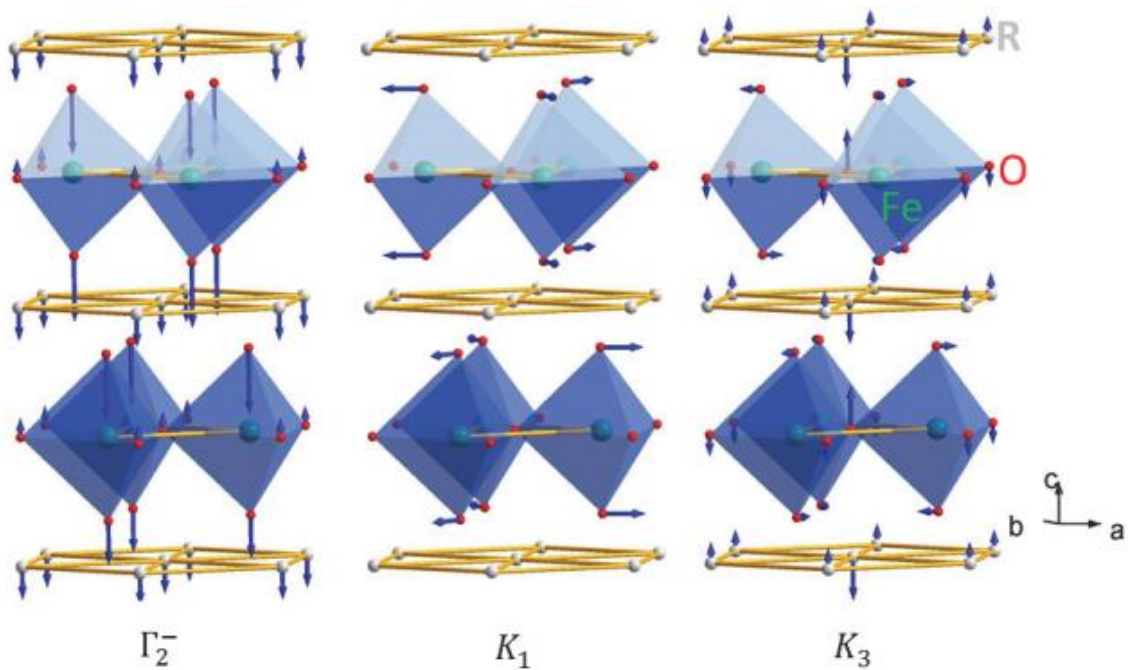
Figure 1.5. Illustration of three phonon modes (Γ_2^-, K$_1$, and K$_3$) that are related to the structural phase transition from *P6$_3$/mmc* to *P6$_3$cm*.[79]
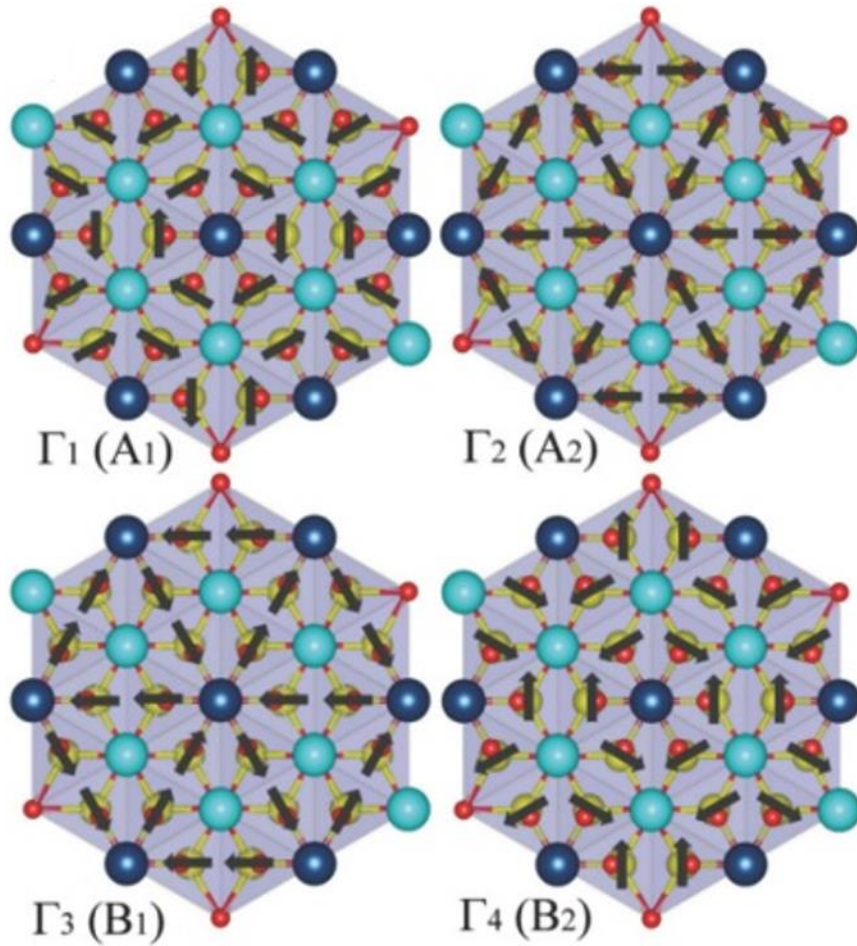
Figure 1.6. Four independent magnetic configurations of 120˚ magnetic orderings that are possible in h-RFeO$_3$ system.[76]

1.4.2 RFe$_2$O$_4$ (R = Sc, Y, In, and Dy to Lu) compounds

Among diverse multiferroics, RFe$_2$O$_4$ (R = Sc, Y, In, and Dy-Lu) compounds are one kind of prospective materials because of their unique dielectric and magnetic properties which emerge via mechanism based on the CO of the equal number of Fe^{2+} and Fe^{3+} ions, coupled with the spin degree of freedom.[41] Given that the structure is regarded as a hexagonal lattice, it has a similar structure with h-RFeO$_3$ compounds except that RFe$_2$O$_4$ is composed of [FeO$_5$] bilayers, which might be the origin of substantially different physical properties compared to h-RFeO$_3$ compound. As mentioned below, I briefly introduce the structure and physical properties of LuFe$_2$O$_4$ that is the most studied material in RFe$_2$O$_4$ compounds.

Crystal structure

Polycrystalline LuFe$_2$O$_4$ was first reported in 1974 by Kimizuka et al.,[80] who synthesized the compound under CO_2/H$_2$ mixed atmospheric condition, and the structural phase diagram at 1200 ℃ was established in 1976 by Sekine et al.[81] In this study, they suggested that the oxygen partial pressure during the sample preparation stage might affect oxygen stoichiometry, leading to LuFe$_2$O$_{4-\delta}$ composition. Afterward, the crystal structure was first clarified by Isobe et al.[82] in 1990 and the refinement result for a single-crystalline material indicates a rhombohedral $R3m$ symmetry that is illustrated in Figure 1.7 (a). The unit cell contains three sets of [FeO$_5$] bilayers that are separated by single [RO$_6$] layers along the c-axis and each atom of R, Fe, and O is located on triangular lattices within the ab-plane. This unusual atomic displacement causes charge and spin frustration

(Figure 1.8). The physical properties related to the frustrations are discussed below.

At the early stage of research on RFe_2O_4 compounds, the geometrical frustration of spins and relevant magnetic phenomena were the main topic for many researchers. In those processes, neutron diffraction was mainly used to determine the oxygen stoichiometry in RFe_2O_4 bulks. At room temperature, Bragg streak line (1/3 1/3 l) where l is a continuous value was observed for YFe_2O_4 single crystal, suggesting a two-dimensional spin correlation.[83] However, when the oxygen deficiencies were reduced to reach the stoichiometric composition, the streak line shrinks to a superlattice (1/3 1/3 1/2+3n), where n is an integer, which indicates the development of three-dimensional spin ordering. Furthermore, J. de Groot et al. performed single-crystal X-ray diffraction and observed (1/3 1/3 3/2)$_h$-type superlattice reflections from the superstructure. Two irreducible representations are allowed to explain the results of diffraction measurements, suggesting that the structure belongs to the space group of $C2/m$ which corresponds to antiferroelectrically stacked polar bilayers without a three-fold rotational symmetry.[43,84] (Figure 1.7 (b)). Contrary to the $C2/m$ interpretation, the result based on the group theory led to $P1$ or $C2$ symmetry that is the subgroup of $R3m$ symmetry.[85] Also, other space groups have been proposed to explain the CO structure in this compound. Thus, an issue as to which space group is correct still seems to be open.

Magnetic property

The magnetic properties of $LuFe_2O_4$ have been investigated using magnetization measurement, Mössbauer spectroscopy, and neutron diffraction method. In the report on

20

high magnetic field measurement at low temperatures, the observed saturation magnetic moment indicates a 2:1 ferrimagnetic spin structure with large coercive fields up to ~10 T and a firm magnetic anisotropy was related to Ising spin-like behavior along the c_{Hex} direction.[86,87] In addition, single-crystalline and polycrystalline $LuFe_2O_4$ bulk samples were reported to undergo a magnetic transition from paramagnetism to ferrimagnetism (or AFM) at T_N in a region between 220 and 240 K.[88,89] At this temperature, Fe spins show a strong preference to be aligned parallel to the c_{Hex}, which is perpendicular to the Fe-O bilayers, and three magnetic domains with 120° rotational symmetry are possible in the $R3m$ space group (Figure 1.9). Furthermore, $LuFe_2O_4$ is known to exhibit complicated magnetic properties like spin or cluster glass transition,[90–92] magnetostructural transition,[88] and competition between ferri- and AFM states[89] because of their frustrated spin structure and the oxygen off-stoichiometry.

In highly stoichiometric samples, three-dimensional spin correlations were observed along the c_{Hex}-axis with a second magnetic phase transition at T_{LT} ~170 K as shown in Figure 1.10. This phenomenon was accompanied by additional monoclinic lattice distortion and enhanced electric resistivity.[88] Also, high coercive fields to switch the magnetization direction were observed in low temperature regions. This phenomenon was explained as a kinetic arrest between two magnetic phases forming pancake-like spin clusters. Wu et al. suggested that the enhancement of coercivity was attributed to the collective freezing of Ising pancakes at low temperatures.[93] However, the underlying mechanism for giant coercivity and magnetostructural transition is still unclear. On the other hand, oxygen off-stoichiometric bulks brought about a disturbed magnetic long-

range ordering and a shrunk spin coherence along the c_{Hex}-axis. As a result, spin or cluster glass-like behaviors were observed by the competitive nature in multi-interactions among spins within triangular lattices.[90–92] Although many studies have been conducted in order to reveal the magnetic properties of these compounds, there still remain problems to be solved, especially, for compounds other than $LuFe_2O_4$ bulks.

<u>Dielectric property</u>

The ordering of Fe^{2+} and Fe^{3+} (Figure 1.11) was estimated based on the neutron diffraction result in the 1990s and the studies suggested a $\sqrt{3} \times \sqrt{3}$ structure that corresponds to the formation of superlattice cell along the (1 1 0) direction enlarged by three-times compared to a chemical unit cell.[94] The temperature dependence of neutron diffraction revealed that the superlattice reflection preserved up to 330 K. On top of that, transmission electron microscopy (TEM) observation also provided the structural information; a diffuse streak of (1/3 1/3 *l*) was observed below about 500 K, indicating the formation of two-dimensional CO within the *ab*-plane of Fe-O bilayers. Further cooling to 330 K, the coherence length of ordering develops along the c_{Hex}-axis is corresponding to the formation of three-dimensional CO.[95,96] In other words, the signal of TEM can be interpreted as a lattice distortion so that the observed results can be expected to consider as an indication of the CO of iron ions.

As for the ferroelectric properties, the existence of spontaneous polarization arising from the CO of Fe ions rather than ion displacement is a new and interesting subject. Ikeda et al. performed pyroelectric current measurements (Figure 1.12) that confirm the

spontaneous electric polarization dependent on the direction of the applied electric field ($\pm$10 kV/cm).[41] However, detailed CO mechanism and a problem as to whether or not this material is really ferroelectric is still controversial because the precise chemical control of the sample quality is not very simple. In particular, the estimation of stoichiometry like deficient or excess ions is an additional issue because the defects largely affect the physical properties. Also, measurements on electric polarization in leaky materials are not so easy to carry out. For instance, the significantly large dielectric constant reported previously might arise from a Schottky barrier and depletion layer formed between the contact electrodes and the surface of the sample.[97–99] Recently, it was reported that the intrinsic dielectric constants of $R\text{Fe}_2\text{O}_4$ are considered to be 40-100 at room temperature. In addition, the symmetry has been reconsidered, and non-polar $C2$ or $C2/m$ for the antiferroelectric state[43,84] or $P1$ or Cm for the polar CO state[85] have been proposed as the low-temperature CO phase. In this regard, the observation of electric polarization and searching for the ground state of charge- and spin-ordered $R\text{Fe}_2\text{O}_4$ might help in resolving much confusion.
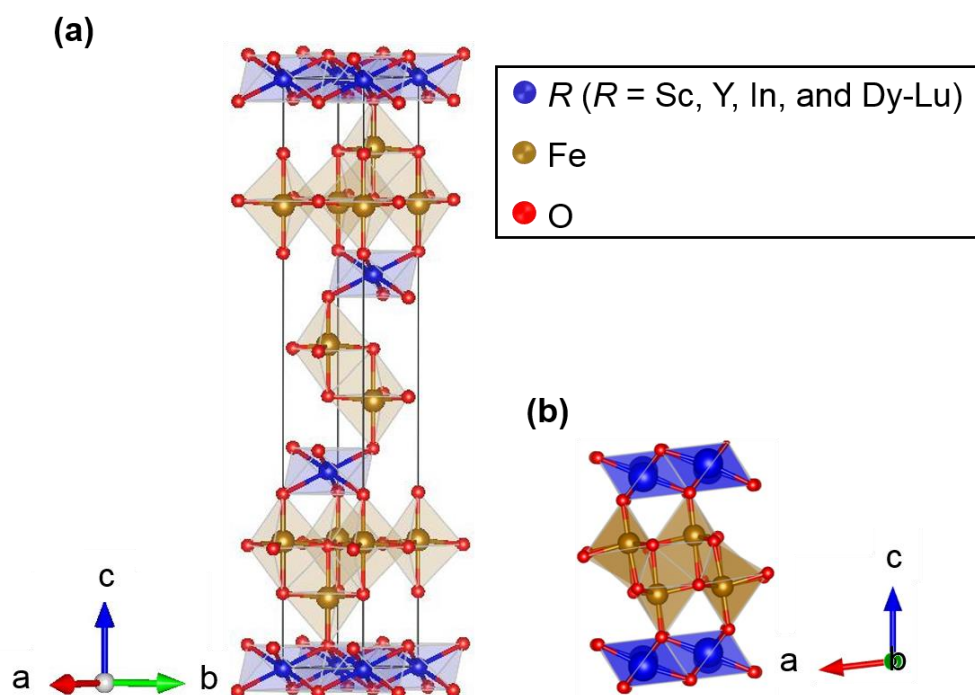
Figure 1.7. (a) $R3m$ crystal symmetry of $R\mathrm{Fe_2O_4}$ in a hexagonal setting. (b) Monoclinic $C2/m$ structure model for the charge-ordered state of $\mathrm{LuFe_2O_4}$
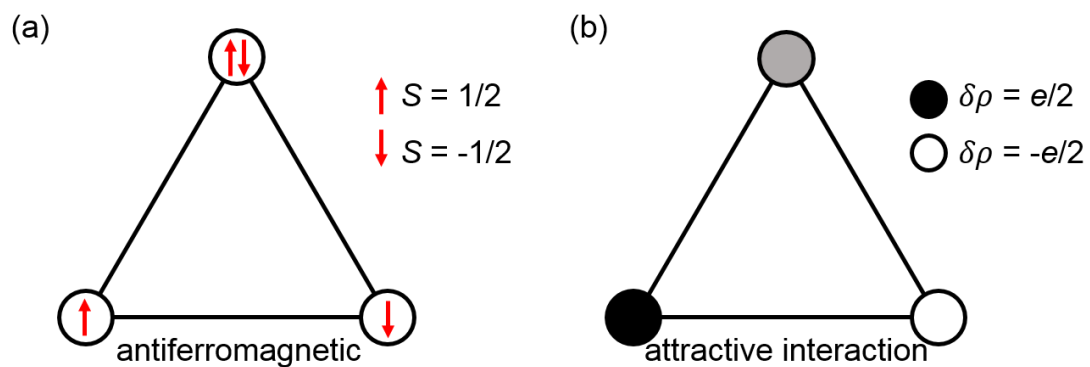
Figure 1.8. Spin and charge frustration in a triangular lattice containing equal number of $\mathrm{Fe^{2+}}$ and $\mathrm{Fe^{3+}}$. (a) spin frustration, (b) charge frustration
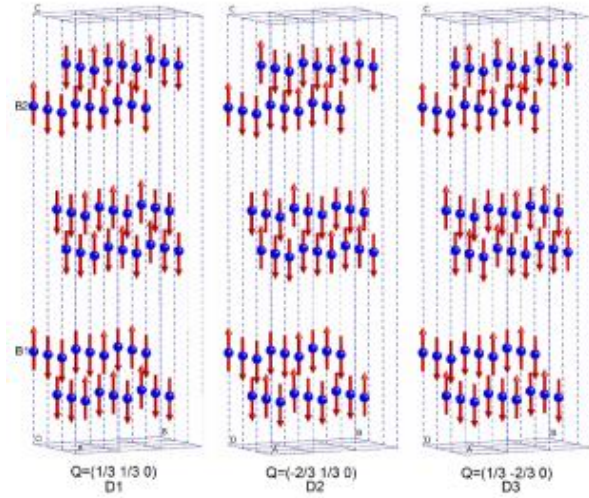
Figure 1.9. Ferrimagnetic spin structure with three domains below T_N ~220 K in $R\bar{3}m$ crystal symmetry, proposed by Christianson et al.[88]
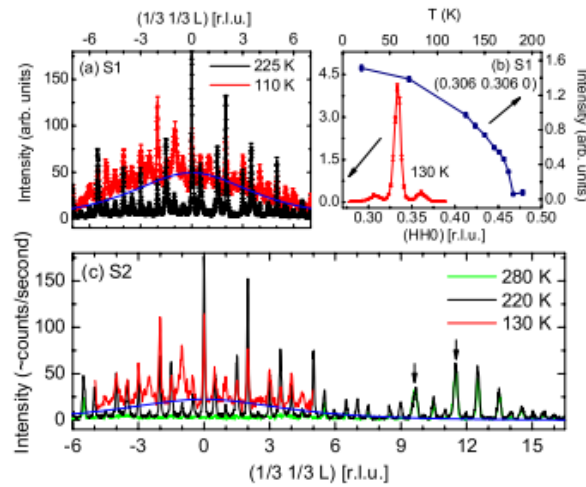
Figure 1.10. (a) and (c) indicates the neutron scattering scans along (1/3 1/3 l) for sample 1 and 2 (S1 and S2). Here, S1 and S2 denote two crystalline samples obtained from the same growth batch. The arrows originate from the aluminum background scattering. (b) The observed new set of satellites that is indexed by $(\frac{1}{3} \pm \delta, \frac{1}{3} \pm \delta, \frac{3}{2})$ with $\delta = 0.027$ below T_{LT}.[88]
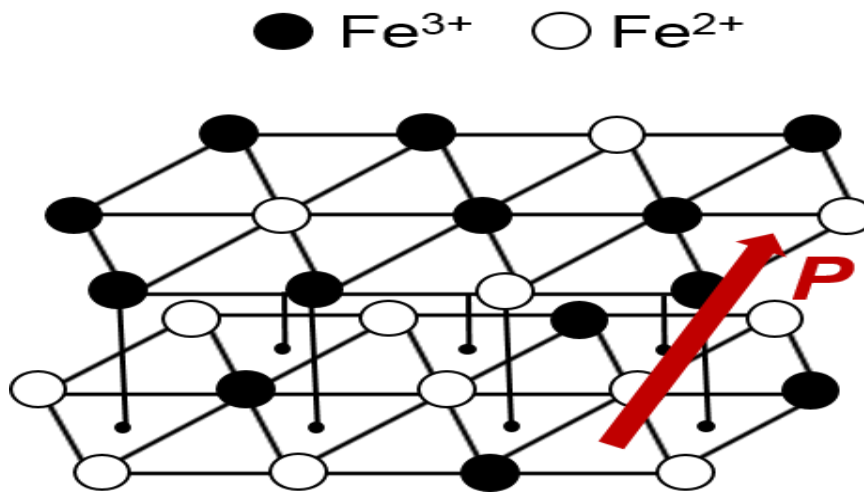
Figure 1.11. Schematic diagram of polar Fe^{2+}/Fe^{3+} charge order configuration within Fe-O bilayers. The spontaneous polarization (P) exists along the c_{Hex} direction.
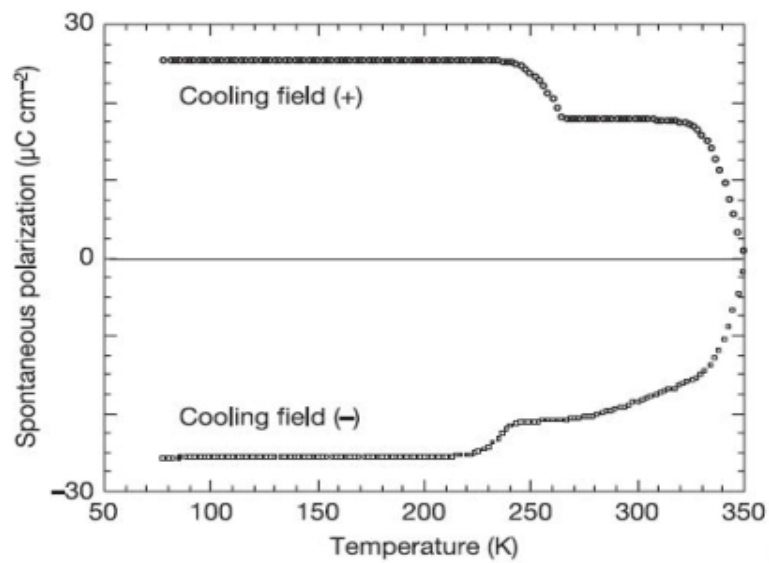
Figure 1.12. Temperature dependence of electric polarization for single-crystalline $LuFe_2O_4$.[41]

1.5. Composite multiferroics

Multiferroic material in a single phase is especially appealing not only due to the properties of both parent compounds but also due to the anticipated additional functionalities induced by the interaction between the magnetic and electric polarization. However, attempts to discover multiferroics that combine ferroelectricity and magnetic properties in the same phase have proved highly difficult and the reported single-phase multiferroics are not suitable for applications until now because most of them cannot combine large and robust electric and magnetic polarization at room temperature. In order to circumvent the observed difficulties, two-phase composite multiferroics that consist of ferroelectric and magnetic components have been examined as an alternative approach. Although the origin of single-phase multiferroics is restricted to the crystal symmetry or constraints associated with the presence of magnetism and ferroelectricity,[9] the composite structures can lift most of constraints since the different order parameters need not coexist in the same phase. In such composite structures, substantially large ME effect might be expected if the composites have large surface area or particularly, features induced by the ferroelastic constituents.[12] Although there are various designs for composite structures,[100–103] I briefly discuss only the multilayered structure in this chapter.

From a fundamental viewpoint, the effect of strain between magnetic ultrathin films and ferroelectric substrates has been studied and two advantages such as better control over crystal structure and near-perfect mechanical coupling have been highlighted. Actually, oxide interfaces in thin film forms give rise to curious phenomena, including

colossal magnetoresistance, high-temperature superconductivity, and improved ME coupling via designing at the atomic-scale, and are important from a point of view of fundamental to applications.[104] For example, a strain due to misfit in $BiFeO_3$ epitaxial thin film leads to an enhanced magnetic and electric polarizations whose magnitude might be associated with the density of ferroelectric domain walls (Figure 1.13).[20] In addition, many other materials, such as $CoFe_2O_4$,[105] $SrRuO_3$,[106] Fe_3O_4,[107–109] and $La_{1-x}A_xMnO_3$ (A = Ca, Sr),[110–112] also showed the modulated magnetic or ferroelectric properties by the strain effect. On top of the single-phase thin film, a recent report on layer-by-layer growth of atomic-scale multiferroic superlattices consisting of two phases, one of which is a ferroelectric and AFM h-$LuFeO_3$ and the other is a ferrimagnetic and polar $LuFe_2O_4$, exhibited multiferroic property above room temperature as shown in Figure 1.14.[103] This discovery provides tremendous opportunities because there are many combinations of suitable crystal structures and chemistries. Vertically aligned nanocomposites (Figure 1.15) are also attractive since their three-dimensional heteroepitaxy can provide the enhanced coupling between dielectric and magnetic polarization thanks to large interface area as well as intensified coercive fields owing to the nanostructures.[113]
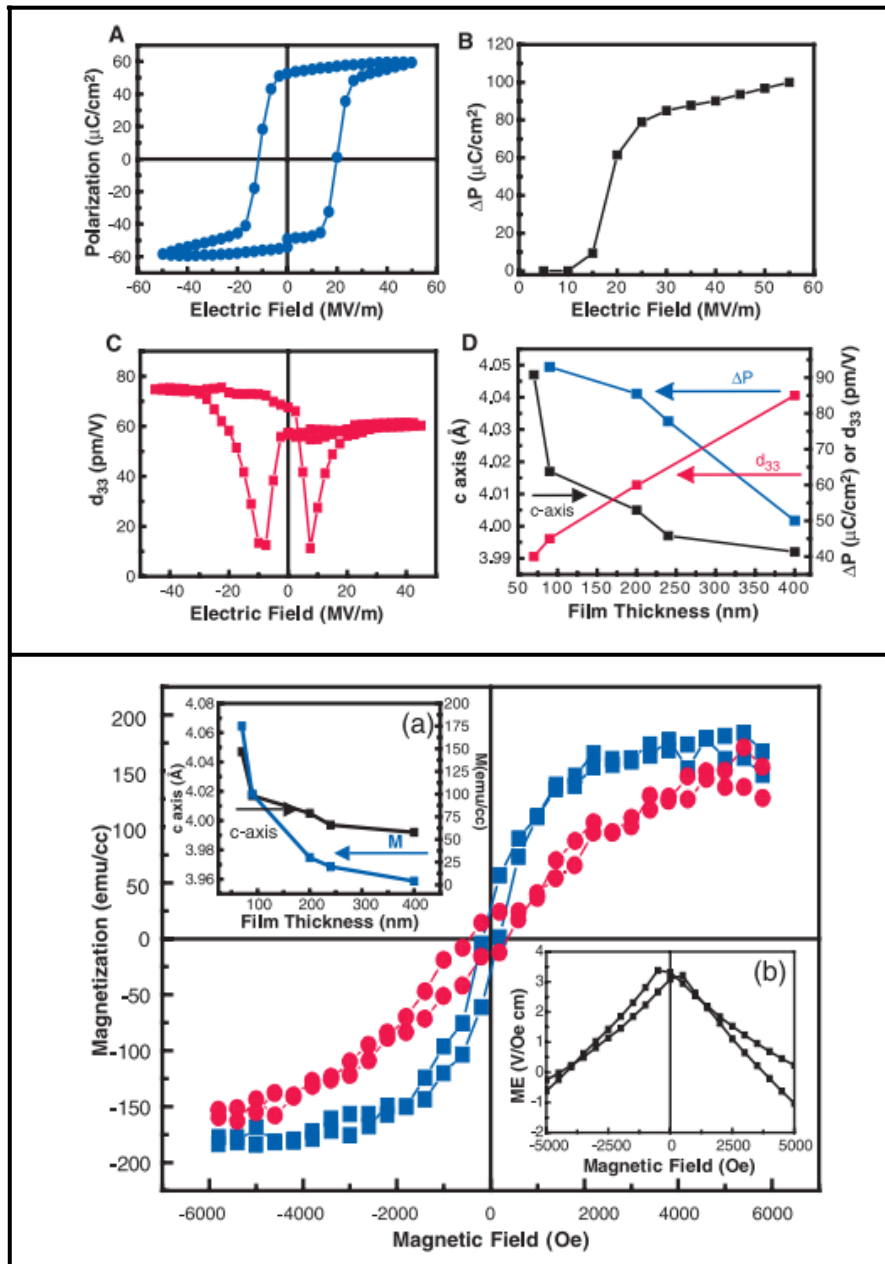
Figure 1.13. Enhanced ferroelectric and piezoelectric responses (upper) and magnetization (bottom) in BiFeO$_3$ epitaxial thin film on SrTiO$_3$ substrate.[20]
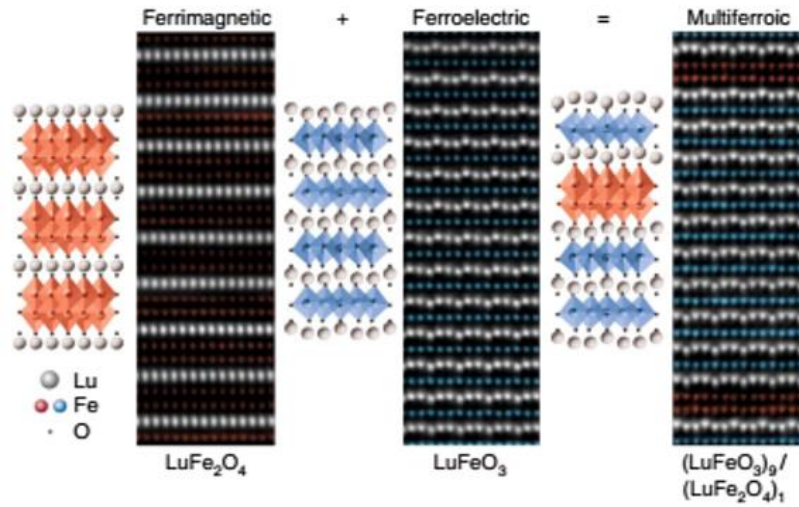
Figure 1.14. An example of horizontal composites that consist of ferroelectric and ferro- or ferrimagnetic materials. In this case, h-LuFeO$_3$ and LuFe$_2$O$_4$ have been used for layer-by-layer growth.[103]
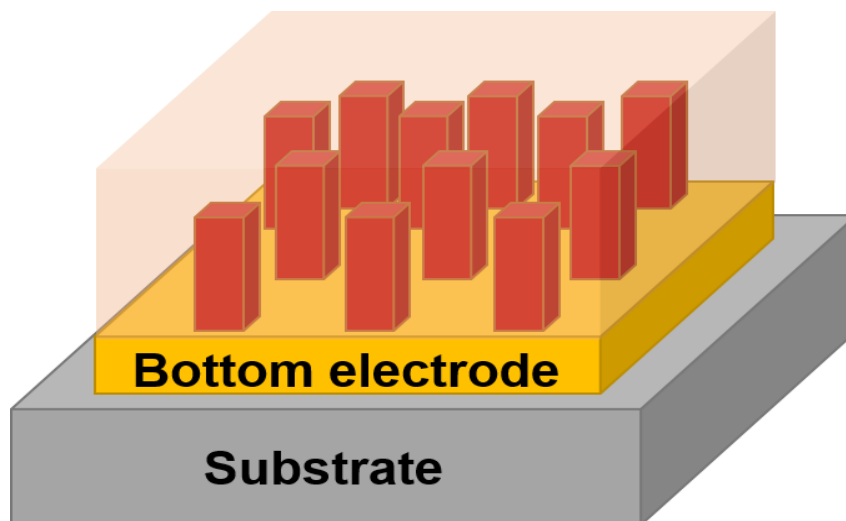
Figure 1.15. Schematic structure of vertically aligned nanocomposites formed by ferro/ferrimagnet embedded in ferroelectric matrix with three-dimensional coherent heteroepitaxy.

1.6. Outline of this thesis

In this thesis, I have investigated magnetic properties of layered rare-earth ferrites, especially $R\text{Fe}_2\text{O}_4$ (R = Lu, Tm) and h-TmFeO_3. I prepared thin films as well as bulk forms of those compounds. The outline of the present thesis is as follows.

In chapter 1, I start from the general theoretical background for explaining various phenomena related to multiferroics, the mechanism of proper and improper ferroelectricity, and magnetoelectric coupling. In addition, a brief introduction of layered rare-earth ferrites and multilayered structure as a composite multiferroic material, that is the main subject of the present thesis, is given as well.

In chapter 2, epitaxial growth of LuFe_2O_4 thin film and its magnetic and electrical properties are described. The thin film was grown on yttria-stabilized zirconia (YSZ) substrate by a pulsed laser deposition method. An unusual very thin self-assembled interface structure, which consists of h-LuFeO_3 and $\text{Lu}_2\text{Fe}_3\text{O}_7$-like compositions with LuFe_2O_4 main phase, was observed by high-resolution scanning transmission electron microscopy. The observed interfacial structure manifests the exchange bias effect at 100 K, which might be induced by the spin competition between different types of magnetic materials. Also, the LuFe_2O_4 thin film itself shows the spin glass transition that is also observed in bulk LuFe_2O_4 with off-stoichiometric amount of oxygen. The electronic transport behavior of the present thin film changes from the Arrhenius-type to variable range hopping schemes at around the three-dimensional CO temperature.[114]

In chapter 3, the fabrication of epitaxial $TmFe_2O_4$ thin film on YSZ substrate using the pulsed laser deposition method and its magnetic properties are described. The structure of the interface between $TmFe_2O_4$ and YSZ was investigated by scanning transmission electron microscopy and electron energy loss spectroscopy. As a result, hexagonal $TmFeO_{3-\delta}$ (h-$TmFeO_{3-\delta}$) phase has been observed at the interface with Tm^{3+}-rich region at the upper side of the substrate and a possible growth mechanism can be suggested based on the structural analysis. Furthermore, $TmFe_2O_4$ phase itself shows spin or cluster glass transition and the coexistence between glassy $TmFe_2O_4$ and AFM h-$TmFeO_{3-\delta}$ leads to the intrinsic exchange bias effect, which is demonstrated by field-cooled hysteresis and training effect, at 100 K. On the other hand, the glassy behavior was verified by the fact that the effect of external dc magnetic field ono the irreversible transition temperature can be interpreted in terms of de Almeida-Thouless line and that the aging-memory effect was clearly observed.[115]

In chapter 4, the preparation of single-crystalline $TmFe_2O_{4-\delta}$ with oxygen vacancies and its magnetic properties, especially spin glass transition, are discussed. $TmFe_2O_{4-\delta}$ was grown by an optical floating zone melting method and the c_{Hex}-plane of the single crystal was detected through a Laue camera. In order to investigate the magnetic properties, I executed the measurements of dc and ac magnetic susceptibilities and confirmed the re-entrant spin glass phase transition in terms of the dynamic scaling law that is based on the result of the frequency dependence of spin-freezing temperature. Furthermore, the aging-memory and rejuvenation effect is also observed below spin-freezing temperature. This

fact indicates that the oxygen vacancies might enhance the magnetic frustration among iron ions coupled by AFM interactions and as a result, the spin glass phase transition has occurred after the ferrimagnetic transition with lowering temperature.[116]

In chapter 5, the structural, dielectric, and magnetic properties of nanocrystalline h-TmFeO$_3$ are mentioned. Single phase h-TmFeO$_3$ nanoparticles were synthesized by a citrate sol-gel method, and the metastable hexagonal phase with a polar $P6_3cm$ space group was successfully obtained. The temperature dependence of dc magnetic susceptibility shows an AFM ordering below T_N which is about 120 K. Mössbauer spectrum manifests a single doublet with an isomer shift corresponding to the value for Fe^{3+} (S = 5/2). In addition, a clear anomaly in the dielectric constant was observed near T_N, which indicates the presence of magnetoelectric coupling below this temperature.

Finally, conclusions derived in the present investigation are described in the chapter of summary.

References in chapter 1

1. G. A. Prinz, *Science*, 1998, **282**, 1660–1663.

2. W. Prellier, M. P. Singh and P. Murugavel, *J. Phys. Condens. Matter*, 2005, **17**, R803.

3. M. E. Lines and A. M. Glass, *Principles and applications of ferroelectrics and related materials*, Oxford university press, 2001.

4. T. Kimura, T. Goto, H. Shintani, K. Ishizaka, T. Arima and Y. Tokura, *Nature*, 2003, **426**, 55–58.

5. H. Schmid, *Ferroelectrics*, 1994, **162**, 317–338.

6. M. Fiebig, *J. Phys. D. Appl. Phys.*, 2005, **38**, R123.

7. R. Ramesh and N. A. Spaldin, *Nat. Mater.*, 2007, **6**, 21–29.

8. W. Eerenstein, N. D. Mathur and J. F. Scott, *Nature*, 2006, **442**, 759–765.

9. N. A. Hill, *J. Phys. Chem. B*, 2000, **104**, 6694–6709.

10. S. M. Skinner, *IEEE Trans. Parts, Mater. Packag.*, 1970, **6**, 68–90.

11. G. A. Smolenskii and I. E. Chupis, *Sov. Phys. Usp.*, 1982, **25**, 415–448.

12. N. A. Spaldin and M. Fiebig, *Science*, 2005, **309**, 391–392.

13. N. A. Spaldin and R. Ramesh, *Nat. Mater.*, 2019, **18**, 203–212.

14. I. Sosnowska, T. P. Neumaier and E. Steichele, *J. Phys. C Solid State Phys.*, 1982, **15**, 4835–4846.

15. Y. Inaguma, J.-M. Greneche, M.-P. Crosnier-Lopez, T. Katsumata, Y. Calage and J.-L. Fourquet, *Chem. Mater.*, 2005, **17**, 1386–1390.

16. A. Simon and J. Ravez, *Ferroelectrics*, 1980, **24**, 305–307.

17. T. Katsumata, M. Nakashima, H. Umemoto and Y. Inaguma, *J. Solid State Chem.*, 2008, **181**, 2737–2740.

18. K. Z. Rushchanskii, S. Kamba, V. Goian, P. Vaněk, M. Savinov, J. Prokleška, D. Nuzhnyy, K. Knžek, F. Laufek, S. Eckel, M. Ležaić and N. A. Spaldin, *Nat. Mater.*, 2010, **9**, 649–654.

19. J. H. Lee, L. Fang, E. Vlahos, X. Ke, Y. W. Jung, L. F. Kourkoutis, J.-W. Kim, P. J. Ryan, T. Heeg, M. Roeckerath, E. Johnston-Halperin and D. G. Schlom, *Nature*, 2010, **466**, 954–958.

20. J. Wang, J. B. Neaton, H. Zheng, V. Nagarajan, S. B. Ogale, B. Liu, D. Viehland, V. Vaithyanathan, D. G. Schlom, U. V. Waghmare, M. Wuttig and R. Ramesh, *Science*, 2003, **299**, 1719–1722.

21. R. Haumont, P. Bouvier, A. Pashkin, K. Rabia, S. Frank, B. Dkhil, W. A. Crichton, C. A. Kuntscher and J. Kreisel, *Phys. Rev. B*, 2009, **79**, 184110.

22. J. B. Neaton, C. Ederer, U. V. Waghmare, N. A. Spaldin and K. M. Rabe, *Phys. Rev. B*, 2005, **71**, 014113.

23. P. Ravindran, R. Vidya, A. Kjekshus, H. Fjellvåg and O. Eriksson, *Phys. Rev. B*, 2006, **74**, 224412.

24. P. Hermet, M. Goffinet, J. Kreisel and P. Ghosez, *Phys. Rev. B,* 2007, **75**, 220102.

25. V. R. Palkar, J. John and R. Pinto, *Appl. Phys. Lett.*, 2002, **80**, 1628–1630.

26. H. Béa, B. Dupé, S. Fusil, R. Mattana, E. Jacquet, B. Warot-Fonrose, F. Wilhelm, A. Rogalev, S. Petit, V. Cros, M. Bibes and A. Barthélémy, *Phys. Rev. Lett.*, 2009, **102**, 217603.

27. J. C. Yang, Q. He, S. J. Suresha, C. Y. Kuo, C. Y. Peng, R. C. Haislmaier, M. A. Motyka, G. Sheng, C. Adamo, H. J. Lin, R. Ramesh and Y. H. Chu, *Phys. Rev. Lett.*, 2012, **109**, 247606.

28. T. Choi, S. Lee, Y. J. Choi, V. Kiryukhin and S.-W. Cheong, *Science*, 2009, **324**, 63–66.

29. S. D. Waghmare, V. V. Jadhav, S. K. Gore, S.-J. Yoon, S. B. Ambade, B. J. Lokhande, R. S. Mane and S.-H. Han, *Mater. Res. Bull.*, 2012, **47**, 4169–4173.

30. T. Gao, Z. Chen, Q. Huang, F. Niu, X. Huang, L. Qin and Y. Huang, *Rev. Adv. Mater. Sci.*, 2015, **40**, 97–109.

31. D. L. Fox and J. F. Scott, *J. Phys. C: Solid State Phys.*, 1977, **10**, L329.

32. C. J. Fennie and K. M. Rabe, *Phys. Rev. B*, 2005, **72**, 100103.

33. Z. Huang, Y. Cao, Y. Sun, Y. Xue and C. Chu, *Phys. Rev. B*, 1997, **56**, 2623–2626.

34. E. Bousquet, M. Dawber, N. Stucki, C. Lichtensteiger, P. Hermet, S. Gariglio, J.-M. Triscone and P. Ghosez, *Nature*, 2008, **452**, 732–736.

35. N. A. Benedek and C. J. Fennie, *Phys. Rev. Lett.*, 2011, **106**, 107204.

36. N. A. Benedek, J. M. Rondinelli, H. Djani, P. Ghosez and P. Lightfoot, *Dalt. Trans.*, 2015, **44**, 10543–10558.

37. T. Choi, Y. Horibe, H. T. Yi, Y. J. Choi, W. Wu and S.-W. Cheong, *Nat. Mater.*, 2010, **9**, 253–258.

38. W. Wu, Y. Horibe, N. Lee, S.-W. Cheong and J. R. Guest, *Phys. Rev. Lett.*, 2012, **108**, 077203.

39. R. Kajimoto, H. Yoshizawa, H. Shintani, T. Kimura and Y. Tokura, *Phys. Rev. B*,

2004, **70**, 012401.

40. M. Morin, A. Scaramucci, M. Bartkowiak, E. Pomjakushina, G. Deng, D. Sheptyakov, L. Keller, J. Rodriguez-Carvajal, N. A. Spaldin, M. Kenzelmann, K. Conder and M. Medarde, *Phys. Rev. B*, 2015, **91**, 064408.

41. N. Ikeda, H. Ohsumi, K. Ohwada, K. Ishii, T. Inami, K. Kakurai, Y. Murakami, K. Yoshii, S. Mori, Y. Horibe, Y. Horibe and H. Kitô, *Nature*, 2005, **436**, 1136–1138.

42. M. S. Senn, J. P. Wright and J. P. Attfield, *Nature*, 2012, **481**, 173–176.

43. J. De Groot, T. Mueller, R. A. Rosenberg, D. J. Keavney, Z. Islam, J.-W. Kim and M. Angst, *Phys. Rev. Lett.*, 2012, **108**, 187601.

44. M. Alexe, M. Ziese, D. Hesse, P. Esquinazi, K. Yamauchi, T. Fukushima, S. Picozzi and U. Gösele, *Adv. Mater.*, 2009, **21**, 4452–4455.

45. S. Ren and M. Wuttig, *Adv. Mater.*, 2012, **24**, 724–727.

46. P. Lunkenheimer, J. Müller, S. Krohns, F. Schrettle, A. Loidl, B. Hartmann, R. Rommel, M. De Souza, C. Hotta, J. A. Schlueter, J. A. Schlueter and M. Lang, *Nat. Mater.*, 2012, **11**, 755–758.

47. A. Stroppa, P. Barone, P. Jain, J. M. Perez-Mato and S. Picozzi, *Adv. Mater.*, 2013, **25**, 2284–2290.

48. H. Schmid, *Ferroelectrics*, 1994, **161**, 1–28.

49. J.-P. Rivera, *Ferroelectrics*, 1994, **161**, 165–180.

50. T. Lottermoser, T. Lonkai, U. Amann, D. Hohlwein, J. Ihringer and M. Fiebig, *Nature*, 2004, **430**, 541–544.

51. R. E. Cohen and H. Krakauer, *Ferroelectrics*, 1992, **136**, 65–83.

52. H. L. Yakel, *Acta Crystallogr.*, 1955, **8**, 394–398.

53. H. L. Yakel Jnr, W. C. Koehler, E. F. Bertaut and E. F. Forrat, *Acta Crystallogr.*, 1963, **16**, 957–962.

54. E. Hanamura and Y. Tanabe, *Phase Transitions*, 2006, **79**, 957–971.

55. B. B. Van Aken, T. T. M. Palstra, A. Filippetti and N. A. Spaldin, *Nat. Mater.*, 2004, **3**, 164–170.

56. A. A. Belik, T. Furubayashi, Y. Matsushita, M. Tanaka, S. Hishita and E. Takayama-Muromachi, *Angew. Chem. Int. Ed. Engl.*, 2009, **48**, 6117–6120.

57. H. Lueken, *Angew. Chem. Int. Ed. Engl.*, 2008, **47**, 8562–8564.

58. T. Katsufuji, S. Mori, M. Masaki, Y. Moritomo, N. Yamamoto and H. Takagi, *Phys. Rev. B*, 2001, **64**, 1044191–1044196.

59. T. Katsufuji, M. Masaki, A. Machida, M. Moritomo, K. Kato, E. Nishibori, M. Takata, M. Sakata, K. Ohoyama, K. Kitazawa, K. Kitazawa and H. Takagi, *Phys. Rev. B*, 2002, **66**, 1344341–1344348.

60. H. Das, A. L. Wysocki, Y. Geng, W. Wu and C. J. Fennie, *Nat. Commun.*, 2014, **5**, 1-11.

61. R. L. White, *J. Appl. Phys.*, 1969, **40**, 1061–1069.

62. M. Marezio, J. P. Remeika and P. D. Dernier, *Acta Crystallogr. B*, 1970, **26**, 2008–2022.

63. J.-H. Lee, Y. K. Jeong, J. H. Park, M.-A. Oak, H. M. Jang, J. Y. Son and J. F. Scott, *Phys. Rev. Lett.*, 2011, **107**, 117201.

64. J. Li, U. G. Singh, T. D. Schladt, J. K. Stalick, S. L. Scott and R. Seshadri, *Chem.*

Mater., 2008, **20**, 6567–6576.

65. S. Hosokawa, H.-J. Jeon, S. Iwamoto and M. Inoue, *J. Am. Ceram. Soc.*, 2009, **92**, 2847–2853.

66. L. J. Downie, R. J. Goff, W. Kockelmann, S. D. Forder, J. E. Parker, F. D. Morrison and P. Lightfoot, *J. Solid State Chem.*, 2012, **190**, 52–60.

67. P. Suresh, K. Vijaya Laxmi, A. K. Bera, S. M. Yusuf, B. L. Chittari, J. Jung and P. S. Anil Kumar, *Phys. Rev. B*, 2018, **97**, 184419.

68. K. Nagashio and K. Kuribayashi, *J. Am. Ceram. Soc.*, 2002, **85**, 2550–2556.

69. K. Kuribayashi and M. S. V. Kumar, *J. Phys.: Conf. Ser.*, 2011, **327**, 1-10.

70. E. Magome, C. Moriyoshi, Y. Kuroiwa, A. Masuno and H. Inoue, *Jpn. J. Appl. Phys.*, 2010, **49**, 09ME06.

71. A. A. Bossak, I. E. Graboy, O. Y. Gorbenko, A. R. Kaul, M. S. Kartavtseva, V. L. Svetchnikov and H. W. Zandbergen, *Chem. Mater.*, 2004, **16**, 1751–1755.

72. Y. K. Jeong, J.-H. Lee, S.-J. Ahn, S.-W. Song, H. M. Jang, H. Choi and J. F. Scott, *J. Am. Chem. Soc.*, 2012, **134**, 1450–1453.

73. W. Wang, J. Zhao, W. Wang, Z. Gai, N. Balke, M. Chi, H. N. Lee, W. Tian, L. Zhu, X. Cheng, J. Shen and X. Xu, *Phys. Rev. Lett.*, 2013, **110**, 237601.

74. S. M. Disseler, J. A. Borchers, C. M. Brooks, J. A. Mundy, J. A. Moyer, D. A. Hillsberry, E. L. Thies, D. A. Tenne, J. Heron, M. E. Holtz, D. G. Schlom and W. D. Ratcliff, *Phys. Rev. Lett.*, 2015, **114**, 217602.

75. A. Masuno, A. Ishimoto, C. Moriyoshi, N. Hayashi, H. Kawaji, Y. Kuroiwa and H. Inoue, *Inorg. Chem.*, 2013, **52**, 11889–11894.

76. J. Liu, T. L. Sun, X. Q. Liu, H. Tian, T. T. Gao and X. M. Chen, *Adv. Funct. Mater.*, 2018, **28**, 1706062.

77. L. Lin, H. M. Zhang, M. F. Liu, S. Shen, S. Zhou, D. Li, X. Wang, Z. B. Yan, Z. D. Zhang, J. Zhao, S. Dong and J.-M. Liu, *Phys. Rev. B*, 2016, **93**, 075146.

78. A. S. Gibbs, K. S. Knight and P. Lightfoot, *Phys. Rev. B*, 2011, **83**, 094111.

79. X. Xu and W. Wang, *Mod. Phys. Lett. B*, 2014, **28**, 1430008.

80. N. Kimizuka, A. Takenaka, Y. Sasada and T. Katsura, *Solid State Commun.*, 1974, **15**, 1321–1323.

81. T. Sekine and T. Katsura, *J. Solid State Chem.*, 1976, **17**, 49–54.

82. M. Isobe, N. Kimizuka, J. Iida and S. Takekawa, *Acta Crystallogr. C*, 1990, **46**, 1917–1918.

83. J. Akimitsu, Y. Inada, K. Siratori, I. Shindo and N. Kimizuka, *Solid State Commun.*, 1979, **32**, 1065–1068.

84. J. Bourgeois, M. Hervieu, M. Poienar, A. M. Abakumov, E. Elkaïm, M. T. Sougrati, F. Porcher, F. Damay, J. Rouquette, G. Van Tendeloo, J. Haines and C. Martin, *Phys. Rev. B*, 2012, **85**, 064102.

85. M. Iwata and Y. Ishibashi, *J. Phys. Soc. Jpn.,* 2012, **81**, 035003.

86. J. Iida, S. Kakugawa, G. Kido, Y. Nakagawa, S. Takekawa and N. Kimizuka, *Physica B: Condens. Matter*, 1989, **155**, 307–310.

87. J. Iida, Y. Nakagawa, S. Takekawa and N. Kimizuka, *J. Phys. Soc. Jpn*, 1987, **56**, 3746–3747.

88. A. D. Christianson, M. D. Lumsden, M. Angst, Z. Yamani, W. Tian, R. Jin, E. A.

Payzant, S. E. Nagler, B. C. Sales and D. Mandrus, *Phys. Rev. Lett.*, 2008, **100**, 107601.

89. J. De Groot, K. Marty, M. D. Lumsden, A. D. Christianson, S. E. Nagler, S. Adiga, W. J. H. Borghols, K. Schmalzl, Z. Yamani, S. R. Bland, Y. Su and M. Angst, *Phys. Rev. Lett.*, 2012, **108**, 037206.

90. F. Wang, J. Kim, Y.-J. Kim and G. D. Gu, *Phys. Rev. B*, 2009, **80**, 024419.

91. M. H. Phan, N. A. Frey, H. Srikanth, M. Angst, B. C. Sales and D. Mandrus, *J. Appl. Phys.*, 2009, **105**, 07E308.

92. M. H. Phan, N. A. Frey, M. Angst, J. de Groot, B. C. Sales, D. G. Mandrus and H. Srikanth, *Solid State Commun.*, 2010, **150**, 341–345.

93. W. Wu, V. Kiryukhin, H.-J. Noh, K.-T. Ko, J.-H. Park, W. Ratcliff, P. A. Sharma, N. Harrison, Y. J. Choi, Y. Horibe, C. L. Zhang and S.-W. Cheong, *Phys. Rev. Lett.*, 2008, **101**, 137203.

94. K. Siratori, in *Proc. 6th Int. Conf. on Ferrites; The Japan Society of Powder and Powder Metallurgy*, 1992, 703.

95. Y. Yamada, S. Nohdo and N. Ikeda, *J. Phys. Soc. Jpn.*, 1997, **66**, 3733–3736.

96. Y. Yamada, K. Kitsuda, S. Nohdo and N. Ikeda, *Phys. Rev. B*, 2000, **62**, 12167–12174.

97. P. Ren, Z. Yang, W. G. Zhu, C. H. A. Huan and L. Wang, *J. Appl. Phys.*, 2011, **109**, 074109.

98. A. Ruff, S. Krohns, F. Schrettle, V. Tsurkan, P. Lunkenheimer and A. Loidl, *Eur. Phys. J. B*, 2012, **85**, 290.

99. D. Niermann, F. Waschkowski, J. De Groot, M. Angst and J. Hemberger, *Phys. Rev. Lett.*, 2012, **109**, 016405.

100. C. A. F. Vaz, J. Hoffman, C. H. Ahn and R. Ramesh, *Adv. Mater.*, 2010, **22**, 2900–2918.

101. M. Avellaneda and G. Harshé, *J. Intell. Mater. Syst. Struct.*, 1994, **5**, 501–513.

102. J. H. Park, M. G. Kim, S.-J. Ahn, S. Ryu and H. M. Jang, *J. Magn. Magn. Mater.*, 2009, **321**, 1971–1974.

103. J. A. Mundy, C. M. Brooks, M. E. Holtz, J. A. Moyer, H. Das, A. F. Rébola, J. T. Heron, J. D. Clarkson, S. M. Disseler, Z. Liu, D. A. Muller and D. G. Schlom, *Nature*, 2016, **537**, 523–527.

104. J. Mannhart and D. G. Schlom, *Science*, 2010, **327**, 1607–1611.

105. R. V. Chopdekar and Y. Suzuki, *Appl. Phys. Lett.*, 2006, **89**, 182506.

106. M. K. Lee, T. K. Nath, C. B. Eom, M. C. Smoak and F. Tsui, *Appl. Phys. Lett.*, 2000, **77**, 3547–3549.

107. M. Ziese, A. Bollero, I. Panagiotopoulos and N. Moutis, *Appl. Phys. Lett.*, 2006, **88**, 212502.

108. H. F. Tian, T. L. Qu, L. B. Luo, J. J. Yang, S. M. Guo, H. Y. Zhang, Y. G. Zhao and J. Q. Li, *Appl. Phys. Lett.*, 2008, **92**, 1–4.

109. C. A. F. Vaz, J. Hoffman, Y. Segal, F. J. Walker and C. H. Ahn, *Proceedings of SPIE - The International Society for Optical Engineering*, 2010, 7760.

110. D. Dale, A. Fleet, J. D. Brock and Y. Suzuki, *Appl. Phys. Lett.*, 2003, **82**, 3725–3727.

111. K. Dörr, C. Thiele, J.-W. Kim, O. Bilani, K. Nenkov and L. Schultz, *Philos. Mag. Lett.*, 2007, **87**, 269–278.

112. W. Eerenstein, M. Wiora, J. L. Prieto, J. F. Scott and N. D. Mathur, *Nat. Mater.*,

2007, **6**, 348–351.

113. H. Zheng, J. Wang, S. E. Lofland, Z. Ma, L. Mohaddes-Ardabili, T. Zhao, L. Salamanca-Riba, S. R. Shinde, S. B. Ogale, F. Bai, A. Roytburd and R. Ramesh, *Science* , 2004, **303**, 661–663.

114. Y. J. Kim, S. Konishi, Y. Hayasaka, I. Kakeya and K. Tanaka, *CrystEngComm*, 2020, **22**, 1096–1105.

115. Y. J. Kim, S. Konishi, Y. Hayasaka, R. Ota, R. Tomozawa and K. Tanaka, *J. Mater. Chem. C*, 2020 (in press).

116. Y. J. Kim, S. Konishi, M. Okada, M. Komabuchi, D. Urushihara, T. Asaka and K. Tanaka, *J. Phys.: Condens. Matter*, 2020, **32**, 405801.

Chapter 2: Magnetic and electrical properties of LuFe$_2$O$_4$ epitaxial thin films with self-assembled interface structure

2.1 Introduction

Multiferroics, which possess more than one ferroic order parameters in a single-phase, have attracted a great deal of attention due to their unique physical properties.[1-3] In particular, materials with ferroelectricity and ferro- or ferrimagnetism have been vigorously searched for owing to their potential applications to new memory devices and data storage systems.[2] RFe$_2$O$_4$ (R = Sc, Y, In and Dy to Lu) is regarded as a multiferroic material where ferroelectricity or antiferroelectricity is thought to be induced by the CO among Fe^{2+} and Fe^{3+} ions, which inevitably has influence on the ordering of magnetic moments of Fe ions.[3, 4] The crystal structure, when viewed as a hexagonal system, is characterized by alternate stacking of iron-containing bilayers separated by [RO$_2$] monolayers along the c-axis[5](Figure 2.1 (a)). In this structure, Fe ions construct a triangular lattice, leading to the geometrical charge and spin frustrations. Among the RFe$_2$O$_4$ compounds, bulk LuFe$_2$O$_4$ materials have been most extensively explored for their diverse physical properties such as magnetism, electrical transport, and dielectricity.[6-11] For LuFe$_2$O$_4$, a two-dimensional CO (2D-CO) among Fe^{2+} and Fe^{3+} ions develops below 500 K, which is recognized by (1/3 1/3 l)$_h$-type superlattice reflections. With further decreasing temperature, a three-dimensional CO (3D-CO) emerges below about 320 K.[12, 13] In this temperature regime, the presence of finite polarization was suggested on the basis of resonant X-ray scattering and pyroelectric measurements.[6] On

the other hand, the localized magnetic moments of Fe ions induce ferrimagnetic or antiferromagnetic properties below Néel temperature of about 220-240 K,[6] and a transition with lattice distortion is observed at 175 K.[14] Below this temperature, both charge and spin ordered states are frozen, and consequently, the superstructure with $\sqrt{3} \times \sqrt{3}$ CO is stabilized.[10] In the overall magnetic transition process, Fe spins are treated by the Ising model, since the magnetic properties exhibit strong anisotropy along the *c*-axis. Furthermore, magnetic and dielectric properties are found to be very sensitive to defects relevant to oxygen and/or iron. For the magnetic properties, glassy nature was observed for the compound with off-stoichiometric oxygen ratio due to the shorten spin coherence length reflected by the two-dimensional pancake-like spin domain.[14-17] For the dielectric properties, oxygen vacancies are thought to give rise to leakage current often observed when an attempt was made to measure polarization under electric field. This is one of the main reasons why the dielectric ground state of $LuFe_2O_4$ has not been established yet.[18-20]

In addition to the extensive studies of physical properties for $LuFe_2O_4$ bulk forms, there exist several reports on thin films of $LuFe_2O_4$. In previous studies, epitaxial *c*-axis oriented $LuFe_2O_4$ thin films were grown on various substrates such as yttria-stabilized zirconia (YSZ) (111), MgO (111), sapphire (0001), ZnO (001), $MgAl_2O_4$ (111), and 6H-SiC (001) via diverse deposition methods.[23-26] Nonetheless, the reports on $LuFe_2O_4$ thin films are much less than those on bulk $LuFe_2O_4$. In particular, magnetic properties of $LuFe_2O_4$ thin films have been little investigated except for the work performed by Brooks et al,[25] They indicated that $LuFe_2O_4$ thin films deposited on SiC, $MgAl_2O_4$, and MgO

substrates showed hysteresis loops at 100 K in the magnetization versus magnetic field relations and that both magnetization and coercive force largely depended on the kinds of substrate materials. Moreover, multilayers based on $LuFe_2O_4$ are expected to manifest intriguing magnetic and dielectric properties never achieved in a single-phase thin film. Mundy et al. synthesized $(LuFeO_3)_m/(LuFe_2O_4)_n$ superlattices and indicated that they could tune the magnetic phase transition temperatures by controlling the thickness of each of the layers.[28] They also observed multiferroic properties above room temperature for those superlattices.

In the present study, I have grown epitaxial $LuFe_2O_4$ thin film on YSZ substrate by using a pulsed laser deposition (PLD) method. Moreover, I have found that the present thin film possesses self-assembled interface structure, as demonstrated by high-angle annular dark field scanning transmission electron microscopy (HAADF-STEM) and energy dispersive X-ray (EDX) spectrometry. Namely, there exists a region where Lu^{3+} ions are concentrated just on the surface of the substrate and very thin layers of $LuFe_2O_4$ lacking Fe-O layers, corresponding to the hexagonal $LuFeO_3$ (h-$LuFeO_3$) and $Lu_2Fe_3O_7$ compositions, are formed in this sequence on the Lu^{3+}-rich region. The $LuFe_2O_4$ thin film is epitaxially grown on the $Lu_2Fe_3O_7$–like layer. Such an interface structure might have influence on the magnetic properties of the present thin film, and indeed, leads to the exchange bias effect. On the other hand, the $LuFe_2O_4$ thin film itself exhibits spin glass transition as confirmed by my magnetization measurements such as dc magnetic field dependence of irreversible transition temperature and aging-memory effect. I have also examined electrical transport properties of the thin film. The mechanism of electronic

conduction changes at the 3D-CO as reported previously.

2.2 Sample fabrication

A PLD method was used for synthesis of $LuFe_2O_4$ thin film. A polycrystalline target of $LuFe_2O_4$ was prepared by using Lu_2O_3 (Nippon Yttrium Co., LTD., Japan, 99.9 %) and Fe_2O_3 (Kojundo Chemical Laboratory Co., Ltd., Japan, 99.99 %) as starting materials. A mixture of the materials with stoichiometric ratio was ground in an agate mortar. After pressing into a pellet, it was heated at 1200 ℃ for 24 h under an atmospheric condition that the molar ratio of CO/CO_2 was 1/2. X-ray diffraction (XRD) measurements with Cu $K\alpha$ radiation were conducted in order to confirm that the prepared target sample contained a single phase of $LuFe_2O_4$. The target material thus obtained was used for the deposition of thin films. The thin films were grown on (111) plane of 9.0 mol% YSZ substrates (SHINKOSHA, Co., Ltd., Japan). The YSZ substrates were first annealed at 1350℃ to obtain atomically smooth surface. The target material was irradiated with a pulsed KrF excimer laser operating at a power of 2.5 J/cm^2, a wavelength of 248 nm, and a repetition rate of 3 Hz. The substrate was set 3.5 cm apart from the target and kept at 850 ℃. The temperature was measured by an optical pyrometer. The deposition was performed under oxygen partial pressures of 2.00×10^{-5} to 2.00×10^{-3} Pa.

2.3 Characterization

XRD analysis with Cu $K\alpha$ radiation was carried out to examine the crystal structure of the thin films and the epitaxial relationship between the thin film and the substrate. I

utilized a four-circle Rigaku SmartLab diffractometer equipped with a Ge (220) $\times$ 2 monochromator on the incident side and an analyzer on the diffracted side. The composition and thickness of the thin films were estimated using Rutherford backscattering spectroscopy (RBS) with a 2.0 MeV He$^+$. Cross-sectional TEM specimens were prepared via a conventional method with focused ion beam (FIB). HAADF-STEM images were acquired on a 300 keV ThermoScientific Titan^3 60-300 with double corrector and EDX spectrometry was done with Super-X detector. Images were obtained with a detection angle of 82-200 mrad, a current value of 40 pA, and pixels of 512 $\times$ 512.

Magnetic properties were measured using a superconducting quantum interference device magnetometer (Quantum Design MPMS-SQUID). Magnetic field dependence of magnetization was explored at various temperatures from 100 to 300 K. A dc magnetic field up to 50 kOe was applied perpendicular to the film surface, i.e., parallel to the c-axis of LuFe$_2$O$_4$ in the hexagonal setting. Temperature dependence of field-cooled (FC) and zero field-cooled (ZFC) magnetization was examined under various dc magnetic fields of 1 to 10 kOe. Also, the measurement of aging-memory effect was performed in the ZFC procedure. For each of the measurements, the diamagnetic magnetizations of YSZ substrate were subtracted from those of the LuFe$_2$O$_4$ thin film deposited on the substrate. Electrical resistivity was measured as a function of temperatures in a range between 200 and 350 K by using physical property measurement system (Quantum Design PPMS). A patterned mask was set on the surface of the thin films, and Au was deposited by electron-beam-evaporation method. Thus, Au ohmic contact electrodes were fabricated and utilized for the electronic transport measurements.

2.4 Results and Discussion

2.4.1 Crystal structure.

The structural characterization has been carried on the resultant $LuFe_2O_4$ thin films to identify the crystalline phases formed and to examine the epitaxial relationship between the thin film and the substrate through the XRD technique. Figure 2.2 (a) depicts the θ-2θ scan of out-of-plane XRD for thin films grown on YSZ substrates at three different oxygen partial pressures. The thin film prepared under 2.00×10^{-4} Pa only exhibits highly c-axis oriented $LuFe_2O_4$ phase without other phases as far as the XRD patterns are concerned. One of the lattice constants, c, and the full-width at half maximum (FWHM) of (0003) diffraction peaks in rocking curve of $LuFe_2O_4$ were determined to be 25.1326 Å and 0.7216°, respectively. The value of FWHM is similar to those of $LuFe_2O_4$ thin films reported previously[25] and suggests that the present $LuFe_2O_4$ thin film has good crystalline quality. On the other hand, the thin film grown at 2.00×10^{-5} Pa contains impurity phases in addition to $LuFe_2O_4$ phase, and no $LuFe_2O_4$ phase was found in the thin film deposited under high oxygen partial pressure like 2.00×10^{-3} Pa. The results indicate that the growth of $LuFe_2O_4$ is very sensitive to the oxygen partial pressure and the structure seems to be easily decomposed to h-$LuFeO_3$ and Fe_3O_4 phases by reacting with oxygen. On the basis of the oxygen partial pressure dependence of crystalline phases formed, the thin film prepared at 2.00×10^{-4} Pa was used for subsequent measurements. In order to estimate the in-plane heteroepitaxial relationship between the $LuFe_2O_4$ thin film and the YSZ substrate, the reciprocal space mapping (RSM) was obtained around

the asymmetric reflections. The RSM around YSZ (331) reflection is displayed in Figure 2.2 (b), where q_x and q_z represent the in-plane and out-of-plane reciprocal vectors, respectively. The (1-10$\underline{22}$) and (1-10$\underline{19}$) Bragg peak positions of the LuFe$_2$O$_4$ film were recorded to calculate the in-plane lattice constants. As shown in Table 2.1, the in-plane lattice constants of LuFe$_2$O$_4$ thin film are similar to those of single-crystalline LuFe$_2$O$_4$, indicating that the lattice of LuFe$_2$O$_4$ thin film is not fixed by the substrate but relaxed to take lattice constants similar to those of the single-crystalline LuFe$_2$O$_4$. The epitaxial relationship between the thin film and the substrate is (0001) [1-100] LuFe$_2$O$_4$ // (111) [11-2] YSZ. Figure 2.2 (c) illustrates a possible growth mode for the LuFe$_2$O$_4$ thin film on the YSZ substrate with (111) orientation. Here, it should be noted that Figure 2.2 (c) only depicts the relation in lattice plane between the thin film and the substrate, because other phases or LuFe$_2$O$_4$ phase lacking Fe-O layers are formed as very thin layers at the interface, as described below. The surface morphology of LuFe$_2$O$_4$ thin film was examined by using atomic force microscopy (AFM). The roughness was evaluated to be about 2.5 nm as a standard deviation of height in an area of 3 μm × 3 μm (Figure 2.3). The growth mode of the present thin film is regarded as a typical 3D island growth and it is reasonable from a point of view of the rather large lattice mismatching between LuFe$_2$O$_4$ and YSZ.

The cation ratio and thickness of LuFe$_2$O$_4$ thin film deposited at 2.00 × 10^{-4} Pa were determined by using RBS technique. The analysis with the simulation program SIMNRA reveals that the film thickness is about 100 nm and the molar ratio of Fe to Lu is approximately 1.5 with a margin of error of about 10 %. This value of molar ratio is much

less than expected for stoichiometry of $LuFe_2O_4$. In other words, a large amount of iron was missing during the deposition process. This phenomenon is also confirmed by the HAADF-STEM image as mentioned below.

In order to elucidate the nanostructure of the thin film, HAADF-STEM and EDX measurements were performed. Figure 2.4 (a) shows HAADF-STEM image for the $LuFe_2O_4$/YSZ interface along [11-20] zone direction. Since the brightness scales approximately as the square of the atomic number Z in the HAADF images, only the lutetium ($Z = 71$) and iron ($Z = 26$) columns are visible. On the other hand, the oxygen ($Z = 8$) columns are indiscernible due to the small atomic number. In Figure 2.4 (a), the uppermost part clearly exhibits a sequence of iron bilayers separated by lutetium monolayers, which confirms that $LuFe_2O_4$ thin film is epitaxially grown with *c*-orientation. It is also found that there exists the brightest region at the surface of the YSZ substrate, indicating that Lu^{3+} ions are concentrated on very top of the substrate. Furthermore, a layer composed of iron monolayer and lutetium monolayer which are alternately stacked is formed just on the Lu^{3+}-rich region, and another layer comprising both iron monolayer and bilayer is found just below the $LuFe_2O_4$ thin film. The chemical compositions corresponding to these two-types of very thin layers might be $LuFeO_3$ and $Lu_2Fe_3O_7$, respectively. Figures 2.4 (b) and (c) illustrate the results of EDX analysis conducted for the region indicated by the yellow dashed rectangular in Figure 2.4 (a). The different colors in these figures represent the different elements. As presented in Figures 2.4 (b) and (c), numerous Lu^{3+} ions are present at the surface of the YSZ substrate, and the interface structure consisting of *h*-$LuFeO_3$-like (red rectangle area) and $Lu_2Fe_3O_7$-like

(blue rectangle area) phases is observed close to the Lu^{3+}-rich region. The h-$LuFeO_3$-like and $Lu_2Fe_3O_7$-like phases may be regarded as $LuFe_2O_4$ phase lacking Fe-O layers. In other words, the $LuFe_2O_4$ phase formed in the vicinity of interface possesses stacking faults typically observed for SiC and so forth.

On the basis of such an interface structure, it is speculated that iron is missing at the early stage of the deposition process presumably because of the volatilization of iron species due to the rather high substrate temperature and that iron-poor phases involving the Lu^{3+}-rich layer at the surface of the YSZ substrate are preferentially formed. After the formation of Lu^{3+}-rich layer, h-$LuFeO_3$-like phase, and $Lu_2Fe_3O_7$-like phase, for which the concentration of iron increases in this order, $LuFe_2O_4$ phase without stacking faults is eventually grown. This speculation is supported by the results of XRD measurements for the thin film samples prepared for different deposition durations, as shown in Figure 2.1 (b). In the XRD pattern of the sample obtained by the deposition for 30 min, diffraction lines assignable to h-$LuFeO_3$ and $Lu_2Fe_3O_7$ are evidently observed in addition to those of $LuFe_2O_4$, and the diffraction lines due to h-$LuFeO_3$ and $Lu_2Fe_3O_7$ disappear while those of $LuFe_2O_4$ grow in the XRD pattern for the 60 min deposition, suggesting that h-$LuFeO_3$-like and $Lu_2Fe_3O_7$-like phases are formed before the growth of $LuFe_2O_4$. The fact suggests that the Fe/Lu molar ratio grows larger as the thin film becomes thicker, although the RBS measurements were not carried out for thin film samples with different thicknesses.

The underlying mechanism of the above-mentioned stacking sequence at the interface is unclear at this moment, but taking account of the lattice mismatching of h-$LuFeO_3$/YSZ

system (~5.14 %) that is somewhat smaller than $LuFe_2O_4$/YSZ system (~5.34 %), the anomalous layered structure might act as a strain buffer layer. A similar phenomenon was reported by Cheng et al., who observed a self-assembled MnO double layer at the interface between $YMnO_3$ thin film and *c*-oriented sapphire substrate.[30] They concluded that the MnO double layer might act as a buffer layer to reduce the large mismatching between $YMnO_3$ and sapphire. In addition, considering the fairly high oxide ion conductivity of YSZ,[31-33] the oxygen partial pressure at the interface might be slightly higher than expected from the oxygen partial pressure initially set for the deposition of thin films, and hence, *h*-$LuFeO_3$ phase containing the higher valence states of iron (Fe^{3+}) might be easily formed. Furthermore, the Lu^{3+}-rich layer just on the surface of the YSZ substrate might be a buffer layer as well. Iida et al.[34] observed that amorphous layer was formed at the interface for *h*-$YbFeO_3$ thin film deposited on YSZ (111) substrate and they considered that the amorphous layer, which seems to be composed of a large amount of Y^{3+} ions, led to the relaxation of the lattice mismatch between the thin film and the substrate. This idea is applicable to the interface structure of the present thin film. However, more detailed measurements and analyses are necessary for complete understanding of the mechanism by which the Lu^{3+}-rich region and $LuFe_2O_4$ phase lacking Fe-O layers are formed at the interface.

A close look at Figure 2.4 (a) indicates that the Lu^{3+} ions in the *h*-$LuFeO_3$-like phase do not manifest any displacements. It seems that this observation is inconsistent with the fact that *h*-$LuFeO_3$ phase has a polar structure with the space group of *P*6$_3$*cm* at room temperature. However, the behaviour is explainable by referring to the fact observed for

YMnO$_3$ thin film, which has the same space group as h-RFeO$_3$, deposited on c-oriented

sapphire substrate.[35] The crystal structure of bulk YMnO$_3$ is assignable to $P6_3cm$, which

is polar due to the up-up-down arrangement of Y^{3+} ions, but such a shift of Y^{3+} ions is

suppressed when the YMnO$_3$ is a very thin film. A similar structural change is possible

for the present h-LuFeO$_3$-like phase and a shift of Lu^{3+} ions leading to a polar structure

is not realized as illustrated in Figure 2.4 (a).

2.4.2 Magnetic properties.

The coexistence of interface phases, h-LuFeO$_3$-like and Lu$_2$Fe$_3$O$_7$-like ones, with

LuFe$_2$O$_4$ thin film is expected to lead to modulated magnetic properties like those

observed for LuFe$_2$O$_4$/LuFeO$_3$ superlattice system.[28] Figure 2.5 shows the magnetic

properties of the present LuFe$_2$O$_4$ thin film on YSZ substrate. The measurements were

conducted by applying magnetic field perpendicular to the film surface because the easy

axis of magnetization is along the c-axis in the RFe$_2$O$_4$ systems. Figures 2.5 (a) and (b)

depict the magnetic field dependence of magnetization (M-H curve, where M is the

magnetization and H is the magnetic field) at various temperatures and the temperature

dependence of magnetization (M-T curve, where T is the temperature), respectively. The

insets in Figure 2.5 (a) indicate the magnified views of M-H curves at 300 K (upper panel)

and 100 K (lower panel). As seen in Figure 2.5 (a), the hysteresis loops were observed in

the M-H curves at all the temperatures of measurements. It is found that the magnetization

is not saturated even when a magnetic field as high as 50 kOe is applied. Such a

phenomenon was observed for other RFe$_2$O$_4$ compounds including thin films. For

example, thin film of $InFe_2O_4$ deposited on ZnO substrate does not manifest saturation of magnetization even at a high magnetic field like 50 kOe.[36] On the other hand, application of higher magnetic fields such as 70 kOe seems to lead to saturation magnetization, as demonstrated for $LuFe_2O_4$ thin films grown on SiC, $MgAl_2O_4$, and MgO substrates.[25] Such a hard magnetic moment was observed for single-crystalline YFe_2O_4 as well when the sample was cooled below 140 K in field-cooling process and the behaviour was interpreted by a model that the electron diffusion between Fe^{3+} and Fe^{2+} ions ceases at low temperatures and a distribution of iron ions with different valence states on the two antiferromagnetic sublattices is fixed.[37] Furthermore, it is curious that a clear hysteresis loop is observed even at 300 K, because the magnetic phase transition temperatures of $LuFe_2O_4$, $Lu_2Fe_3O_7$, and h-$LuFeO_3$ are lower than 300 K, as mentioned above. One possibility is that a 2D ordering[29] of magnetic moments restricted within the iron bilayers takes place in the $LuFe_2O_4$ phase and is reflected in the *M-H* curve. Another possibility is that the interface structure might lead to an increased magnetic phase transition temperature similarly to the $(LuFeO_3)_m/(LuFe_2O_4)_n$ superlattices.[28]

One of the striking features relevant to the above-mentioned interface structure is the presence of exchange bias (EB) effect as found in Figure 2.5 (a). The EB effect is caused by the competition between two different types of magnetic interactions at an interface between two different magnetically ordered phases such as antiferromagnetic (AFM) and ferromagnetic (FM) phases. In the present case, the EB effect is clearly observed at 100 K but is not seen above 200 K. Considering that the magnetic phase transition temperatures and magnetic structures of $LuFe_2O_4$, $Lu_2Fe_3O_7$, and h-$LuFeO_3$ were reported

to be 219 K (ferrimagnetism or antiferromagnetism),[28] 260-270 K (ferrimagnetism) ,[38] and 130 K (canted antiferromagnetism),[39-41] respectively, the EB effect might be induced by the canted magnetic moments in h-LuFeO$_3$-like phase at the interface between Lu$_2$Fe$_3$O$_7$-like and h-LuFeO$_3$-like layers. As a result, the shift of the M-H loop along the magnetic field axis can be distinguished at 100 K. A bias field (H_{EB}), which is defined as the absolute offset of the loop along the field axis, is about 730 Oe. This value signifies fairly large when compared with EB effect related to Fe$_3$O$_4$, a prototype of ferrimagnetic iron oxide, such as core/shell nanoparticles[42, 43] and thin film with heterostructure.[44, 45] However, the observed shift of M-H loop in the magnetically unsaturated state can be sometimes due to a minor hysteresis loop.[46, 47] In order to clarify the origin of the shift of hysteresis loop, firstly, the equal magnetizations values at the highest positive and negative fields are confirmed because a minor loop is asymmetrical and also expected to present significant vertical asymmetry.[48] In addition, I measured several consecutive hysteresis loops to elucidate the true EB effect in my system. This measurement is named as a training effect, which shows a gradual and monotonous degradation in the EB shift with the number of consecutive hysteresis loops (n) at a constant temperature and is the important characteristic of an EB system.[49-51] For the present thin film, the consecutive hysteresis loops were measured at 100 K after FC in 30 kOe. Figure 2.5 (b) displays the expansion of the low magnetic field region after FC process. In general, the shift of the consecutive hysteresis loops is pronounced at the left part of a loop, and on the other hand, the right part shows only slight shifts.[51] The inset of Figure 2.5 (b) also indicates the obvious magnetic training effect in my thin film. A considerable decrease in H_{EB}, about

43.3 %, can be seen between the first and the second loops and then slowly declines with increasing n. The relationship between H_{EB} and n can be expressed by using a simple power law, which can be valid only for $n > 1$,[52]

$$H_{EB}(n) - H_{EB,\infty} = \frac{k}{\sqrt{n}}$$

where k is a material dependent constant and $H_{EB}(n)$ and $H_{EB,\infty}$ are the magnitudes of the EB field for the nth cycle and in the limit of infinite loops, respectively. The resultant H_{EB} data clearly show that the experimental values are expressed well in terms of the power law, indicating that the EB field exists in the present $LuFe_2O_4$ thin film with interface structure.

Here, it should be noted that the training effect was observed in some alloys and oxides for which spin glass or cluster glass behaviour was found, such as $PdNCr_3$,[49] Si-substituted $Ni_{50}Mn_{36}Sn_{14}$[50] and $LiMn_2O_4$.[51] It was considered that magnetic phase boundary between glassy state and ferro-or antiferromagnetic phase was responsible for the EB effect in those compounds. The magnetic structure shown in the reports[49-51] is very similar to that of the present $LuFe_2O_4$ thin film itself. In other words, ferromagnetic and spin glass phases coexist in the $LuFe_2O_4$ thin film at low temperatures as suggested by the temperature dependence of magnetization illustrated in Figure 2.5 (c), and such a situation can create a magnetic phase boundary, which can be another possible origin to lead to the EB effect in addition to the interface between $Lu_2Fe_3O_7$-like and h-$LuFeO_3$-like phases mentioned above.

Meanwhile, I also explored the temperature dependence of magnetization at 50 to 300

K, as illustrated in Figure 2.5 (c). For the ZFC process, the sample was cooled down to 50 K without an external magnetic field, and for the FC measurement, an external magnetic field of 1 kOe was applied during the cooling-down process from 300 K. Although the FC and ZFC curves coincide with each other at higher temperatures, the bifurcation into two curves occurs below a certain temperature. Here, I define this temperature as an irreversible transition temperature (T_{irr}). A sudden ascent of magnetization around 250 K as the temperature is decreased is ascribable to 3D magnetic long-range ordering. In other words, the magnetic phase transition occurs from paramagnetic to ferrimagnetic states. The Néel temperature, T_N, evaluated by the first-order temperature derivative of magnetization (dM/dT) as shown in the inset of Figure 2.5 (b) is about 236 K. This value is somewhat higher than the reported T_N, about 219 K for the $LuFe_2O_4$ thin film,[28] although the values of T_N reported for $LuFe_2O_4$ thin films are slightly diverse depending on the kinds of substrates and the definition of T_N. The increased magnetic transition temperature may be related to the $Lu_2Fe_3O_7$-like phase.[36, 53]

The ZFC curve shown in Figure 2.5 (c) has a maximum at about 220 K. This fact as well as the behavior that the FC and ZFC curves diverge from each other at T_{irr} suggests that the present thin film undergoes the spin glass or cluster glass transition. To clarify the magnetic phase of the present thin film at low temperatures, the measurements of FC and ZFC magnetizations were carried out under various dc magnetic fields of 1, 3, 5, 7, and 10 kOe. Figure 2.6 (a) shows the results obtained for 1, 3, and 7 kOe. It is found that T_{irr} monotonically decreases with increasing the applied dc magnetic field. This

phenomenon, which is the characteristic of *M-T* curves observed for spin glasses or cluster glasses, implies that the frozen state of magnetic moments arising from the magnetic frustration is suppressed by the strong magnetic fields.[54] As indicated in Figure 2.6 (b), the magnetic field dependence of T_{irr} follows the de Almeida-Thouless (AT) line expressed by the following relation:

$$H(T_{irr})/ \Delta J \propto (1 - T_{irr}/T_F)^{3/2},$$

where ΔJ is the distribution width of the exchange interaction and T_F is the spin freezing temperature.[55] Though the ac susceptibility measurements at varied frequencies would be generally an important indicator to reveal the glassy behavior, an attempt to obtain ac susceptibilities for the present $LuFe_2O_4$ thin film resulted in failure because the ac magnetic signals were too weak to distinguish from the noise of dc mode in SQUID.[56] Nevertheless, the fact that the magnetic field dependence of T_{irr} is interpreted well in terms of the AT-line verifies that the present thin film undergoes spin glass transition. According to the previous reports on $LuFe_2O_4$ bulk samples, the oxygen nonstoichiometry is an important factor for the occurrence of spin glass or cluster glass transition induced by the randomly distributed Fe^{3+} and Fe^{2+} ions with antiferromagnetic interactions.[15-17] It is thought that the present $LuFe_2O_4$ thin film also has an imbalance in the numbers of Fe^{2+} and Fe^{3+} ions due to the oxygen nonstoichiometry.

I have studied the aging effect for the present $LuFe_2O_4$ thin film to confirm that the magnetic phase of the thin film is spin glass or cluster glass at low temperatures. The temperature dependence of dc magnetic susceptibility ($\chi(T)$) was examined by using a

protocol proposed by Mathieu et al.[57] This protocol includes the procedure that $\chi(T)$ is measured on heating after ZFC with an intermittent stop at a temperature below the magnetic transition temperature. In my case, the thin film was first cooled from 250 K that is above $T_N = 236$ K to a stopping temperature of $T_S = 180$ K, which is lower than the temperature of maximum ZFC magnetization, at a rate of 2 K/min, and was kept at T_S for 6 h. After a stop for 6 h, the thin film was cooled to 150 K at a rate of 2 K/min. As a reference, $\chi_{ref}(T)$ was determined by measuring the temperature dependence of ZFC susceptibility without any intermittent stops. The obtained result is shown in Figure 2.7. It is found that $\chi(T)$ is somewhat smaller than $\chi_{ref}(T)$ in a temperature range close to T_s. At temperatures far from T_S, the $\chi(T)$ and $\chi_{ref}(T)$ curves merge with each other. The difference between $\chi(T)$ and $\chi_{ref}(T)$ as a function of temperature is presented in the upperpart of Figure 2.7. The aging effect is detected as a dip at around T_S. The occurrence of the dip, called a memory effect, indicates that the spin configurations acquired at T_S after aging are preserved even after cooling and subsequently heating. Because the spin configuration at a particular temperature (T) is completely different from other spin configurations at $T+\Delta T$ with sufficiently large ΔT, the aging at T does not affect the spin structure at $T+\Delta T$. This effect usually occurs in spin glasses and strongly interacting magnetic nanoparticles systems or cluster glasses. Hence, the observation of the aging-memory effect as well as the above-mentioned phenomenon that the relationship between T_{irr} and H follows the AT-line is an indication of spin glass or cluster glass transition.

2.4.3 Electrical properties.

There exist a few reports on electrical conduction of $LuFe_2O_4$ thin film. Rai et al.[24] measured the electrical resistivity of $LuFe_2O_4$ thin film deposited on (0001) sapphire substrate at various temperatures between 78 and 400 K. They observed a change in slope at Néel temperature, i.e., 235 K and a fluctuation of resistivity at about 350 K in the relation between the inverse of temperature and the logarithmic resistivity. They considered that the temperature at which the fluctuation of resistivity occurred was the temperature of 3D-CO transition in $LuFe_2O_4$. Fujiwara et al.[26] fabricated $LuFe_2O_4$ thin film on (111) YSZ substrate and examined its temperature dependence of resistivity. According to their report, the slope of the logarithmic resistivity-inverse of temperature relation changes around 310 K, which is close to the temperature of 3D-CO transition. The activation energies above and below the temperature of 3D-CO transition they calculated by assuming the Arrhenius-type mechanism are 0.23 and 0.28 eV, respectively. They also found that the current density drastically increased as the electrical field exceeded a certain threshold and attributed this phenomenon to the phase transition between charge ordered and disordered states induced by the electric field.

Figure 2.8 shows the temperature dependence of electrical resistivity for the present $LuFe_2O_4$ thin film measured by flowing the dc current in the film surface, i.e. in the *ab*-plane. The observed result, therefore, manifests the intrinsic electrical properties of $LuFe_2O_4$ phase, which are not affected by the interface structure. The resistivity increases with decreasing temperature, indicating that the $LuFe_2O_4$ thin film is an insulator or a semiconductor. Also, a change in slope is observed at about 310 K, which is close to 320

61

K known as the temperature of 3D-CO transition in bulk $LuFe_2O_4$.[21, 22] The behavior is very similar to that reported by Fujiwara et al.[26] The resistivity above 310 K is well fitted with Arrhenius law and the estimated activation energy is 0.23 eV. This value is similar to the activation energy for the temperature dependence of electrical resistivity in the direction perpendicular to the c-axis of the single crystalline $LuFe_2O_4$,[11] and just the same as the value reported by Fujiwara et al.[26] In contrast, below 310 K, the resistivity is best fitted to the 3D Mott-variable range hopping (VRH) scheme, i.e., $\rho \propto \exp[(T_0/T)^{1/4}]$, where ρ is the resistivity and T_0 is the characteristic temperature,[58] as illustrated in Figure 2.8 (b). This fact indicates that the electron hopping occurs between Fe^{2+} and Fe^{3+} ions below the 3D-CO temperature. The inset in Figure 2.8 (b) presents an attempt to fit the experimental data with the thermal activation (TA) scheme, i.e., $\ln(\rho) \propto T^{-1}$, suggesting the nearest-neighbor-hopping (NNH) process cannot support the electronic transport behavior in the 3D-CO state.

2.5 Conclusion

In summary, I have prepared $LuFe_2O_4$ thin film on (111)-oriented YSZ substrate with unique interface structure by using a pulsed laser deposition method. The out-of-plane X-ray diffraction and reciprocal space mapping indicate that the thin film is grown along the c-axis with the epitaxial relationship of (0001)[1-100]$LuFe_2O_4$//(111)[11-2]YSZ. Very thin layers of h-$LuFeO_3$-like and $Lu_2Fe_3O_7$-like phases or $LuFe_2O_4$ phase lacking Fe-O layers are formed at the interface between the $LuFe_2O_4$ thin film and the YSZ substrate. Considering the smaller

lattice mismatching of h-LuFeO$_3$/YSZ interface when compared with the LuFe$_2$O$_4$/YSZ interface, the very thin layers are considered to be buffer layers. Because of such an interface structure composed of different types of magnetic oxides, large exchange bias effect was observed at 100 K. The LuFe$_2$O$_4$ thin film itself undergoes ferrimagnetic phase transition around 236 K and spin glass or cluster glass transition at 220 K. The spin glass or cluster glass phase was ascertained by the dc magnetic field dependence of irreversible transition temperature as well as the aging-memory effect. For the electrical resistivity, Arrhenius-type and Mott-VRH schemes are observed at temperatures above and below the 3D-CO temperature, respectively.

References in chapter 2

1. N. A. Spaldin, M. Fiebig, *Science.* 2005, *309*(5733), 391-392.

2. W. Eerenstein, N. Mathur, J. F. Scott, *Nature.* 2006, *442*(7104), 759.

3. N. Kimizuka, A. Takenaka, Y. Sasada, T. Katsura, *Solid State Commun.* 1974, *15*(8), 1321-1323.

4. M. Isobe, N. Kimizuka, J. Iida, S. Takekawa, *Acta Cryst.* 1990, *46*(10), 1917-1918.

5. T. Mueller, J. de Groot, J. Strempfer, M. Angst, *J. Cryst. Growth.* 2015, *428*, 40-45.

6. N. Ikeda, H. Ohsumi, K. Ohwada, K. Ishii, T. Inami, K. Kakurai, Y. Murakami, K. Yoshii, S. Mori, Y. Horibe, *Nature.* 2005, *436*(7054), 1136.

7. M. Subramanian, T. He, J. Chen, N. S. Rogado, T. G. Calvarese, A. W. Sleight, *Adv. Mater.* 2006, *18*(13), 1737-1739.

8. Y. Zhang, H. Yang, C. Ma, H. Tian, J. Li, *Phys. Rev. Lett.* 2007, *98*(24), 247602.

9. H. Xiang, M. Whangbo, *Phys. Rev. Lett.* 2007, *98*(24), 246403.

10. A. Nagano, M. Naka, J. Nasu, S. Ishihara, *Phys. Rev. Lett.* 2007, *99*(21), 217202.

11. S. Lafuerza, J. García, G. Subías, J. Blasco, K. Conder, E. Pomjakushina, *Phys. Rev. B.* 2013, *88*(8), 085130.

12. Y. Yamada, S. Nohdo, N. Ikeda, *J. Phys. Soc. Jpn.* 1997, *66*(12), 3733-3736.

13. Y. Yamada, K. Kitsuda, S. Nohdo, N. Ikeda, *Phys. Rev. B.* 2000, *62*(18), 12167.

14. A. D. Christianson, M. D. Lumsden, M. Angst, Z. Yamani, W. Tian, R. Jin, E. A. Payzant, S. E. Nagler, B. C. Sales, D. Mandrus, *Phys. Rev. Lett.* 2008, *100*(10), 107601.

15. M. Phan, N. Frey, H. Srikanth, M. Angst, B. C. Sales, D. Mandrus, *J. Appl. Phys.* 2009, *105*(7), 07E308.

16. F. Wang, J. Kim, Y. Kim, G. Gu, *Phys. Rev. B.* 2009, *80*(2), 024419.

17. M. Phan, N. Frey, M. Angst, J. De Groot, B. C. Sales, D. Mandrus, H. Srikanth, *Solid State Commun.* 2010, *150*(7-8), 341-345.

18. P. Ren, Z. Yang, W. Zhu, C. Huan, L. Wang, *J. Appl. Phys.* 2011, *109*(7), 074109.

19. D. Niermann, F. Waschkowski, J. de Groot, M. Angst, J. Hemberger, *Phys. Rev. Lett.* 2012, *109*(1), 016405.

20. A. Ruff, S. Krohns, F. Schrettle, V. Tsurkan, P. Lunkenheimer, A. Loidl, *Eur. Phys. J. B.* 2012, *85*(8), 290.

21. C. Li, X. Zhang, Z. Cheng, Y. Sun, *Appl. Phys. Lett.* 2008, *93*(15), 152103.

22. S. Cao, J. Li, H. Tian, Y. Qin, L. Zeng, H. Yang, J. Li, *Appl. Phys. Lett.* 2011, *98*(10), 102102.

23. J. Liu, Y. Wang, J. Dai, *Thin Solid Films.* 2010, *518*(23), 6909-6914.

24. R. Rai, A. Delmont, A. Sprow, B. Cai, M. Nakarmi, *Appl. Phys. Lett.* 2012, *100*(21), 212904.

25. C. M. Brooks, R. Misra, J. A. Mundy, L. A. Zhang, B. S. Holinsworth, K. R. O'Neal, T. Heeg, W. Zander, J. Schubert, J. L. Musfeldt, *Appl. Phys. Lett.* 2012, *101*(13), 132907.

26. K. Fujiwara, T. Hori, H. Tanaka, *J. Phys. D: Appl. Phys.* 2013, *46*(15), 155108.

27. R. Kashimoto, T. Yoshimura, A. Ashida, N. Fujimura, *Thin Solid Films.* 2016, *614*, 44-46.

28. J. A. Mundy, C. M. Brooks, M. E. Holtz, J. A. Moyer, H. Das, A. F. Rébola, J. T. Heron, J. D. Clarkson, S. M. Disseler, Z. Liu, *Nature.* 2016, *537*(7621), 523.

29. J. Y. Park, J. H. Park, Y. K. Jeong, H. M. Jang, *Appl. Phys. Lett.* 2007, *91*(15), 152903.

30. S. Cheng, C. Xu, S. Deng, M. Han, S. Bao, J. Ma, C. Nan, W. Duan, L. Bellaiche, Y. Zhu, *Sci. Adv.* 2018, *4*(5), 1-6.

31. T. J. Pennycook, M. J. Beck, K. Varga, M. Varela, S. J. Pennycook, S. T. Pantelides, *Phys. Rev. Lett.* 2010, *104*(11), 115901.

32. A. Kushima, B. Yildiz, *J. Mater. Chem.* 2010, *20*(23), 4809-4819.

33. G. Dezanneau, J. Hermet, B. Dupé, *Int. J. Hydrogen Energy.* 2012, *37*(9), 8081-8086.

34. H. Iida, T. Koizumi, Y. Uesu, K. Kohn, N. Ikeda, S. Mori, R. Haumont, P.-E. Janolin, J.-M. Kiat, M. Fukunaga, Y. Noda, *J. Phys. Soc. Jpn.* 2012, *81*(2), 024719.

35. S. Cheng, M. Li, S. Deng, S. Bao, P. Tang, W. Duan, J. Ma, C. Nan, J. Zhu, *Adv. Funct. Mater*. 2016, *26*, 3589–3598.

36. M. Seki, T. Konya, K. Inaba, H. Tabata, *Appl. Phys. Express* 2010, *3*, 105801.

37. T. Sugihara, K. Siratori, I. Shindo, T. Katsura, *J. Phys. Soc. Jpn*. 1978, *45*(4), 1191-1198.

38. K. Yoshii, N. Ikeda, R. Fukuyama, T. Nagata, T. Kambe, Y. Yoneda, T. Fukuda, S. Mori, *Solid State Commun.* 2013, *173*, 34-37.

39. Y. K. Jeong, J. Lee, S. Ahn, H. M. Jang, *Chem. Mater.* 2012, *24*(13), 2426-2428.

40. J. A. Moyer, R. Misra, J. A. Mundy, C. M. Brooks, J. T. Heron, D. A. Muller, D. G. Schlom, P. Schiffer, *APL Materials.* 2014, *2*(1), 012106.

42. P. Suresh, K. V. Laxmi, A. Bera, S. Yusuf, B. L. Chittari, J. Jung, P. A. Kumar, *Phys. Rev. B.* 2018, *97*(18), 184419.

43. X. Sun, N. Frey Huls, A. Sigdel, S. Sun, *Nano Lett.* 2011, *12*(1), 246-251.

44. Y. Ijiri, J. Borchers, R. Erwin, S. Lee, P. Van der Zaag, R. Wolf, *Phys. Rev. Lett.* 1998,

80(3), 608.

45. D. Zheng, M. Sun, D. Li, P. Li, C. Jin, H. Bai, *EPL (Europhysics Letters).* 2015*, 110*(2), 27005.

46. T. Qu, Y. Zhao, P. Yu, H. Zhao, S. Zhang, L. Yang, *Appl. Phys. Lett.* 2012*, 100*(24), 242410.

47. J. Geshev, *J. Appl. Phys.* 2009, *105*, 066108.

48. J. Geshev, *J. Magn. Magn. Mater.* 2008, *320*, 600-602.

49. B. M. Wang, Y. Liu, P. Ren, B. Xia, K. B. Ruan, J. B. Yi, J. Ding, X. G. Li and L. Wang, *Phys. Rev. Lett.* 2011, *106*, 077203.

50. S. Lin, D. F. Shao, J. C. Lin, L. Zu, X. C. Kan, B. S. Wang, Y. N. Huang, W. H. Song, W. J. Lu, P. Tong and Y. P. Sun, *J. Mater. Chem. C.* 2015, *3*, 5683.

51. G. R. Raji, B. Uthaman, R. K. Rajan, M. P. Sharannia, S. Thomas, K. G. Suresh and M. R. Varma, *RSC Adv.* 2016, *6*, 32037.

52. X. K. Zhang, J. J. Yuan, Y. M. Xie, Y. Yu, F. G. Kuang, H. J. Yu, X. R. Zhu and H. Shen, *Phys. Rev. B.* 2018, *97*, 104405.

53. D. Paccard, C. Schlenker, O. Massenet, R. Montmory and A. Yelon, *Phys. Status Solidi.* 1966, *16*, 301.

54. J. Iida, M. Tanaka, S. Funahashi, *J. Magn. Magn. Mater.* 1992*, 104*, 827-828.

55. B. Cui, C. Song, G. Wang, H. Mao, F. Zeng, F. Pan, *Sci. Rep.* 2013*, 3*, 2542.

56. K. Binder, A. P. Young, *Rev. Mod. Phys.* 1986*, 58*(4), 801.

57. B. Pang, L. Zhang, Y. Chen, J. Zhou, S. Yao, S. Zhang, Y. Chen, *ACS Appl. Mater. Interfaces.* 2017*, 9*(3), 3201-3207.

58. R. Mathieu, P. Jönsson, D. Nam, P. Nordblad, *Phys. Rev. B.* 2001*, 63*(9), 092401.

59. N. F. Mott, E. A. Davis, *Electronic processes in non-crystalline materials*, Oxford University press 2012.

Table 2.1 Lattice constants and cell volume evaluated from the Reciprocal space mapping

(RSM) data for $LuFe_2O_4$ thin film and its bulk single-crystalline counterpart.
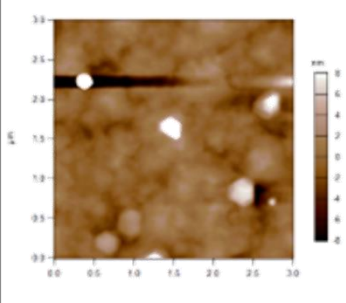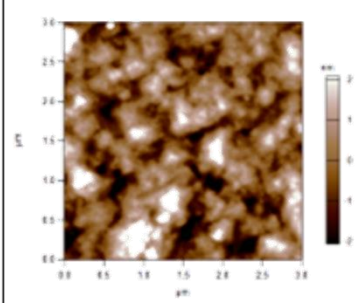
	Bulk	Film	A film / a bulk Ratio
a, b $(Å)$	3.4433	3.4459	1.0007
c $(Å)$	25.242	25.1326	0.9957
V $(Å^3)$	259.1816	258.4481	1.0029
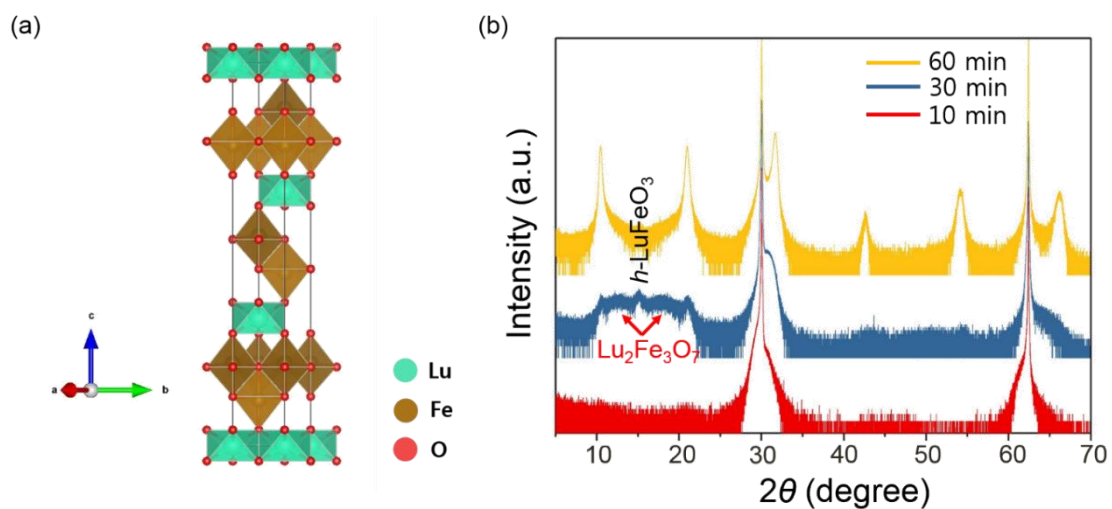
Figure 2.1. (a) Schematic illustration of crystal structure for $LuFe_2O_4$ viewed as a hexagonal system. (b) θ-2θ out-of-plane XRD patterns for the $LuFe_2O_4$ thin films grown under diverse duration times. The diffraction lines ascribable to h-$LuFeO_3$ and $Lu_2Fe_3O_7$ phases are observed after 30 min deposition. All the diffraction lines observed for the specimen after 60 min deposition are assigned to $LuFe_2O_4$ phase.
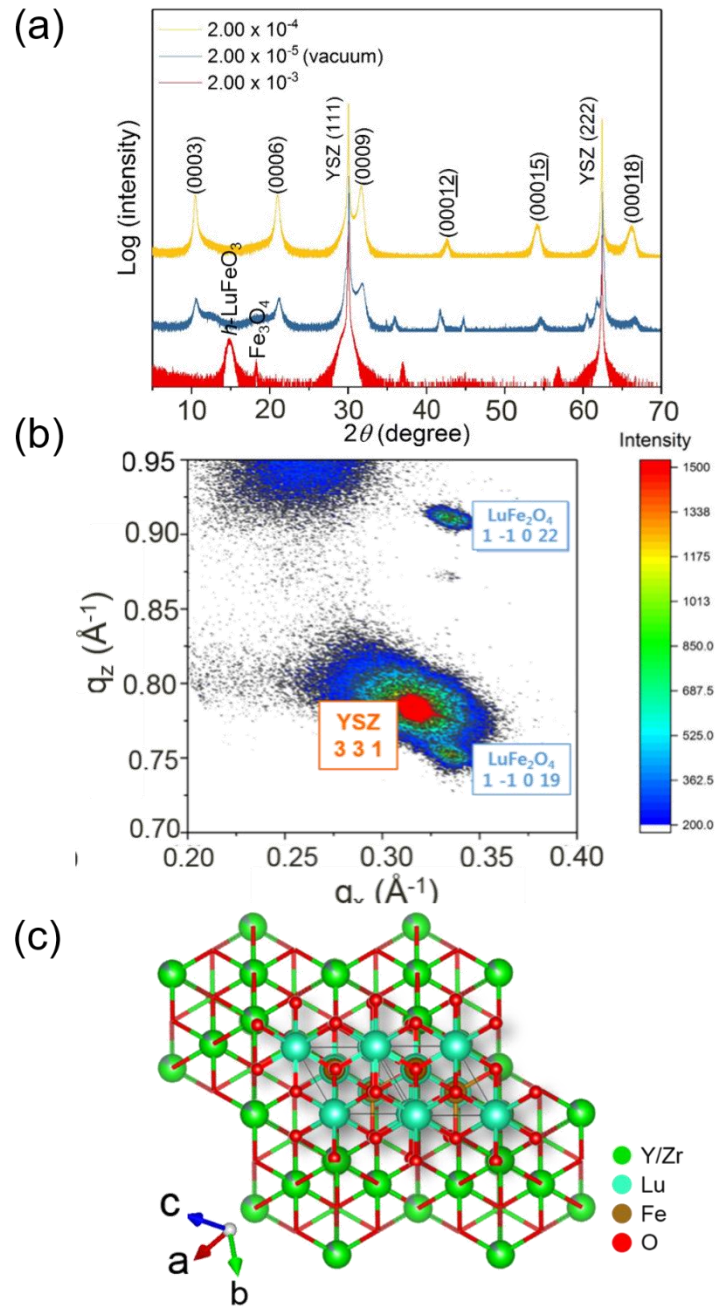
Figure 2.2. (a) θ-2θ out-of-plane XRD patterns for the thin films deposited on the (111)-oriented YSZ substrates under various oxygen partial pressures. (b) RSM around (331) diffraction peak of YSZ substrate and for (1-10$\underline{19}$) and (1-10$\underline{22}$) diffraction peaks of LuFe$_2$O$_4$ thin film. (c) Possible growth mode for the LuFe$_2$O$_4$ thin film / YSZ substrate system, for which the orientation relationship is LuFe$_2$O$_4$ [0001] // YSZ [111].

Root Mean Square (RSM, nm)	3.912	1.036
Region (μm × μm)	3 × 3	

**Figure 2.3.** AFM images of LuFe$_2$O$_4$ thin film.
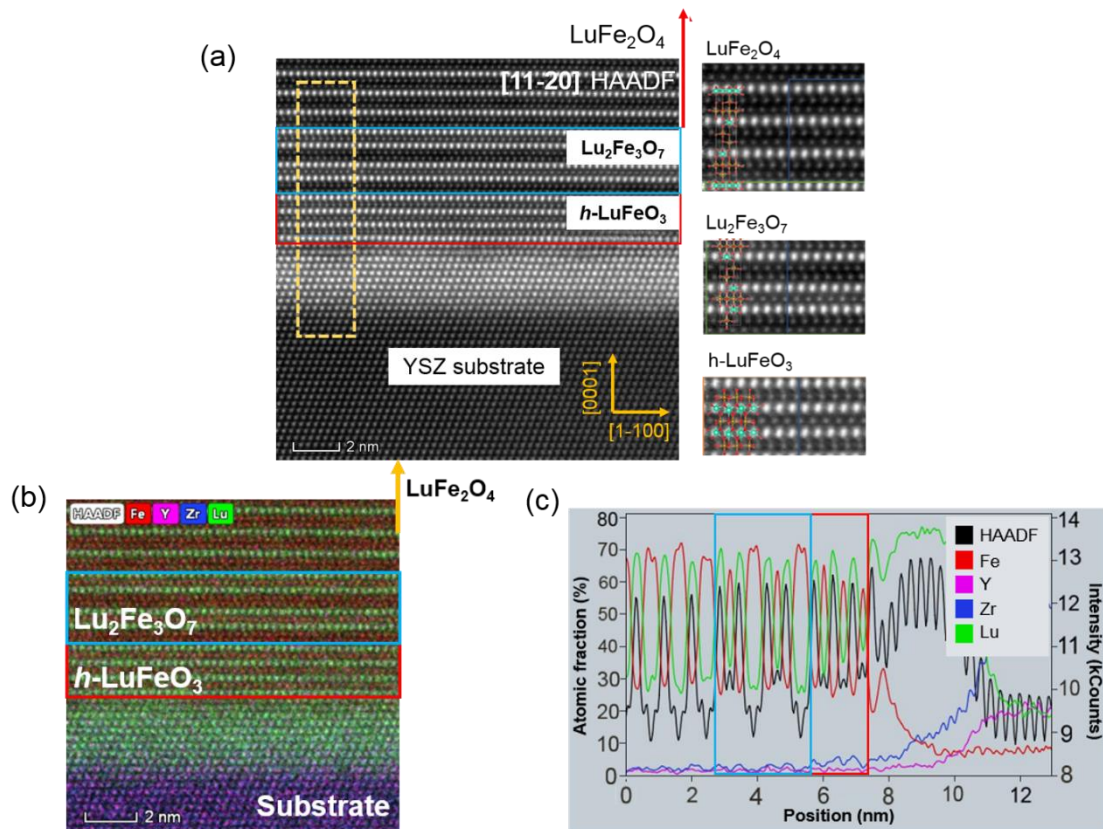
Figure 2.4. (a) HAADF-STEM image of the $LuFe_2O_4$ thin film grown on the YSZ substrate. $LuFe_2O_4$ phases lacking Fe-O layers, corresponding to h-$LuFeO_3$ and $Lu_2Fe_3O_7$ compositions, as well as $LuFe_2O_4$ phase without such a stacking fault are observed, as illustrate on the right side. (b) STEM-EDX image, which indicates that a large number of Lu^{3+} ions are present on the surface of the YSZ substrate as well as the self-assembled interface phases. (c) The corresponding integrated intensity profile across the interface from the YSZ substrate (the rightmost side) to the $LuFe_2O_4$ thin film (the leftmost side).
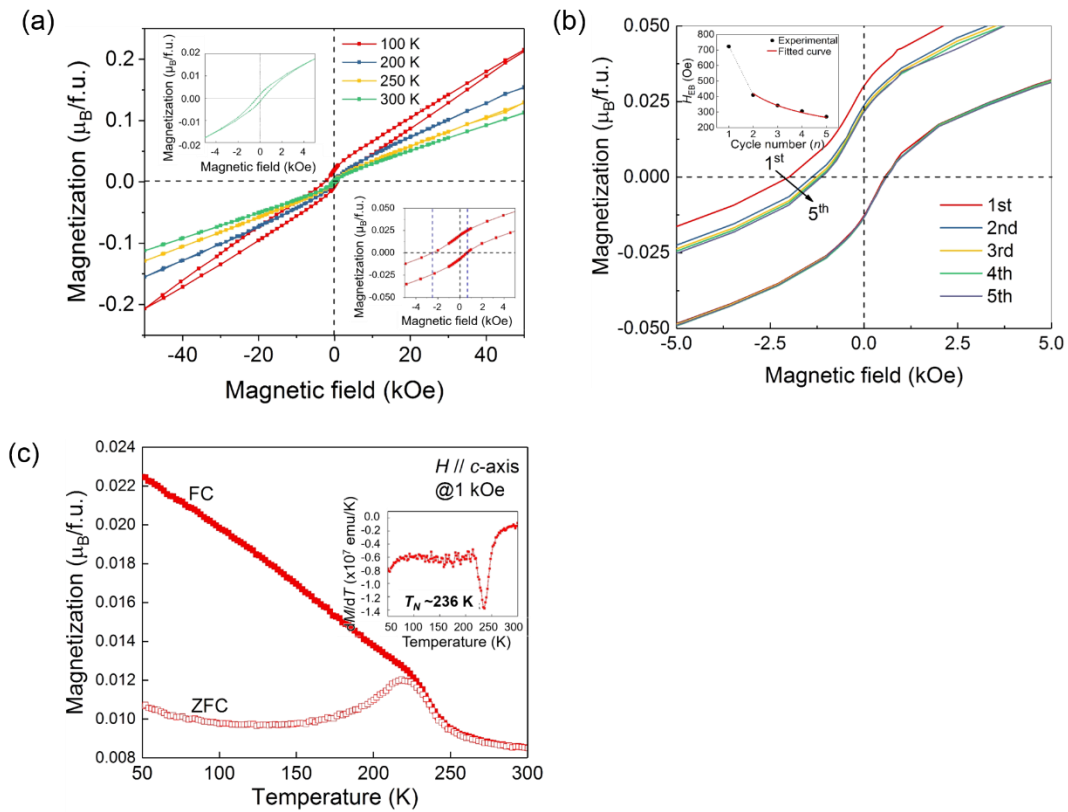
Figure 2.5. Magnetic properties of the LuFe$_2$O$_4$ thin film. (a) *M-H* curves measure at various temperatures of 100, 200, 250, and 300 K. The inset at left upper side illustrates an enlarged *M-H* curve at 300 K. The bottom right inset indicates a shift of hysteresis loop observed at 100 K under ZFC process. (b) The enlarged view of the central region of the consecutive hysteresis loops after cooling in a field of 30 kOe with increasing field cycles (*n*), indicating that training effect of exchange bias occurs at 100 K. The inset depicts the dependence of H_{EB} on the cycle number (*n*). The solid black circles represent the experimental data and the solid red lien shows the fitting of the power law to the observed values. (c) Temperature dependence of ZFC and FC magnetizations measured at 1 kOe of dc magnetic field. The inset depicts the first-order temperature derivative of magnetization, from which the Néel temperature is estimated to be 236 K.
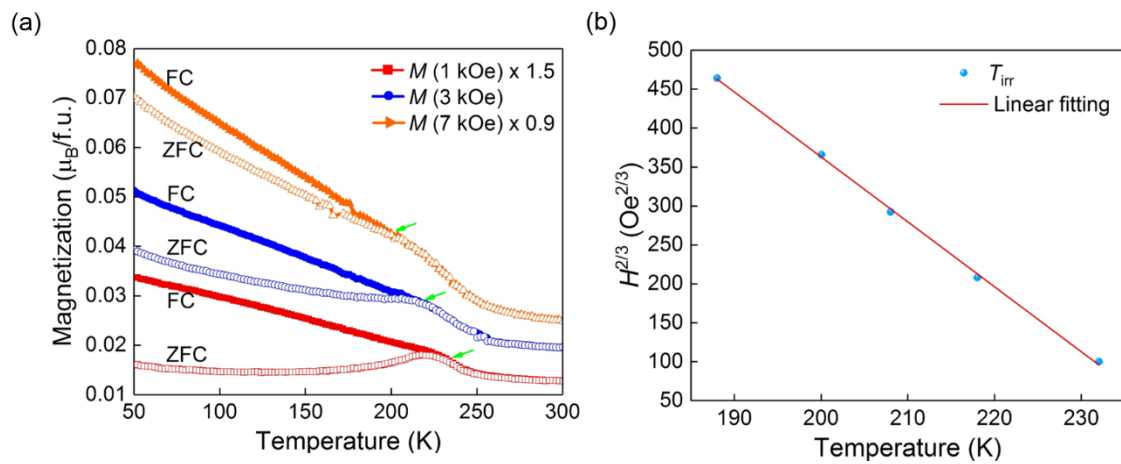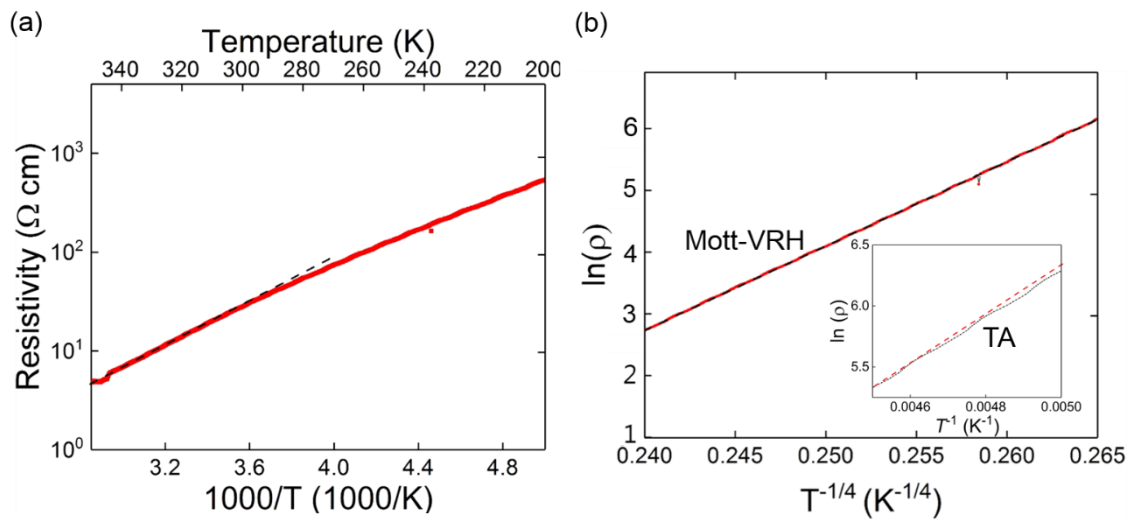
Figure 2.6. (a) Temperature dependence of ZFC and FC magnetizations measured at various dc magnetic fields (H = 1, 3, and 7 kOe). Curves symbolized by solid and open figures denote FC and ZFC magnetizations as a function of temperature, respectively. The arrows represent T_{irr}. (b) The relations between T_{irr} and $H^{2/3}$. The experimental data can be analysed well in terms of the de Almeida-Thouless (AT) line. The experimental errors, which are the standard deviations of T_{irr}, lie in a range between 0.25 and 0.3 K.
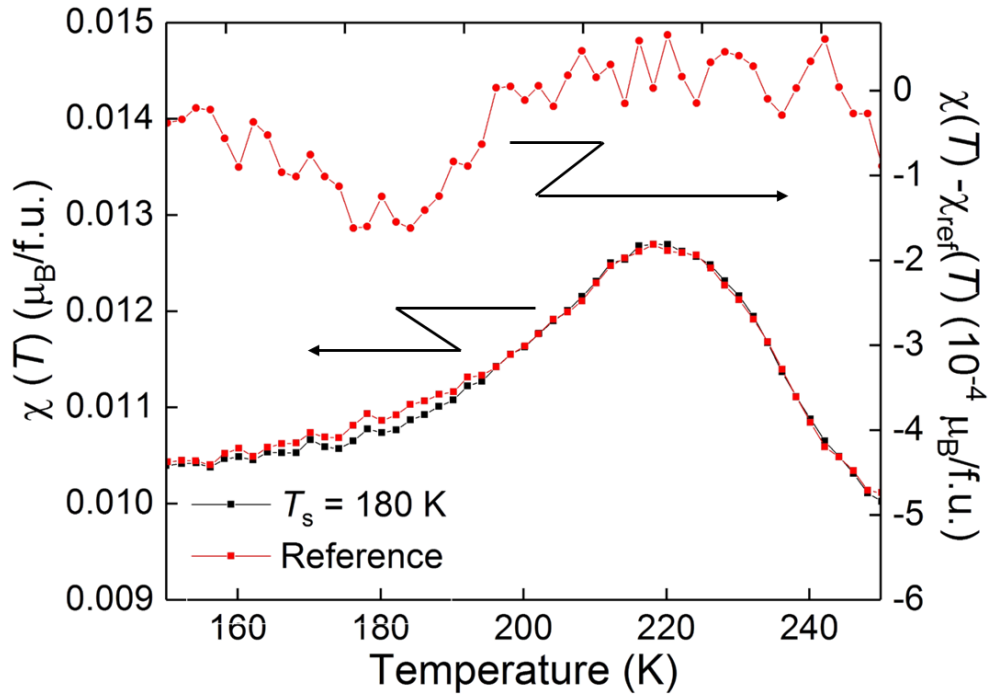
Figure 2.7. Temperature dependence of dc magnetic susceptibility measured on heating after zero-field-cooling with and without an intermittent stop, i.e., aging at $T_S = 180$ K. The difference between $\chi(T)$ and $\chi_{\mathrm{ref}}(T)$ is presented in the upperpart of the figure. Here, $\chi(T)$ and $\chi_{\mathrm{ref}}(T)$ are temperature-dependent susceptibilities with and without the aging, respectively.

Figure 2.8. (a) Temperature dependence of electrical resistivity measured at low dc current. The dashed line was fitted to the data at higher temperatures, indicating a change in slope at about 310 K. (b) Logarithm of resistivity versus $T^{-1/4}$ plot, corresponding to the 3D Mott-variable range hopping (VRH) scheme. The inset shows the logarithm of resistivity versus T^{-1} plots, corresponding to the thermal activation (TA) scheme.

Chapter 3: Magnetic properties of epitaxial TmFe₂O₄ thin film with anomalous interface structure

3.1 Introduction

A coupling among spin, charge and orbital degree of freedom in transition metal oxides brings about intriguing physical phenomena such as multiferroicity, where two or more ferroic order parameters govern the physical properties in a single phase.[1–3] In particular, materials with both long-range magnetic ordering and ferroelectricity have been extensively studied owing to their unique properties caused by the interaction between magnetic and dielectric orderings. These materials are expected to be promising candidates for spin-transistors and next-generation memory devices, for which it is possible to control magnetism (dielectricity) by electric (magnetic) fields.[3] However, single-phase multiferroics are not so many because the electronic configurations of cations responsible for the magnetism and displacive-type ferroelectricity, respectively, are not coincident with each other, and in addition, many of the multiferroics reported thus far usually show magnetic and dielectric phase transitions at low temperatures.[4–7] Consequently, much attention has been focused on ferroelectricity originating from unconventional mechanisms like complex lattice distortion and charge or spin ordering.[2]

$R\mathrm{Fe_2O_4}$ (R = Sc, Y, In, and Dy to Lu) is a family of multiferroic materials where ferroelectricity is thought to be driven by the charge ordering owing to an equal number of $\mathrm{Fe^{2+}}$ and $\mathrm{Fe^{3+}}$ ions, coupled with the spin degree of freedom.[8,9] Supposing that the structure of $R\mathrm{Fe_2O_4}$ is regarded as a hexagonal lattice,[10] it is composed of [FeO₅] bilayers

separated by [RO_6] monolayers along the c-axis, with each cation located in a triangular lattice as shown in Figure 3.1 (a). In other words, both charge and spin arrangements of iron ions are geometrically frustrated, rendering the rather complicated ground states of charge and spin structures. The spins of iron ions are described by the Ising model because the Fe^{2+} and Fe^{3+} in the high spin states exhibit strong anisotropy along the c-axis.[11] Among the $R\mathrm{Fe_2O_4}$ compounds, $\mathrm{LuFe_2O_4}$ has been most extensively studied; a large number of papers have been published concerning it structure, dielectricity, electrical conductivity, and magnetism.[9,12–15] Single-crystalline and polycrystalline $\mathrm{LuFe_2O_4}$ bulk materials were reported to undergo magnetic transitions at Néel temperature of about 220-240 K.[16–20] In addition, $\mathrm{LuFe_2O_4}$ is known to show complicated magnetic properties such as spin or cluster glass transition,[16–19] magnetostructural transition at T_{LT} ~170 K,[16] and a competition between ferri- and antiferromagnetic (AFM) states,[20] presumably because of the frustrated spins in the triangular lattice and the oxygen off-stoichiometry. Thus, the magnetic structure and properties of the $R\mathrm{Fe_2O_4}$ compounds involving $\mathrm{LuFe_2O_4}$ are rather intricate, many aspects of which remain to be understood.

Thin films as well as bulk forms of $R\mathrm{Fe_2O_4}$ are of importance from a point of view of both fundamental and applications. As for the thin films, electronic structures at interfaces often lead to unusual physical properties. For instance, superconductivity emerges at the interface between $\mathrm{SrTiO_3}$ and $\mathrm{LaAlO_3}$ thin films although both of these oxides are insulators.[21] Another example is the confinement of two-dimensional electron gas in Nb-doped $\mathrm{SrTiO_3}$ quantum well formed in between $\mathrm{SrTiO_3}$ layers, which results in very large thermoelectric Seebeck coefficient.[22] For the $R\mathrm{Fe_2O_4}$-related compounds, unique

magnetic properties were found in artificial superlattices composed of $LuFe_2O_4$ and hexagonal $LuFeO_3$, which had never been observed in bulk RFe_2O_4 compounds.[23] It was revealed that $(LuFeO_3)_m/(LuFe_2O_4)_n$ superlattices exhibited multiferroic properties above room temperature. In addition, there are some reports on synthesis, structural analysis, and measurements of physical properties for $LuFe_2O_4$,[24–27] $YbFe_2O_4$,[28–30] and $InFe_2O_4$[31] thin films. However, to my best of knowledge, there exist few reports focusing on the details of interface structure and properties of RFe_2O_4 thin films.

In this study, I report the synthesis of $TmFe_2O_4$ thin film epitaxially grown on an yttria-stabilized zirconia (YSZ) substrate by using a pulsed laser deposition (PLD) technique. The epitaxial relationship is established by X-ray diffraction (XRD) and high-resolution scanning transmission microscopy (HR-STEM). I have found that the interface between the $TmFe_2O_4$ thin film and the YSZ substrate exhibits a unique structure; Tm^{3+}-rich layer and very thin layer of hexagonal $TmFeO_{3-\delta}$ phase are formed at the interface. Because of such an interface structure, exchange bias (EB) effect is observed at 100 K in the magnetic field dependence of magnetization, while the $TmFe_2O_4$ thin film itself shows spin or cluster glass behavior.

3.2 Sample fabrication

For the deposition of epitaxial thin films by using the PLD method, a polycrystalline $TmFe_2O_4$ target was synthesized from Tm_2O_3 (Nippon Yttrium Co. Ltd., Japan, 99.9 %) and Fe_2O_3 (Kojundo Chemical Laboratory Co. Ltd., Japan, 99.99 %) as starting materials. Tm_2O_3 powder was first heated at 1173 K for 12 h to remove absorbed water. The starting

materials were weighted in stoichiometric ratio and mixed in an agate mortar. The mixed

powder was pressed into a pellet and then heated at 1473 K for 24 h in a CO: CO_2

atmosphere (molar ratio CO: CO_2 = 1: 2). After preparing the target, XRD was carried

out to identify the crystalline phase. The molar ratio of Fe to Tm was evaluated using

inductively coupled plasma-atomic emission spectroscopy (ICP-AES). The results are

shown in Table 3.1. The $TmFe_2O_4$ pellet thus obtained was used as a target for the

deposition of the thin films.

PLD technique was used for the preparation of epitaxial $TmFe_2O_4$ thin film. A pulsed

KrF excimer laser (wavelength: 248 nm) was used for the deposition of $TmFe_2O_4$ thin

film on (111) plane of 9.0 mol % Y_2O_3-bearing YSZ substrate (SHINKOSHA, Co. Ltd.,

Japan). The YSZ substrates were first annealed at 1623 K to obtain a smooth surface at

an atomic level. The full-width at half maximum (FWHM) obtained from the rocking

curve of YSZ substrate was evaluated to be 0.0305° (see Figure 3.2 in the Supporting

Information). The target was set 3.5 cm away from the substrate. The substrate

temperature was maintained at about 1123 K throughout the deposition, and was

continuously monitored by an optical pyrometer. The thin film was deposited with a laser

energy density of about 2.5 Jcm^{-2} and a repetition rate of 3 Hz. The duration of deposition

was 60 min. The oxygen partial pressure in the chamber was varied from 2.00 $\times$ 10^{-5} to

2.00 $\times$ 10^{-3} Pa.

3.3 Characterization

The crystal structure and lattice plane orientations of the thin film were analyzed by

Cu Kα XRD using a four-circle Rigaku SmartLab diffractometer equipped with Ge(220) × 2 monochromator and analyzer crystals. Rutherford backscattering spectroscopy (RBS) was carried out using 2.0 MeV He^+ to determine the thickness and chemical composition of the thin films. The analysis with the simulation program SIMNRA revealed that the thin film thickness was about 99.3(2) nm and that the ratio of Tm to Fe was typically 1: 1.66, indicating that a substantial amount of iron was evaporated during the thin film deposition process. Cross-sectional samples for transmission electron microscopy (TEM) were prepared by milling with a focused ion beam (FIB). HAADF-STEM images were acquired on a 300 keV ThermoScientific Titan[3] 60-300 with double corrector, and EDX spectroscopy was carried out by using Super-X detector. The DCFI (Drift Corrected Frame Integration 512 × 512, dwelltime 1μsec×50frame) HAADF image was collected with a detection angle of 82-200 mrad and a current of 40 pA. The energy resolution defined as the height at the full width at half-maximum of the zero-loss peak was ~0.3 eV. The convergence semi-angle of the electron probe was 13.1 mrad, and atomically resolved EELS data were acquired with a collection semi-angle of 27.3 mrad. A small convergence semi-angle like 13.1 mrad was selected to improve the energy resolution and to make a spot size of electron beam as small as possible so as to avoid a damage caused by the electron beam irradiation. The surface morphology of YSZ substrate as well as $TmFe_2O_4$ thin film was examined by atomic force microscopy (AFM, Seiko SPI 3800) equipped with a cantilever (OMCL-AC240TS-C3, Olympus Corp.) with a spring constant of 1.7 N m^{-1} and a resonant frequency of 70 kHz).

Magnetic measurements were performed with a superconducting quantum interference

device (SQUID) magnetometer (Quantum Design MPMS-SQUID). Temperature dependence of magnetization was measured with external dc magnetic fields of 1 to 10 kOe parallel to the c-axis, i.e., perpendicular to the film surface, in FC and ZFC runs. For the ZFC measurements, the sample was cooled to 50 K in the absence of an external magnetic field. For the FC measurements, an external magnetic field was applied perpendicular to the surface of the film during the cooling-down process. Magnetization as a function of magnetic field was measured at 100 to 300 K by applying magnetic fields up to ±50 kOe. Also, aging-memory effect was examined in the ZFC run. Detailed procedure is described in the above sections. For all the magnetic measurements, magnetizations of bare YSZ substrate was subtracted from those of the samples in order to determine the intrinsic magnetizations of the $TmFe_2O_4$ thin films.

3.4 Results and discussion

3.4.1 Structure and composition

Figure 3.2 (b) illustrates a possible growth mode of $TmFe_2O_4$ thin film on YSZ containing 9.0 mol % Y_2O_3 used as a substrate. Although there are several compounds which can be used as a substrate for thin films with a hexagonal structure, YSZ (111) has the smallest lattice mismatch with $TmFe_2O_4$ (~4.44 %). It is also important to evaluate the lattice mismatch at high temperatures like 1123 K, which is the substrate temperature during the PLD process, as well as at room temperature so that the effect of thermal expansion is taken into account. The thermal expansion coefficient averaged between 298 and 1273 K for YSZ containing 8 mol% Y_2O_3 was reported to be 10.5 × 10^{-6} K^{-1}.[32] Also,

the thermal expansion coefficient of YSZ containing 10mol % Y_2O_3 is about 10^{-5} K^{-1} at 800 K.[33] On the other hand, to the best of my knowledge, the thermal expansion coefficient of $TmFe_2O_4$ was not reported, but data of lattice constants at various temperatures are available for $LuFe_2O_4$, although they are limited to a temperature range below 400 K.[34] The thermal expansion coefficient evaluated from the temperature dependence of lattice constant (a-axis) is about 10^{-5} K^{-1} at 300 to 400 K, which is similar to the values of YSZ. Hence, although this is a rather rough estimation, the lattice mismatch between $TmFe_2O_4$ and YSZ at 1123 K is not so different from that at room temperature, suggesting that the effect of thermal expansion is probably not so significant.

The effect of oxygen partial pressure on the crystalline phases formed in thin films is found in the XRD patterns depicted in Figure 3.2 (c). As shown in the figure, the oxygen partial pressure plays an important role in the thin film growth, and well-defined XRD peaks with c-axis orientation assigned to $TmFe_2O_4$ appear at 1.85×10^{-4} Pa, which is slightly lower than the oxygen partial pressure utilized for the deposition of $LuFe_2O_4$ thin films ($\sim 2.00 \times 10^{-4}$ Pa).[35] Although a very weak peak assigned to hexagonal $TmFeO_3$ (h-$TmFeO_3$) is observed at the oxygen pressure of 1.85×10^{-4} Pa, the linewidth of the diffraction peaks is rather broad, suggesting that the crystalline quality of the $TmFe_2O_4$ phase is rather good. When the oxygen partial pressure is 2.00×10^{-4} Pa, the intensity of diffraction peak assigned to h-$TmFeO_3$ phase becomes larger and the linewidth of the diffraction peaks grows broader due to the $TmFe_2O_4$ phase. On the other hand, h-$TmFeO_3$ and Fe_3O_4 phases were formed at 2.00×10^{-3} Pa, which indicates that high oxygen partial pressure can easily decompose $TmFe_2O_4$ into other phases with oxidized state of

iron ions. Based on the oxygen partial pressure dependence of formed crystalline phases, the thin film deposited at 1.85×10^{-4} Pa was used for the subsequent measurements.

The length of c-axis and the full-width at half maximum (FWHM) of rocking curve corresponding to (0003) diffraction peak of $TmFe_2O_4$ are estimated to be 24.954 Å and 0.5046°, respectively (see the inset of Figure 3.2 (c)). The latter is somewhat smaller than those observed for $LuFe_2O_4$ thin films,[26] indicating that the present $TmFe_2O_4$ thin film has good crystalline quality. The in-plane heteroepitaxial relationship between the $TmFe_2O_4$ thin film and the YSZ substrate was further confirmed by a two-dimensional reciprocal space mapping (RSM) as shown in Figure 3.2 (d). It is found that the thin film is epitaxially grown with the relationship of (0001) [1100] $TmFe_2O_4$// (111) [112] YSZ. On the other hand, the diffraction peak of h-$TmFeO_3$-like phase which is observed in the out-of-plane XRD pattern is not detected because of its low intensity of diffraction peak. The evaluated lattice constants and cell volume of the present thin film are summarized and compared to the values of bulk $TmFe_2O_4$ in Table 3.2. The in-plane lattice constants are similar to the values of single-crystalline $TmFe_2O_4$, suggesting that the lattice of $TmFe_2O_4$ thin film is not fixed to the YSZ substrate but is relaxed. Furthermore, the surface morphology of YSZ substrate and $TmFe_2O_4$ thin film was examined by using atomic force microscopy (AFM). The results are illustrated in Figure 3.3. The roughness of YSZ substrate and $TmFe_2O_4$ thin film was evaluated to be about 0.64 nm and 33.3 nm, respectively. In order to reflect the growth mode of the present thin film, the measured area of $TmFe_2O_4$ thin film (5 μm × 5 μm) was made to be larger than that of the substrate (1 μm × 1 μm). The results exhibit that the present thin film was formed by a typical

three-dimensional island growth mechanism. In other words, the $TmFe_2O_4$ thin films was

not fixed by the layer beneath the thin film but a stress or a strain otherwise applied to the

thin film was released.

A more detailed clarification of the structure at atomic level was performed using high-

resolution high-angle annular dark field scanning TEM (HAADF-STEM). In this work, I

focused on the $TmFe_2O_4$/YSZ interface. In a HAADF-STEM image, the contrast reflects

the atomic number of elements, and hence, a heavier element is observed as a brighter

spot. Figure 3.4 (a) shows the low-magnification image of $TmFe_2O_4$ thin film when

viewed along [1120] direction. The inset depicts the magnified image which clearly

exhibits a sequence of Fe-O bilayers separated by Tm-O monolayers, indicating that the

thin films of $TmFe_2O_4$ phase is epitaxially grown along the *c*-orientation. However, the

interface between $TmFe_2O_4$ phase and YSZ substrate exhibits a rather irregular structure,

as shown in Figure 3.4 (b) and (c). Figure 3.4 (b) illustrates a magnified HAADF-STEM

image of the interface. The colors in this figure represent the different elements identified

by energy dispersive X-ray (EDX) spectroscopy. Figure 3.4 (c) shows a distribution of

each element across the interface between the substrate and the thin film. The ordinate in

this figure denotes the intensity of X-ray emitted from each of the elements. In the region

corresponding to the YSZ substrate, which is the leftmost side in Figure 3.4 (c), only Zr

is observed as expected. On the other hand, the number of Tm increases as the Zr

concentration decreases at the surface of the YSZ substrate (the region surrounded by a

pale blue rectangle in Figure 3.4 (a) and (c)). Furthermore, a very thin layered region

consisting of a few single Fe-O and Tm-O layers stacked alternately is observed adjacent

to the Tm^{3+}-rich layer (the region surrounded by an orange rectangle in Figure 3.4 (a) and (c)). It is inferred that the very thin layered region has a chemical composition corresponding to h-$TmFeO_3$ phase.

Thus, the average concentration of Fe gradually deviates from the stoichiometric composition of $TmFe_2O_4$ and decreases from the region of $TmFe_2O_4$ phase to the surface region of the YSZ substrate in the present thin film. This suggests that Fe atoms disappear at the early state of the deposition. Although the exact reason why such a phenomenon occurs is unclear at this moment, I speculate that the volatilization of Fe species takes place at the surface of the YSZ substrate. Wang et al. suggested that a difference in residence time (τ_{ad}) of adsorbed atoms might induce the deviation of composition from the stoichiometry of the target.[36] The τ_{ad} can be represented by the equation

$$\tau_{ad} = \frac{1}{\nu}\exp(\frac{E_{des}}{kT}),$$

where υ is the vibrational frequency and E_{des} is the desorption energy, respectively. It is thought that E_{des} is lower for Fe than for Tm, so the Fe atoms are easily detached at the initial stage of the thin film growth process. Besides, the different laser ablation rate of Fe and Tm in the target also might be related to the formation of Fe deficient phase.[24] Although the effect of the residence time is crucial only at the initial step of the deposition, at which both Tm and Fe species reach the surface of the YSZ substrate, it is considered that once the Tm^{3+}-rich layer is formed at the surface of the YSZ, it plays a role of a nucleating agent for further growth of Tm^{3+}-rich phase, leading to the formation of the

layer with several nanometers. At the same time, the difference in the residence time between Fe and Tm becomes less effective, and eventually, Fe as well as Tm species begin to condense. As for the formation of Tm^{3+}-rich layer at the surface region of the YSZ substrate, a similar phenomenon was reported for hexagonal $YbFeO_3$ (h-$YbFeO_3$) thin film. Iida et al. observed amorphous layer that seems to be composed of a substantial amount of Yb^{3+} ions at the interface of h-$YbFeO_3$/YSZ system and considered that the amorphous layer contributed to the relaxation of the thin film.[37] Similarly, the present Tm^{3+}-rich phase may act as a buffer layer to compensate the large lattice mismatch between the thin film and the substrate.

Also, a closer look at Figure 3.4 (b) disclosed that a displacement of cations, or an ionic polarization, does not occur in the region corresponding to the h-$TmFeO_{3-\delta}$ phase although it was reported that h-$TmFeO_3$ thin film 60 nm thick deposited on a Pt (111)/Al_2O_3 (0001) substrate by the PLD method exhibits ferroelectricity with Curie temperature of 430 K.[38] This is presumably because the present h-$TmFeO_{3-\delta}$ phase is too thin to show spontaneous polarization. A similar phenomenon was observed for a thin film of $YMnO_3$ which has the same space group as h-$RFeO_3$. Cheng et al.[39] fabricated $YMnO_3$ thin film on c-oriented Al_2O_3 substrate by using the PLD technique and clarified that the displacement of Y^{3+} ions, which leads to the spontaneous polarization in $YMnO_3$, is suppressed near the interface. They argued that the polarization at the interface between $YMnO_3$ and Al_2O_3 might be compensated by the interfacial charges. A similar arrangement of Tm^{3+} ions is plausible at the thin layer of h-$TmFeO_{3-\delta}$ phase formed at the interface of the present thin film sample.

In order to further disclose the chemical states of constituent elements in the region from the surface of the thin film to the substrate involving the interface and to speculate the growth mechanism of the thin film, EEL spectra were obtained by the analysis of energy loss near-edge structure (ELNES). The EEL spectra were gleaned at the O K-edge to elucidate the local bonding environment of oxygen in different positions of the thin film, substrate, and the interface. Figure 3.5 (a) illustrates the HAADF-STEM image. Here, the positions for which EEL spectra were obtained are indicated by O_1 to O_6. Figure 3.5 (b) depicts the O K-edge ELNES taken at six points from the surface of $TmFe_2O_4$ thin film (O_1) to the YSZ substrate (O_6) as shown in Figure 3.5 (a). The spectrum taken at the point O_6 (a black curve in Figure 3.5 (b)) distinctly exhibits two peaks denoted as P_1 and P_2 .These peaks are induced by the crystal field splitting of Zr $4d$ into e_g (P_1) and t_{2g} (P_2) orbitals.[40] For the Tm^{3+}-rich layers at the upper side of substrate (point O_5 , a sky blue curve in Figure 3.5 (b)), however, the doublet peaks shift towards higher energy loss side, i.e., P_4 and P_5 peaks, compared to the substrate peaks. The shift of peaks suggests that Tm-O bond is formed since the peaks of P_4 and P_5 are caused by the hybridization between O $2p$ and Tm $5d$ orbitals.[41] Another peak close to 530 eV denoted as P_3 is observed from O_3 (an orange curve in Figure 3.5 (b)) to O_1, (a yellow curve in Figure 3.5 (b)), which represents the hybridization of the O $2p$ orbitals and the Fe $3d$ orbitals, corresponding to the formation of a phase containing Tm, Fe, and O. It is found that the intensity of P_3 peak is larger at O_1 than at O_2 and O_3. This peak stems from the hybridization of O 2p and Fe 3d orbitals, so that the difference in the peak intensity reflects the different electronic configurations of iron ions bonded to the oxide ions. I

consider that iron ions at the surface of $TmFe_2O_3$ thin film, namely, those at O_1 are more easily oxidized than the iron ions at O_2 and O_3, that is, inside the thin film because the surface of the thin films is exposed to the air. Such a difference in oxidation state of iron ions is thought to be reflected in the difference in intensity of P_3 peak.

For further analysis, spectra of Fe $L_{2,3}$-edge were obtained in order to identify the composition of very thin interfacial layer that is composed of Tm-O and Fe-O monolayers as illustrated in the inset of Figure 3.5 (c). In this measurement, Fe_2O_3 (hematite) and FeO (wüstite) were used as reference peaks of Fe^{3+} and Fe^{2+}, respectively. These iron oxides have been usually utilized a reference materials for EEL spectra of Fe^{3+} and Fe^{2+}.[42,43] They are denoted by black and sky blue curves, respectively, in Figure 3.5 (c). Fe_2O_3 shows a main peak at ~710.0 eV with a pre-peak at ~708.0 eV characteristic of Fe L_3-edge.[42] On the other hand, L_3-peak of FeO exhibits ~2 eV chemical shift to lower energy side compared to the peak of Fe^{3+}. The spectra for the thin film sample were acquired from iron ions within the Fe-O monolayers at the interface region. The results indicate the presence of both Fe^{2+} and Fe^{3+} ions. One reason why Fe^{2+} as well as Fe^{3+} ions are present in the layer the composition of which corresponds to h-TmFeO$_3$ is a possibility that Fe^{3+} was reduced into Fe^{2+} by the high energy electron beam irradiation during the process to acquire the EEL spectra, as suggested by Masina et al.[42] Also, I cannot rule out a possibility that oxygen-deficient hexagonal $TmFeO_3$ (h-TmFeO$_{3-\delta}$) phase might be formed by the high energy supplied in the PLD process.[44] Although the reason why the shape of EEL spectra are somewhat different from each other; in particular, the spectrum denoted by the purple curve in Figure 3.5 (c) is rather different from others is unclear, it

might be attributed to the reduction of Fe^{3+} into Fe^{2+} by the electron beam irradiation as described above.

Thus, I suggest a possible growth mechanism of $TmFe_2O_4$ thin film with interfacial structure in the $TmFe_2O_4$/YSZ system as illustrated in Figure 3.6. The deposition process is thought to include three major steps. Figure 3.6 (a) depicts the first step, in which Fe and Tm atoms simultaneously bombarded out from the target material are supposed to reach the surface of the YSZ substrate. However, the different residence time between Fe and Tm might induce the preferential detachment of Fe atoms from the substrate. First, it is possible that Tm^{3+} ions are incorporated into the surface region of YSZ substrate by replacing the Zr^{4+} and/or Y^{3+} ions because these three kinds of ions have similar ionic radii to each other. Since the substrate temperature, i.e., 1123 K, is not high enough to lead to the diffusion of Tm^{3+} ion into the YSZ substrate, it is plausible that the kinetic energy in the bombardment process injects Tm^{3+} ions into the surface region of the YSZ substrate. Another possibility is that bixbyite-type cubic Tm_2O_3 phase[45] is formed on the surface that is akin to a fluorite structure the YSZ adopts. The lattice mismatch between YSZ and cubic Tm_2O_3 (about 1.9 %) is smaller than the lattice mismatch between $TmFe_2O_4$ and YSZ, which is 4.44 % as mentioned above, suggesting that the Tm^{3+}-rich phase might work as a buffer layer.

Afterwards, iron and oxygen deficient phase, h-$TmFeO_{3-\delta}$ layer, is generated at the early stage of the deposition process. This speculation is proved by the XRD, HAADF-STEM image, and EELS results. As illustrated in Figure 3.6 (b) and (c), $TmFe_2O_4$ eventually starts to from on the h-$TmFeO_{3-\delta}$ layer. Although the existence of interfacial

layer is inevitable and further investigation is needed to determine the behavior of Fe atoms, the influence from the interface gradually becomes negligible as the thickness of thin film is increased and the coexistence of different layers might induce a change in physical properties. Besides, the oxygen off-stoichiometry in $TmFe_2O_4$ phase affect the non-equilibrium magnetic glassy dynamics observed in the present thin film, as mentioned below.

3.4.2 Magnetic properties

The coexistence of different phases, i.e., $TmFe_2O_4$ and h-$TmFeO_{3-\delta}$ in the present case, can have an influence on the physical properties involving magnetic properties as observed in $LuFe_2O_4$/$LuFeO_3$ superlattice system.[23] Figure 3.7 (a) shows the temperature dependence of field-cooled (FC) and zero-field-cooled (ZFC) magnetizations (M-T curves, where M is the magnetization and T is the temperature) measured at 1 kOe. The FC and ZFC curves coincide completely with each other at higher temperatures, but bifurcate into two curves below a certain temperature, T_{irr}. A sudden increase in magnetization around 250 K, observed in both FC and ZFC curves, is ascribable to the onset of long-range magnetic ordering (ferrimagnetic state) from paramagnetic state. The Néel temperature (T_N) derived from the first-order temperature derivative of magnetization (indicated in the inset of Figure 3.7 (a)), is about 234 K. In addition, the temperature dependence of ZFC magnetization (shown in Figure 3.7 (a)) takes a maximum at about 220 K. The large difference in magnetization between FC and ZFC processes at low temperatures and the occurrence of a maximum in the ZFC

magnetization imply that the system might undergo a spin (or cluster) glass phase transition below 220 K. This phenomenon is discussed below.

The magnetic field dependence of magnetization (M-H loop, where H is the magnetic field) was measured at temperatures of 100, 150, 200, 250, and 300 K. The results are shown in Figure 3.7 (b). It is found that the magnetization is not saturated even at a magnetic field of 50 kOe. Such a phenomenon was observed for other RFe$_2$O$_4$ compounds including thin films[31] because of its hard magnetic behavior that can be explained by a model that the electron diffusion between Fe^{2+} and Fe^{3+} ions ceases at low temperature and a distribution of iron ions with different valence states on the two AFM sublattices is fixed.[46] Interestingly, the shift of M-H curve is observed at 100 K, indicating the EB effect occurs. Such a shift vanishes above 150 K. The EB effect has inspired many researches since it was first discovered by Meiklejohn and Bean in oxidized cobalt particles.[47] The EB effect usually occurs at an interface between two different magnetic phases and manifests itself as a shift of the hysteresis loop along the magnetic fields. In this work, the M-H loop (blue curve) was measured after cooling at +30 kOe field from room temperature to 100 K. A shift of the loop is observed along the magnetic field axis toward negative fields. On the other hand, on cooling at -30 kOe field (red curve), the loop is biased in the positive direction. The results are shown in the inset of Figure 3.7 (b). An EB field (H_{EB}) is defined as $H_{EB} = |(H_1 + H_2)/2|$, where H_1 (H_2) represents the negative (positive) coercive field. It is noteworthy that about 1.1 kOe of EB effect is obtained at 100 K in the present TmFe$_2$O$_4$ thin film. The observed EB effect at 100 K might be caused by the spin competition between the interfacial h-TmFeO$_{3-\delta}$ layer and

TmFe$_2$O$_4$ phase, although further studies are necessary on physical properties of oxygen deficient h-TmFeO$_3$ phase. This value is relatively large compared to the EB effect of ferrimagnetic Fe$_3$O$_4$ nanoparticle with core/shell structure[48,49] or thin film with heterosctructure.[50,51] This idea comes from the fact that according to the previous study, h-TmFeO$_3$ thin film on Pt-buffered (0001)-Al$_2$O$_3$ substrate showed the robust canted AFM order along the c-axis below 120 K.[38]

On the other hand, it has been reported that the minor loop might also induce a phenomenon similar to EB effect, if the applied magnetic field is not sufficient to reverse the magnetization of ferromagnetic (FM) phase.[52,53] Hence, the EB effect in unsaturated M-H loop as indicated in Figure 3.7 (b) needs to be further verified. In this case, the training effect ensures that the shift of hysteresis loop originates in not minor loop effect but EB effect.[53] The training effect indicates that the consecutive M-H loops with a number of times (n) cause the relaxation of uncompensated spins at the interface and then makes the symmetric M-H loop. For the present thin film, the magnetic hysteresis loops were measured at 100 K after FC at +30 kOe and the result of training effect can be seen in Figure 3.7 (c). The shift of consecutive M-H loops is prominent at the left part of a loop, and in contrast, the right part shows only slight shifts, similarly to the results of previous studies.[54,55] Also, the asymmetry and H_{EB} are gradually reduced from the second to fifth loops. Such a relaxation feature is remarkable in the inset of Figure 3.7 (c) which shows the relationship between H_{EB} and n. In general, this relationship can be expressed in terms of the following empirical power law:[56,57]

$$H_{\text{EB}}(n) - H_{\text{EB},\infty} \propto \frac{1}{\sqrt{n}},$$

where $H_{\text{EB}}(n)$ and $H_{\text{EB},\infty}$ are the magnitudes of the EB field for the nth cycle and in the limit of infinite loops, respectively. The experimental data are well described by the power law, indicating that the intrinsic EB field exists in the present $TmFe_2O_4$ thin film with h-$TmFeO_{3-\delta}$-like interface structure. The value of $H_{\text{EB},\infty}$ has been found to be 241 Oe from the fitting of the above equation to the experimental data.

In general, the EB effect is easy to observe in a system that is composed of FM-spin (or cluster) glass or system and FM-AFM interface when the system is cooled in FC process through the freezing temperature of the glassy phase or the T_N of AFM.[55–59] In the present case, the coexistence of canted AFM (weak FM) in the h-$TmFeO_{3-\delta}$ phase and spin (or cluster) glass phase in the oxygen off-stoichiometric $TmFe_2O_4$ phase can cause a magnetic phase boundary at 100 K that is lower than T_N (~120 K). This might be a possible origin of EB effect. The number density of interface is low in the present sample, but the thickness of $TmFe_2O_4$ is large enough to cause the EB effect at the interface between $TmFe_2O_4$ and h-$TmFeO_{3-\delta}$ layer. Shiratsuchi et al.[60] examined perpendicular EB effect for FM Pt/Co thin film deposited on AFM Cr_2O_3 thin film with the thickness of Cr_2O_3 thin film varied and found that the temperature at which the EB effect occurs is increased with an increase in the thickness of Cr_2O_3 thin film from 50 to 150 nm while the thickness of the Co layer was kept constant (0.8 nm), suggesting that the thicker Cr_2O_3 thin film more readily causes the EB effect. I speculate that the magnetic moments of iron ions somewhat canted to the c-plane of h-$TmFeO_{3-\delta}$ layer[38] are forced to align along the

direction perpendicular to the film surface because the easy axis of magnetization of the TmFe$_2$O$_4$ thin film is along the *c*-axis. The thickness of the TmFe$_2$O$_4$ thin film, i.e., 99.3(2) nm, is thought to be large enough to lead to the EB effect.

Meanwhile, the hysteresis loop persists even at 300 K and the reason might be relevant to some iron oxide impurities at the surface of one of my TmFe$_2$O$_4$ thin films (Figure 3.8). However, EB effect and spin (or cluster) glass behavior are not related to the impurities because the observed iron oxides undergo magnetic transitions well above room temperature.

As mentioned above, the temperature dependence of FC and ZFC magnetizations suggests that the spin (or cluster) glass-like phase transition occurs in the present thin film. Although this behavior of FC and ZFC magnetizations is common in many systems where the magnetic frustration occurs, the existence of frozen glassy state needs to be further verified. In this work, I measured *M-T* curves under various dc magnetic fields of 1, 3, 5, 7 and 10 kOe. The results are shown in Figure 3.9 (a). It is found that both FC and ZFC magnetizations increase and the T_{irr} monotonically decreases with increasing applied magnetic field. This behavior suggests that the frozen spin state is suppressed by strong magnetic fields.[59] A detailed analysis of the magnetic field dependence of irreversibility transition temperature (T_{irr}) indicates that T_{irr} varies almost linearly with $H^{2/3}$, as demonstrated in Figure 3.9 (b). Namely, the relation follows the de Almeida-Thouless line (AT line), i.e., $H(T_{irr})/\Delta J \propto (1-T_{irr}/T_F)^{3/2}$, where T_F is the spin-freezing temperature and ΔJ is the distribution width of the exchange interaction.[61] The result confirms that the spin (or cluster) glass phase transition occurs in the present TmFe$_2$O$_4$ thin film.

Generally, the alternating current susceptibility (AC-χ) measurement is a conventional method to prove the spin glass state. However, a peak of AC-χ related to the spin glass transition was not clearly observed in my measurements of the $TmFe_2O_4$ thin films because the magnetic signal was too weak compared to the background noise of the DC mode in SQUID. In order to further clarify the spin (or cluster) glass state in the present thin film, I have carried out experiments of aging-memory effect proposed by Mathieu et al.[62] The measurement procedure is as follows. The thin film was first cooled in the absence of a magnetic field from 270 K at a rate of 2 K/min, and kept for 6 h at an intermittent stop temperature (T_S) lower than the spin-freezing temperature. In the present case, T_S was set to 180 K. Afterwards, the thin film was cooled again to the lowest temperature of measurement, and the magnetic susceptibilities were measured in a weak dc magnetic field while the temperature was raised at a rate of 2 K/min. The resultant aging-memory effect is presented in Figure 3.10. The magnetization after aging deviates downward from the normal ZFC magnetization as the temperature becomes close to the T_S. The two curves merge with each other in a range above T_S as the temperature increases. The difference between the two curves is shown in the upper part of Figure 3.10. The aging effect is reflected by a dip at around T_S. The observed aging-memory effect can be an additional evidence for spin (or cluster) glass transition. Similarly to $LuFe_2O_4$[16–19] and $YbFe_2O_4$ bulks,[63,64] it is suggested that geometrical frustration with oxygen off-stoichiometry leads to the strengthening of magnetic frustration and gives rise to the spin (or cluster) glass phase transition in the oxygen nonstoichiometric $TmFe_2O_4$ phase.

3.5 Conclusion

I successfully synthesized epitaxial $TmFe_2O_4$ thin film with self-assembled interfacial h-$TmFeO_{3-\delta}$ phase on (111)-oriented YSZ substrate by using a pulsed laser deposition technique. The out-of-plane X-ray diffraction and reciprocal space mapping demonstrate that c-axis oriented thin film grows with the epitaxial relationship of $(0001)[1\overline{1}00]TmFe_2O_4//(111)[11\overline{2}]$YSZ. The high-resolution HAADF-STEM reveals that a Tm^{3+}-rich layer and a very thin h-$TmFeO_{3-\delta}$ layer are formed at the interface between the $TmFe_2O_4$ thin film and the YSZ substrate. The thin film undergoes ferrimagnetic transition at 234 K and exhibits spin (or cluster) glass transition at around 220 K. The latter is confirmed by the fact that the dc magnetic field dependence of the irreversibility temperature follows the de Almeida-Thouless line and that the aging-memory effect is clearly observed. The origin of glassy behavior is thought to be the strengthened magnetic frustration by the oxygen off-stoichiometry in $TmFe_2O_4$ phase. Furthermore, the exchange bias effect is observed in the magnetic field dependence of magnetizations at 100 K due to the spin competition between the $TmFe_2O_4$ phase and the interfacial h-$TmFeO_{3-\delta}$ phase. The effect of field cooling and training cycle ascertains that the shift of hysteresis loops observed in the present thin film is not ascribed to the unsaturated minor loop but due to the intrinsic EB effect.

References in chapter 3

1. N. A. Spaldin and M. Fiebig, *Science*, 2005, **309**, 391–392.

2. K. F. Wang, J.-M. Liu and Z. F. Ren, *Adv. Phys.*, 2009, **58**, 321–448.

3. W. Eerenstein, N. D. Mathur and J. F. Scott, *Nature*, 2006, **442**, 759–765.

4. N. A. Hill, *J. Phys. Chem. B*, 2000, **104**, 6694–6709.

5. J. Wang, J. B. Neaton, H. Zheng, V. Nagarajan, S. B. Ogale, B. Liu, D. Viehland, V. Vaithyanathan, D. G. Schlom, U. V. Waghmare, M. Wuttig and R. Ramesh, *Science*, 2003, **299**, 1719–1722.

6. T. Kimura, T. Goto, H. Shintani, K. Ishizaka, T. Arima and Y. Tokura, *Nature*, 2003, **426**, 55–58.

7. H. J. Zhao, W. Ren, Y. Yang, J. Íñiguez, X. M. Chen and L. Bellaiche, *Nat. Commun.*, 2015, **5**, 4021.

8. N. Kimizuka, A. Takenaka, Y. Sasada and T. Katsura, *Solid State Commun.*, 1974, **15**, 1321–1323.

9. N. Ikeda, H. Ohsumi, K. Ohwada, K. Ishii, T. Inami, K. Kakurai, Y. Murakami, K. Yoshii, S. Mori, Y. Horibe, Y. Horibe and H. Kitô, *Nature*, 2005, **436**, 1136–1138.

10. T. Mueller, J. De Groot, J. Strempfer and M. Angst, *J. Cryst. Growth*, 2015, **428**, 40–45.

11. M. A. Subramanian, T. He, J. Chen, N. S. Rogado, T. G. Calvarese and A. W. Sleight, *Adv. Mater.*, 2006, **18**, 1737–1739.

12. A. Nagano, M. Naka, J. Nasu and S. Ishihara, *Phys. Rev. Lett.*, 2007, **99**, 217202.

13. H. J. Xiang and M.-H. Whangbo, *Phys. Rev. Lett.*, 2007, **98**, 246403.

14. Y. Zhang, H. X. Yang, C. Ma, H. F. Tian and J. Q. Li, *Phys. Rev. Lett.*, 2007, **98**, 247602.

15. K. Siratori, in *Proc. 6th Int. Conf. on Ferrites; The Japan Society of Powder and Powder Metallurgy*, 1992, 703.

16. A. D. Christianson, M. D. Lumsden, M. Angst, Z. Yamani, W. Tian, R. Jin, E. A. Payzant, S. E. Nagler, B. C. Sales and D. Mandrus, *Phys. Rev. Lett.*, 2008, **100**, 107601.

17. F. Wang, J. Kim, Y.-J. Kim and G. D. Gu, *Phys. Rev. B*, 2009, **80**, 024419.

18. M. H. Phan, N. A. Frey, H. Srikanth, M. Angst, B. C. Sales and D. Mandrus, *J. Appl. Phys.*, 2009, **105**, 07E308.

19. M. H. Phan, N. A. Frey, M. Angst, J. de Groot, B. C. Sales, D. G. Mandrus and H. Srikanth, *Solid State Commun.*, 2010, **150**, 341–345.

20. J. De Groot, K. Marty, M. D. Lumsden, A. D. Christianson, S. E. Nagler, S. Adiga, W. J. H. Borghols, K. Schmalzl, Z. Yamani, S. R. Bland, Y. Su and M. Angst, *Phys. Rev. Lett.*, 2012, **108**, 037206.

21. N. Reyren, S. Thiel, A. D. Caviglia, L. Fitting Kourkoutis, G. Hammerl, C. Richter, C. W. Schneider, T. Kopp, A.-S. Rüetschi, D. Jaccard, J.-M. Triscone and J. Mannhart, *Science*, 2007, **317**, 1196–1199.

22. H. Ohta, S. Kim, Y. Mune, T. Mizoguchi, K. Nomura, S. Ohta, T. Nomura, Y. Nakanishi, Y. Ikuhara, M. Hirano, H. Hosono and K. Koumoto, *Nat. Mater.*, 2007, **6**, 129–134.

23. J. A. Mundy, C. M. Brooks, M. E. Holtz, J. A. Moyer, H. Das, A. F. Rébola, J. T. Heron, J. D. Clarkson, S. M. Disseler, Z. Liu, D. A. Muller and D. G. Schlom, *Nature*,

2016, **537**, 523–527.

24. J. Liu, Y. Wang and J. Y. Dai, *Thin Solid Films*, 2010, **518**, 6909–6914.

25. R. C. Rai, A. Delmont, A. Sprow, B. Cai and M. L. Nakarmi, *Appl. Phys. Lett.*, 2012, **100**, 212904.

26. C. M. Brooks, R. Misra, J. A. Mundy, L. A. Zhang, B. S. Holinsworth, K. R. O'Neal, T. Heeg, W. Zander, J. Schubert, J. L. Musfeldt, P. Schiffer and D. G. Schlom, *Appl. Phys. Lett.*, 2012, **101**, 132907.

27. K. Fujiwara, T. Hori and H. Tanaka, *J. Phys. D: Appl. Phys.*, 2013, **46**, 155108.

28. R. Kashimoto, T. Yoshimura, A. Ashida and N. Fujimura, *Thin Solid Films*, 2016, **614**, 44–46.

29. T. Fujii, T. Numata, H. Nakahata, M. Nakanishi, J. Kano and N. Ikeda, *Jpn. J. Appl. Phys.*, 2017, **57**, 010305.

30. T. Fujii, N. Okamura, H. Hashimoto, M. Nakanishi, J. Kano and N. Ikeda, *AIP Adv.*, 2016, **6**, 085213.

31. M. Seki, T. Konya, K. Inaba and H. Tabata, *Appl. Phys. Express*, 2010, **3**, 105801.

32. I. Yasuda and M. Hishinuma, *Electrochemistry*, 2000, **68**, 526–530.

33. H. Hayashi, T. Saitou, N. Maruyama, H. Inaba, K. Kawamura and M. Mori, *Solid State Ionics*, 2005, **176**, 613–619.

34. Y. Hou, Y. P. Yao, S. N. Dong, M. L. Teng, X. F. Sun and X. G. Li, *J. Raman Spectrosc.*, 2011, **42**, 1695–1700.

35. Y. J. Kim, S. Konishi, Y. Hayasaka, I. Kakeya and K. Tanaka, *CrystEngComm*, 2020, **22**, 1096–1105.

36. W. Wang, Z. Gai, M. Chi, J. D. Fowlkes, J. Yi, L. Zhu, X. Cheng, D. J. Keavney, P. C. Snijders, T. Z. Ward, J. Shen and X. Xu, *Phys. Rev. B*, 2012, **85**, 155411.

37. H. Iida, T. Koizumi, Y. Uesu, K. Kohn, N. Ikeda, S. Mori, R. Haumont, P.-E. Janolin, J.-M. Kiat, M. Fukunaga, M. Fukunaga and Y. Noda, *J. Phys. Soc. Jpn.*, 2012, **81**, 024719.

38. S.-J. Ahn, J.-H. Lee, H. M. Jang and Y. K. Jeong, *J. Mater. Chem. C*, 2014, **2**, 4521–4525.

39. S. Cheng, M. Li, S. Deng, S. Bao, P. Tang, W. Duan, J. Ma, C. Nan and J. Zhu, *Adv. Funct. Mater.*, 2016, **26**, 3589–3598.

40. K. Develos-Bagarinao, H. Yokokawa, H. Kishimoto, T. Ishiyama, K. Yamaji and T. Horita, *J. Mater. Chem. A*, 2017, **5**, 8733–8743.

41. J. A. Mundy, Q. Mao, C. M. Brooks, D. G. Schlom and D. A. Muller, *Appl. Phys. Lett.*, 2012, **101**, 042907.

42. C. J. Masina, J. H. Neethling, E. J. Olivier, S. Manzini, L. Lodya, V. Srot and P. A. Van Aken, *RSC Adv.*, 2015, **5**, 39643–39650.

43. P. Torruella, R. Arenal, F. De La Peña, Z. Saghi, L. Yedra, A. Eljarrat, L. López-Conesa, M. Estrader, A. López-Ortega, G. Salazar-Alvarez, F. Peiró and S. Estradé, *Nano Lett.*, 2016, **16**, 5068–5073.

44. D. Oka and T. Fukumura, *CrystEngComm*, 2017, **19**, 2144–2162.

45. S. Sato, R. Takahashi, M. Kobune and H. Gotoh, *Appl. Catal. A*, 2009, **356**, 57–63.

46. T. Sugihara, T. Katsura, K. Siratori and I. Shindo, *J. Phys. Soc. Jpn.*, 1978, **45**, 1191–1198.

47. W. H. Meiklejohn and C. P. Bean, *Phys. Rev.*, 1956, **102**, 1413.

48. X. Sun, N. Frey Huls, A. Sigdel and S. Sun, *Nano Lett.*, 2012, **12**, 246–251.

49. Y. Ijiri, J. A. Borchers, R. W. Erwin, S.-H. Lee, P. J. van der Zaag and R. M. Wolf, *Phys. Rev. Lett.*, 1998, **80**, 608–611.

50. D. Zheng, M. Sun, D. Li, P. Li, C. Jin and H. Bai, *EPL (Europhysics Letters)*, 2015, **110**, 27005.

51. T. L. Qu, Y. G. Zhao, P. Yu, H. C. Zhao, S. Zhang and L. F. Yang, *Appl. Phys. Lett.*, 2012, **100**, 242410.

52. L. Klein, *Appl. Phys. Lett.*, 2006, **89**, 036101.

53. J. Geshev, *J. Magn. Magn. Mater.*, 2008, **320**, 600–602.

54. C. Binek, *Phys. Rev. B*, 2004, **70**, 014421.

55. S. Karmakar, S. Taran, E. Bose, B. K. Chaudhuri, C. P. Sun, C. L. Huang and H. D. Yang, *Phys. Rev. B*, 2008, **77**, 144409.

56. S. Lin, D. F. Shao, J. C. Lin, L. Zu, X. C. Kan, B. S. Wang, Y. N. Huang, W. H. Song, W. J. Lu, P. Tong, P. Tong and Y. P. Sun, *J. Mater. Chem. C*, 2015, **3**, 5683–5696.

57. X. K. Zhang, J. J. Yuan, Y. M. Xie, Y. Yu, F. G. Kuang, H. J. Yu, X. R. Zhu and H. Shen, *Phys. Rev. B*, 2018, **97**, 104405.

58. R. R. Das, P. Parida, A. K. Bera, T. Chatterji, B. R. K. Nanda and P. N. Santhosh, *Phys. Rev. B*, 2018, **98**, 184417.

59. B. Cui, C. Song, G. Y. Wang, H. J. Mao, F. Zeng and F. Pan, *Sci. Rep.*, 2013, **3**, 2542.

60. Y. Shiratsuchi, T. Fujita, H. Oikawa, H. Noutomi and R. Nakatani, *Appl. Phys. Express*, 2010, **3**, 113001.

61. K. Binder and A. P. Young, *Rev. Mod. Phys.*, 1986, **58**, 801–976.

62. R. Mathieu, P. Jönsson, D. N. H. Nam and P. Nordblad, *Phys. Rev. B*, 2001, **63**, 092401.

63. Y. Sun, Y. Liu, F. Ye, S. Chi, Y. Ren, T. Zou, F. Wang and L. Yan, *J. Appl. Phys.*, 2012, **111**, 07D902.

64. H. Kobayashi, K. Fujiwara, N. Kobayashi, T. Ogawa, M. Sakai, M. Tsujimoto, O. Seri, S. Mori and N. Ikeda, *J. Phys. Chem. Solids*, 2017, **103**, 103–108.

Table 3.1. The molar fractions of Tm and Fe analyzed by ICP-AES for $TmFe_2O_4$ polycrystals prepared under various CO/CO_2 ratios. The compositions of the samples are almost stoichiometric although subtle deviations from the stoichiometry are observed. The values of concentration for Fe and Tm are averaged ones obtained by repeating the measurements three times. The experimental error is within 1 %.

CO/CO_2 molar ratio	Molality of Fe (mol/kg)	Molality of Tm (mol/kg)	Fe/Tm ratio
1	5.56	2.86	1.94
2/3	5.58	2.85	1.96
1/2	5.48	2.80	1.96
1/3	5.38	2.67	2.01
1/4	5.43	2.64	2.05

Table 3.2. Lattice constants and cell volume evaluated from the RSM data for TmFe$_2$O$_4$ thin film, and comparison with those of its bulk form.

|	Bulk	Film	A film / a bulk ratio
a, b (Å)	3.479	3.484	1.001
c (Å)	25.01	24.95	0.998
V (Å^3)	262.1	262.4	1.001
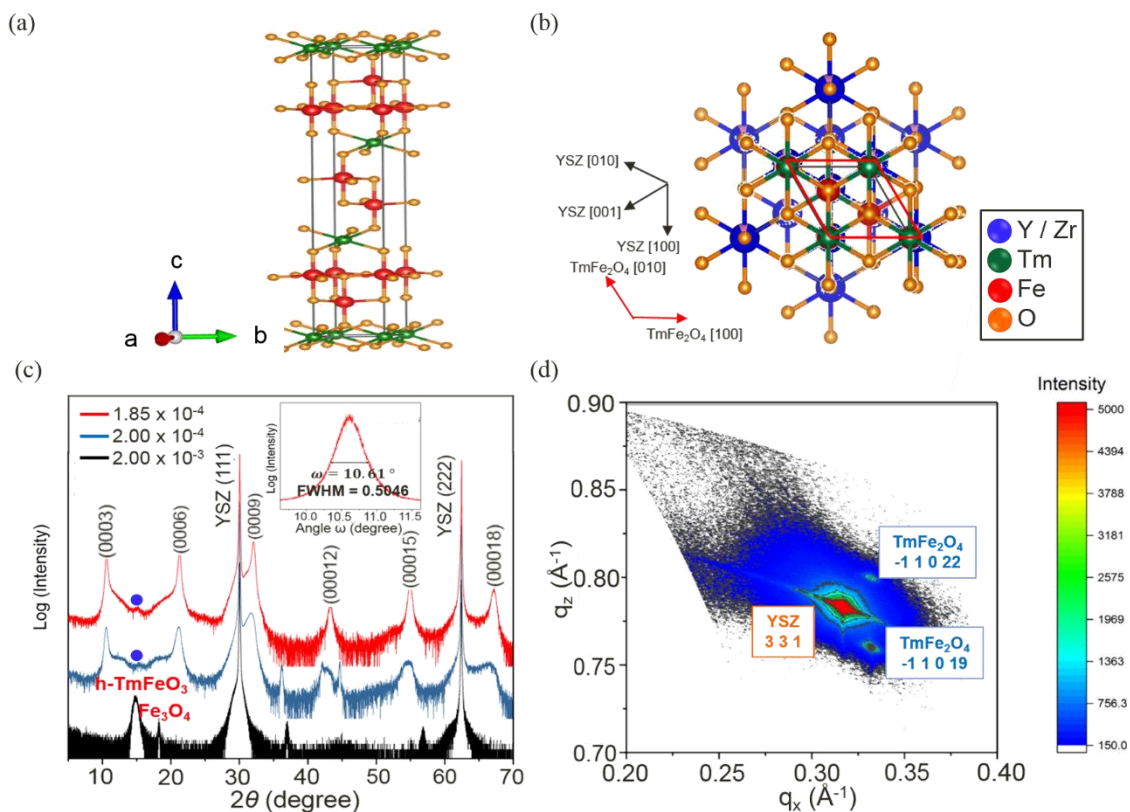
Figure 3.1. (a) Unit cell of $TmFe_2O_4$ in a hexagonal setting. (b) A possible growth mode

for $TmFe_2O_4$ thin film deposited on YSZ substrate. The [0001] direction of $TmFe_2O_4$ is

parallel to the [111] direction of YSZ. (c) Out-of-plane XRD patterns (θ-2θ scans) for

thin films deposited on YSZ (111) substrates under various oxygen partial pressures. The

filled circle (●) denotes the diffraction peaks assigned to hexagonal $TmFeO_3$ phase. The

inset shows a rocking curve measured for $TmFe_2O_4$ (0003) reflection. The full-width at

half maximum obtained from the rocking curve is 0.5046°. (d) Reciprocal space mapping

around (331) diffraction peak of YSZ substrate and for (110$\underline{19}$) and (110$\underline{22}$) diffraction

peaks of $TmFe_2O_4$ thin film.
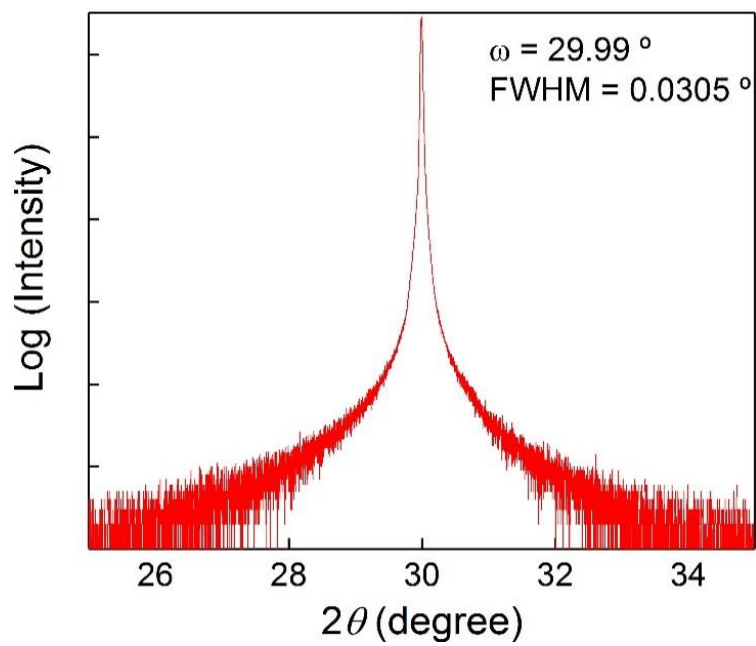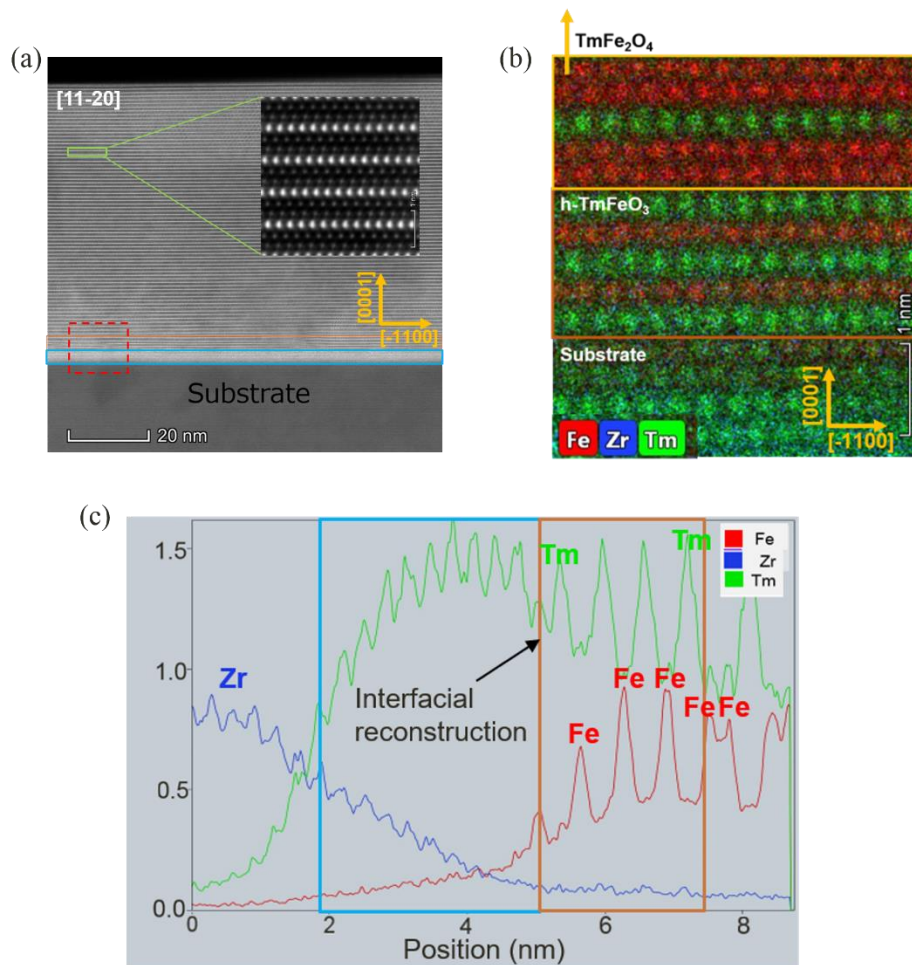
Figure 3.2. A rocking curve of YSZ (111) substrate used in the present study. The full-width at half maximum is 0.0305˚.
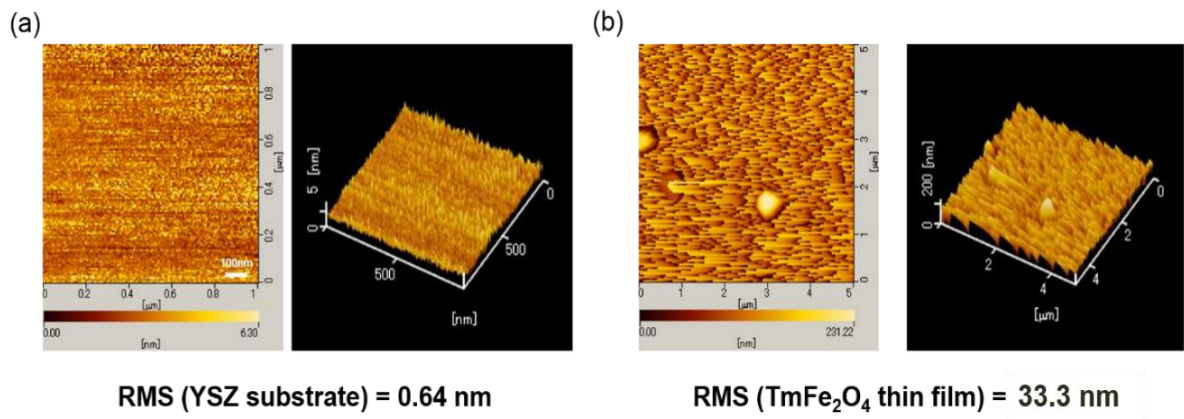
Figure 3.3. AFM images of YSZ substrate and TmFe₂O₄ thin film.

Figure 3.4. (a) High-angle annular dark field scanning TEM (HAADF-STEM) image of the $TmFe_2O_4$ thin film grown on the YSZ substrate. A well-ordered structure of $TmFe_2O_4$ phase is clearly observed, as illustrated in the inset. (b) STEM-electron dispersive X-ray (EDX) image, which shows that three layers, namely, Tm-rich layer, h-$TmFeO_3$-like phase with few atomic layers, and the $TmFe_2O_4$ phase are formed in this order, on the surface of the YSZ substrate. (c) A distribution of elements, estimated by EDX spectroscopy, across the interface from the YSZ substrate (the leftmost) to the $TmFe_2O_4$ thin film (the rightmost).
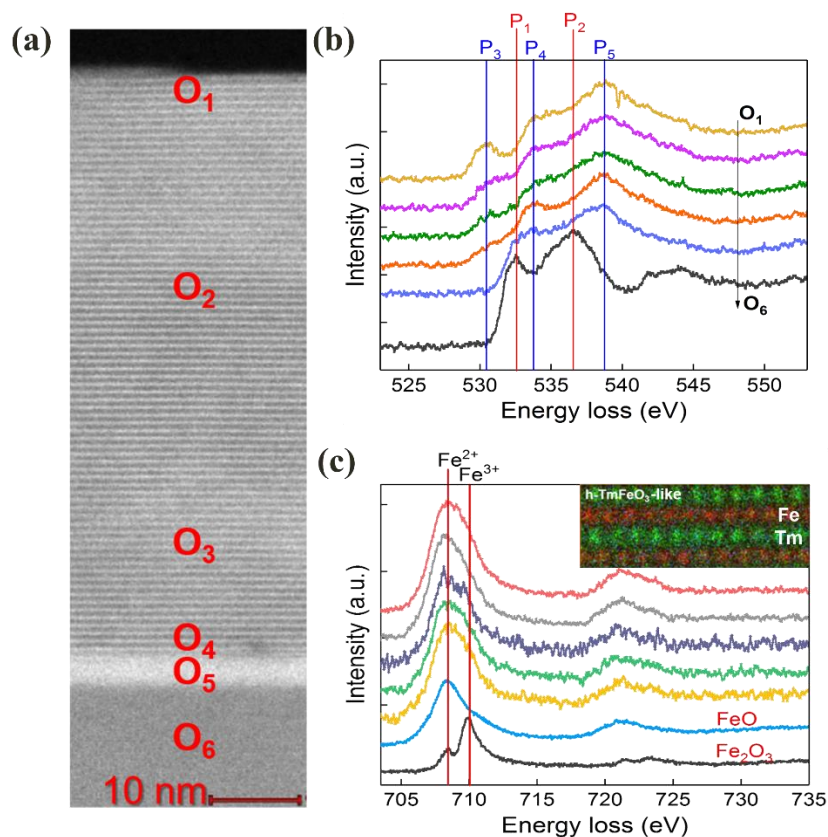
**Figure 3.5.** Structural analysis based on EELS for the $TmFe_2O_4$ thin film and the $TmFe_2O_4$/YSZ interface. (a) HAADF-STEM image, in which the bottom is the substrate and the upper part is the thin film. The white stripe represents the Tm^{3+}-rich region. The symbols O_1 to O_6 denote the positions for which EEL spectra of O K-edge were obtained (see Figure 3.3 (b)). (b) O K-edge EEL spectra for the positions from O_1 (surface) to O_6 (substrate). The peaks of P_1 and P_2 are attributed to the crystal field splitting of Zr 4d into e_g (P_1) and t_{2g} (P_2) orbitals. On the other hand, P_3 peak indicates the hybridization of the O 2p orbitals with the Fe 3d orbitals, and both P_4 and P_5 peaks are derived from the mixing between O 2p and Tm 5d orbitals. (c) Fe $L_{2,3}$-edge EEL spectra obtained from the several Fe ions of Fe monolayer at the interfacial *h*-$TmFeO_3$-like phase (inset). The reference spectra of Fe_2O_3 (hematite) and FeO (wüstite) are shown for comparison.

111
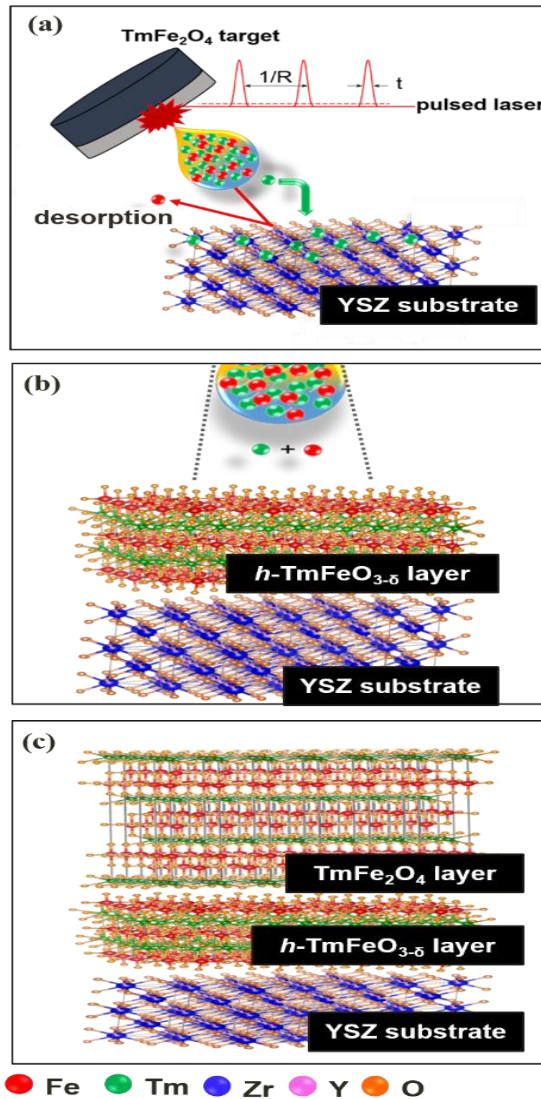
Figure 3.6. A possible growth mechanism of the present $TmFe_2O_4$ thin film on YSZ substrate. The red, green, blue, pink, and orange spheres refer to Fe, Tm, Zr, Y, and O atoms, respectively. (a) At the beginning step of deposition, Fe and Tm atoms are bombarded out from the target. In this process, Tm^{3+} ions might be diffused into the substrate by the interface reaction and Fe atoms may be detached from the substrate due to the low residence time of Fe atoms. (b) The h-$TmFeO_{3-\delta}$ interlayer is formed prior to $TmFe_2O_4$, and afterwards, $TmFe_2O_4$ phase stats to form. (c) A schematic model for a $TmFe_2O_4$/h-$TmFeO_{3-\delta}$/YSZ structure.
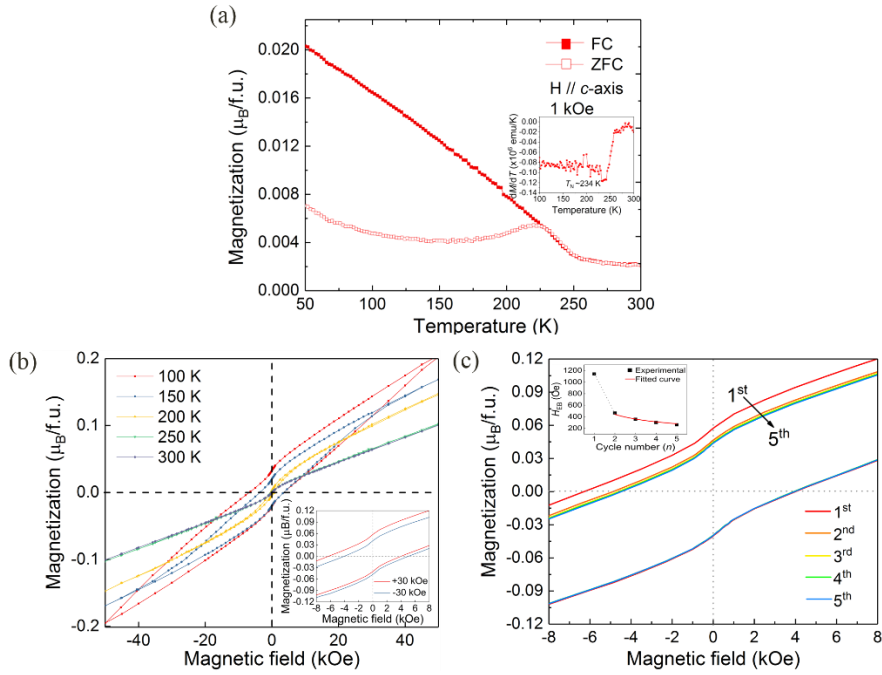
Figure 3.7. Magnetic properties of the $TmFe_2O_4$ thin film. (a) Temperature dependence of zero-field-cooled (ZFC) and field-cooled (FC) magnetizations measured by applying 1 kOe of dc magnetic field. The inset shows the first-order temperature derivative of magnetization, from which Néel temperature can be estimated to be ~234 K. (b) The magnetic field dependence of magnetizations (*M-H* curves) measured at various temperatures ($T = 100, 150, 200, 250$, and 300 K). The inset illustrates the central part of *M-H* loops measured at 100 K after ± 30 kOe FC process. (c) An enlarged view of the central region of the consecutive hysteresis loops after +30 kOe FC process, indicating the training effect of exchange bias at 100 K. The inset denotes H_{EB} as a function of the number of cycle (*n*). Here, $H_{EB} = |(H_1 + H_2)/2|$, and H_1 (H_2) represents the negative (positive) coercive field. The solid black rectangles indicate the experimental data and the solid red line shows the best fit of the empirical power law to the data for $n > 1$.
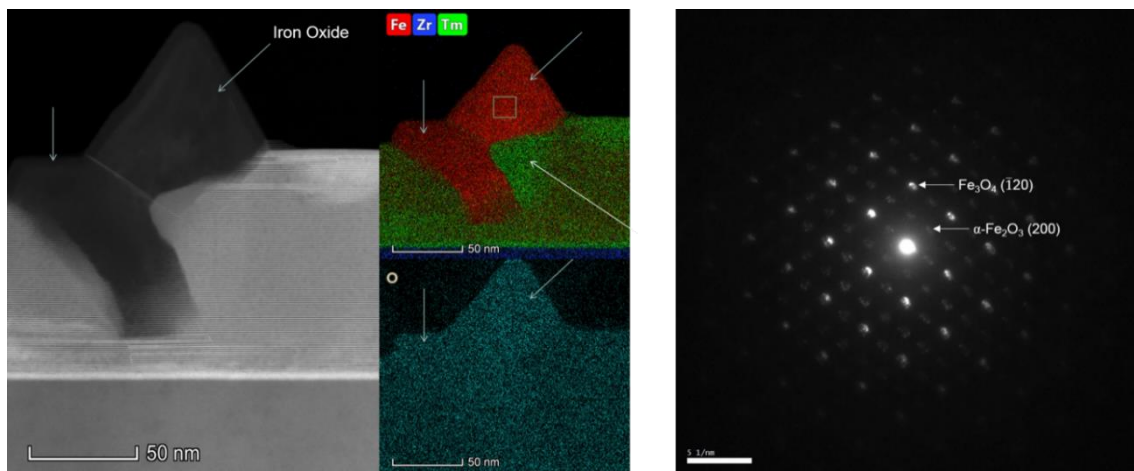
Figure 3.8. HAADF-STEM image, distribution of elements determined by EDX, and SAED pattern of impurity phases observed in a limited area of $TmFe_2O_4$ thin film. The SAED pattern was analyzed to identify the impurity phases, and they were found to be Fe_3O_4 and α-Fe_2O_3.
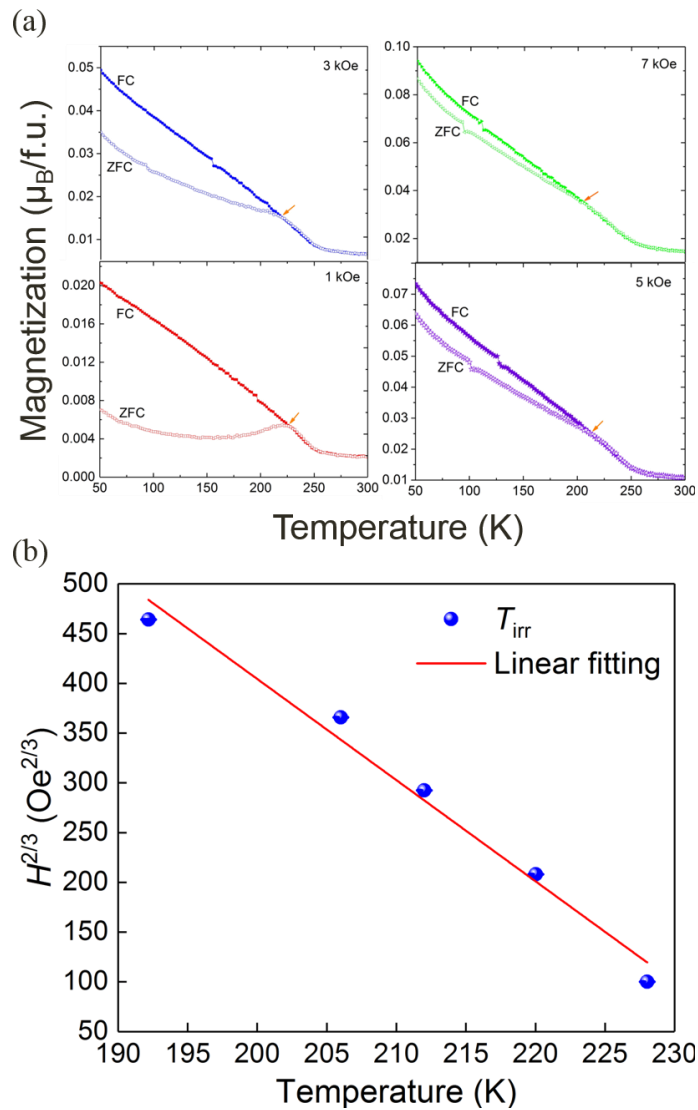
Figure 3.9. (a) Temperature dependence of ZFC and FC magnetizations measured at various dc magnetic fields (H = 1, 3, 7, and 10 kOe). The curves denoted by solid and open symbols show FC and ZFC data, respectively. The arrows indicate the irreversibility temperature, T_{irr}. (b) The relation between T_{irr} and $H^{2/3}$. A liner relation, corresponding to the AT line, is observed. The standard deviation of T_{irr}, lies in the range between 0.25 and 0.3 K.
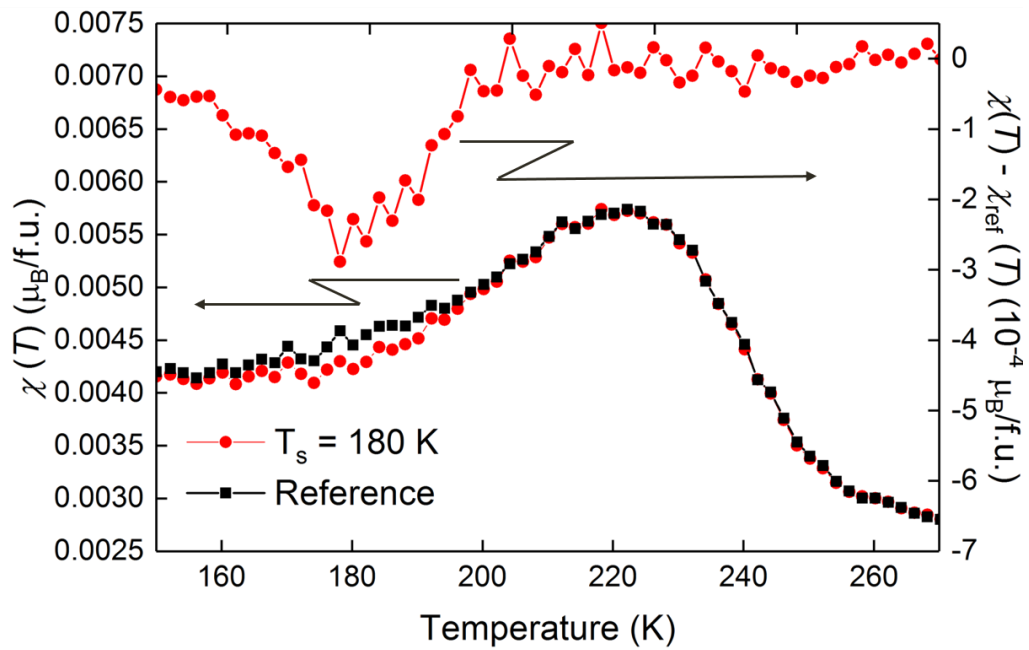
Figure 3.10. Temperature dependence of dc magnetization for TmFe$_2$O$_4$ thin film before and after aging at 180 K for 6 h. Difference between the magnetization values before and after aging is also shown at the upper part.

Chapter 4: Spin glass transition of single-crystalline TmFe$_2$O$_{4-\delta}$

4.1. Introduction

Spin glass is a prototype of random spin systems where magnetic moments are frozen in random orientations due to the magnetic frustration originating in different types of magnetic interactions or geometrically specified arrangement of magnetic moments with antiferromagnetic interactions.[1] Vigorous investigations have been carried out for spin glasses since the first observation of spin glass behavior in binary alloy systems of Au-Fe[2] and Cu-Mn.[3] Spin glass phase exhibits curious properties, in particular, those related to spin dynamics such as critical slowing down[4] and aging-memory effect[5] at around and below the spin glass transition temperature. Unusual magnetic properties relevant to the spin glass phase have been observed in a variety of compounds including oxides,[6-8] sulfides,[9, 10] and halides[11. 12] as well as alloys as exemplified above. In addition, one milestone in the research of spin glasses is its great contribution to the development of information technology, as theories of spin glasses have been successfully applied to neural network systems which possess some features similar to the associative memory process in brain.[13]

A series of compounds RFe$_2$O$_4$ (R = Sc, In, Y, and Dy to Lu),[14] which have attracted great attention because they are thought to be electronic dielectrics[15], are known to show spin frustration as well. The crystal structure of RFe$_2$O$_4$ in hexagonal setting is characterized by the alternative stacking of [FeO$_5$] double-layers sandwiched in between

[RO$_6$] single-layers along the c-axis and Fe^{2+} and Fe^{3+} ions are on a triangular lattice within the c-plane.[16] Such a two dimensional triangular lattice in which antiferromagnetic interactions work among the Fe^{2+} and Fe^{3+} ions inevitably leads to the geometrical frustration of spins. In this structure, iron double-layer that consists of equal number of Fe^{2+} and Fe^{3+} generates frustration of charge as well. Also, two- and three-dimensional ordered states of charge and spin emerge depending on the temperature, leading to a variety of physical properties such as magnetism, electrical conduction, and dielectricity.[15, 17-20] Among the RFe$_2$O$_4$ compounds, LuFe$_2$O$_4$ has been most extensively studied for its structure and physical properties. According to the previous reports on magnetism of LuFe$_2$O$_4$ bulk forms, both Fe^{2+} and Fe^{3+} ions take the high-spin configurations and behave as an Ising spin owing to the strong anisotropy along the c-axis.[21] The magnetic properties are also largely dependent on the stoichiometry of oxygen and/or iron. For instance, a long-range spin correlation develops along the c-axis in stoichiometric LuFe$_2$O$_4$ and a competition between ferrimagnetic and antiferromagnetic structures is observed at the magnetic phase transition temperature.[22, 23] On the other hand, for nonstoichiometric LuFe$_2$O$_4$, glassy behavior such as spin glass or cluster glass transition was observed due to a decrease of coherence length within the c-plane that was characterized by pancake-like spin clusters.[23-26] Wang et al.[24] performed detailed investigation on the spin glass behavior of LuFe$_2$O$_{4.07}$, that is the compound with excess oxygen. They revealed that the dependence of spin-freezing temperature on frequency of ac magnetic field is explainable in terms of the dynamic scaling law with the critical exponent and the microscopic flipping time of magnetic moments being 6.9 and 10^{-13} s,

118

respectively. They also found that $LuFe_2O_{4.07}$ exhibits non-equilibrium phenomena such as aging-memory and rejuvenation effect. On the basis of those observations they concluded that spin glass phase appears at low temperatures.

In addition to $LuFe_2O_4$, magnetic properties of $YbFe_2O_4$ and YFe_2O_4 have been rather widely studied.[17, 19, 27-30] Those compounds are also known to manifest magnetic behavior which largely depends on the oxygen nonstoichiometry. Inazumi et al.[28] examined temperature dependence of magnetization for $YFe_2O_{4-\delta}$ with δ being 0.00 to 0.095. According to their report, both zero-field-cooled (ZFC) and field-cooled (FC) magnetizations manifest a sharp peak at around 240 K for $\delta = 0.00$, suggesting that an antiferromagnetic transition seems to occur at this temperature,[29] whereas a broad peak is observed in temperature dependence of ZFC magnetization for $\delta \geq 0.055$. Furthermore, for the latter compositions, FC magnetization does not show such a broad peak but monotonically increases with a decrease in temperature. Williamson et al.[30] prepared single crystals of $YbFe_2O_4$ in atmosphere of varied molar ratios of CO_2 to CO gases and found that temperature variation of magnetization depends on the oxygen partial pressure used for the growth of the single-crystalline specimens; highly stoichiometric specimen exhibits a sharp magnetic transition while the transition observed for nonstoichiometric ones is rather broad. These phenomena are similar to those observed for $LuFe_2O_4$ and YFe_2O_4 with different amounts of oxygen deficiencies.

In comparison to $LuFe_2O_4$, $YbFe_2O_4$, and YFe_2O_4, whose magnetic structures and transitions were examined in detail, there exist only a few reports on magnetic properties of $R$$Fe_2O_4$ with other rare-earth elements. For instance, temperature-dependent

magnetization was first reported for single-crystalline $TmFe_2O_4$ very recently.[31] In the present study, I have explored in detail magnetic transitions and structures for single-crystalline $TmFe_2O_{4-\delta}$ with oxygen vacancies on the basis of static and dynamic measurements. I have performed experiments on temperature dependence of FC and ZFC magnetizations, effect of dc magnetic field on magnetic phase transition temperature, dependence of phase transition temperature on frequency of ac magnetic field, and aging-memory and rejuvenation effect. I have found that $TmFe_2O_{4-\delta}$ exhibits spin glass transition with the spin-freezing temperature $T_g = 186.2$ K.

4.2. Sample fabrication

$TmFe_2O_{4-\delta}$ single crystal was grown by using optical floating zone (FZ) melting method. Reagent-grade Tm_2O_3 (Nippon Yttrium Co., LTD., Japan, 99.9 %) and Fe_2O_3 (Kojundo Chemical Laboratory Co., Ltd., Japan, 99.99 %) powders were used as starting materials. Tm_2O_3 powder was heated at 900℃ for 12 h to remove adsorbed water and then mixed with Fe_2O_3 with the stoichiometric composition. The powders were mixed thoroughly and the mixture was compacted into a rod. Then, the rod-shaped specimen was sintered in air at 1200℃ for 12 h. The resultant sintered material was used as both feed and seed for the growth of single crystals. First, a rod of polycrystalline $TmFe_2O_{4-\delta}$ was prepared in an FZ melting furnace at a rather high moving rate of the rod (about 18.90 mm/h) under an atmosphere of N_2, H_2 and CO_2. I used a mixture of 95% N_2/5% H_2 gas and CO_2 gas, the molar ratio of which was 3 : 1. By using the polycrystalline rod thus obtained, single crystal was synthesized at a growth rate of about 1.70 mm/h under the

same atmospheric condition.

4.3. Characterization

X-ray diffraction (XRD) analysis with Cu Kα radiation was carried out to confirm that the resultant single-crystalline specimen was $TmFe_2O_{4-\delta}$ (Rigaku RINT2500). By using Laue camera (IPX IPX-LC) with white radiation from a tungsten tube, the lattice planes of the single-crystalline specimen were detected and the specimen was cut into pieces so that the surface of each specimen would be equivalent to the c-plane of crystal. Since the present single crystal might have oxygen vacancies because of the reducing atmosphere and high temperature during the crystal growth process, oxygen content was evaluated for the as-grown single-crystalline specimen by using thermogravimetry and differential thermal analysis (Rigaku TG-DTA 8120). Magnetic properties were examined using a superconducting quantum interference device magnetometer (Quantum Design MPMS-SQUID). I carried out measurements on temperature dependence of FC and ZFC magnetizations at varied dc magnetic fields, frequency and temperature dependence of ac susceptibility, and effects of aging with and without external magnetic fields on susceptibility to clarify the static and dynamic properties of spins. Details of the conditions for the measurements are described in the following.

4.4. Results and discussion

My preliminary experiment reveals that the single-crystalline $TmFe_2O_{4-\delta}$ is easily decomposed into other phases such as garnet-type $Tm_3Fe_5O_{12}$, Tm_2O_3, orthorhombic

TmFeO$_3$, and iron oxides at high temperatures when the compound is heat-treated in air. In order to avoid the decomposition, TG-DTA measurement was conducted up to 250℃, at which the DTA curve manifested a drastic change signifying that the decomposition reaction begins. Figure 4.1 shows TG-DTA curves for the as-grown TmFe$_2$O$_{4-\delta}$, indicating that the weight of the specimen slightly increases by about 0.36 % upon heating up to 250℃. This suggests that oxygen vacancies likely present in the as-grown specimen are filled by oxide ions supplied from the air. Supposing the resultant specimen after heating up to 250℃ has the stoichiometric composition, the amount of oxygen vacancies, i.e., δ in TmFe$_2$O$_{4-\delta}$ is estimated to be about 0.07. Here, it should be noted that the amount of oxygen vacancies is dependent on the part of a rod of single-crystalline TmFe$_2$O$_{4-\delta}$, as de Groot et al. reported that the oxygen contents in LuFe$_2$O$_4$ single crystals were not identical to each other even if the single-crystalline specimens stemmed from the same rod.[22] Although the value of δ estimated for the present TmFe$_2$O$_{4-\delta}$ is just an approximate one, the weight gain in the TG curve in figure 4.1 clearly ascertains that the present single-crystalline specimen, for which measurements of magnetic properties have been performed, contains oxygen vacancies.

Figure 4.2(a) depicts the temperature dependence of magnetizations (*M-T* curve, where *M* is the magnetization and *T* is the temperature.) measured under 1 kOe of dc magnetic field applied parallel and perpendicular to the *c*-axis for the as-grown TmFe$_2$O$_{4-\delta}$ single crystal. The magnetization parallel to the *c*-axis is significantly higher than that perpendicular to the *c*-axis, indicating that the easy axis of magnetization is along the *c*-axis, as suggested for other *R*Fe$_2$O$_4$ single crystals such as LuFe$_2$O$_4$ and YbFe$_2$O$_4$. Also,

in the previous reports on magnetic properties of $LuFe_2O_4$, $YbFe_2O_4$, and YFe_2O_4, the M-T curves were utilized as a criteria for determination of degree of nonstoichiometry.[21, 22] Namely, as mentioned above, single crystals with nonstoichiometric oxygen contents exhibit a magnetic transition characterized by a broad peak in the temperature dependence of ZFC magnetization.[32-35] In addition to the above-mentioned TG-DTA result, the broad peak observed in the ZFC process in figure 4.2(a) indicates that the present single-crystalline specimen has oxygen vacancies. The temperature variations of ZFC and FC magnetizations in figure 4.2(a) are very similar to those observed for polycrystalline $TmFe_2O_4$[36] and for single-crystalline $TmFe_2O_{4-\delta}$ reported previously.[31] Namely, an abrupt increase in FC magnetization observed around 240 K suggests that long-range magnetic ordering begins to develop and the magnetic phase transition occurs from paramagnetic to ferrimagnetic states at this temperature. The Néel temperature (T_N), determined by the first-order temperature derivative of magnetization (dM/dT), is about 208 K (the left inset of figure 4.2(a)). The antiferromagnetic interaction between iron ions might be ascertained by the negative Weiss temperature that is about -6.2 K as estimated by the following Curie-Weiss equation for the paramagnetic states (the right inset of figure 4.2(a)):

$$\frac{1}{\chi} = \frac{3k_B(T - \theta)}{NM_B^2\mu_B^2} \tag{1.}$$

The Weiss temperatures is similar with the value previously reported for single-crystalline $YbFe_2O_4$.[37,38]

Moreover, RFe_2O_4 exhibits rather complicated magnetic structure and phase transition

relevant to the spin dynamics; spin glass or cluster glass behavior was observed for LuFe$_2$O$_4$[23-26] and YbFe$_2$O$_4$.[27, 39] In the *M-T* curves shown in figure 4.2(a), the large difference in magnetization is found between FC and ZFC processes at low temperatures, suggesting that there exist glassy phase transition around 186.2 K at which the maximum of ZFC magnetization is observed. First, I measured *M-T* curves under various dc magnetic fields to verify that the single-crystalline TmFe$_2$O$_{4-\delta}$ undergoes spin glass or cluster glass transition before analyzing spin dynamics in more detail. The results are illustrated in figure 4.2(b), which clearly indicates that the irreversible transition temperature, T_{irr}, decreases with increasing the dc magnetic field, *H*. Here, T_{irr} is defined as a temperature at which the ZFC and FC magnetizations diverge from each other as the temperature is decreased. Furthermore, the relation between T_{irr} and *H* can be well interpreted in terms of the de Almeida-Thouless (AT) line. Qualitatively speaking, the phenomenon reflects the fact that the magnetic frustration is suppressed by large dc magnetic fields, indicating that the present TmFe$_2$O$_{4-\delta}$ single crystal manifests spin glass-like transition.

In order to elucidate the spin dynamics for the present TmFe$_2$O$_{4-\delta}$ single crystal, the temperature dependence of real (χ') and imaginary (χ'') parts of ac magnetic susceptibility was measured in the ZFC process. The amplitude of the ac field was constantly kept at 3 Oe and the ac frequency was varied from 5 to 500 Hz. For both real and imaginary parts, the spin-freezing temperature (T_f (*f*)) shifts to higher temperatures with increasing the frequency of ac field. In order to obtain more detailed information about the glassy state of the present TmFe$_2$O$_{4-\delta}$ single crystal, I analyze the experimental data by assuming that

the frequency variation of $T_f(f)$ is expressed in terms of the dynamic scaling law described by[40]

$$\tau = \tau_0 \left(\frac{T_f(f) - T_g}{T_g}\right)^{-zv} , \tag{2}$$

where τ is the characteristic relaxation time that is equal to $1/f$, τ_0 is the microscopic relaxation time which indicates a spin flip time of an individual magnetic moment or a magnetic cluster, z is the dynamical exponent, and v is the critical exponent for the magnetic correlation length. In the present case, the best fit of equation (2) to the experimental data, as shown in the inset of figure 4.3(a), yields that $zv = 8.68(8)$, $T_g = 186.2$ K, and $\tau_0 = \sim 10^{-13.66(5)}$ s. Considering the fact that zv values previously reported for spin glasses including alloys, sulfides, and oxides lie in a range of 4 to 13,[41] the present value $zv = 8.68(8)$ suggests that the magnetic structure at low temperatures can be categorized into a spin glass state. In addition to the zv value, the value of τ_0, i.e., $10^{-13.66(5)}$ s is also reasonable for the typical spin glasses.[42, 43] Therefore, as the temperature is decreased, $TmFe_2O_{4-\delta}$ first undergoes the transition from paramagnetic to ferrimagnetic states followed by additional transition from ferrimagnetic to spin glass states.

I have further performed the measurement of aging-memory effect without applied magnetic field, the process of which was proposed by Mathieu et al.[6] to confirm that the magnetically ordered phase of $TmFe_2O_{4-\delta}$ is spin glass at low temperatures. In the measurement process, the specimen is cooled under zero magnetic fields from high temperature to the lowest temperature of measurement with or without an intermittent stop at a specific stopping temperature (T_s) that is below the spin glass transition

temperature. Afterward, the magnetic susceptibility, $\chi(T)$, is recorded during the subsequent heating process in an applied magnetic field. Since the aging-memory effect only occurs in spin glasses, strongly interacting nanoparticle systems, and cluster glasses, observation of the effect can be a standard evidence for cooperative spin dynamics characteristic of spin glasses and related systems. Here, the single-crystalline $TmFe_2O_{4-\delta}$ was cooled from 220 K, which was higher than T_N, to $T_s = 150$ and 160 K at a rate of 2 K/min and was kept for 6 h at T_s. The reference data were acquired by conducting the ZFC process without any intermittent stops. Figure 4.4 illustrates the temperature dependence of dc magnetic susceptibility obtained with and without the intermittent stops. Also, the difference in susceptibility between with and without the stop is shown in figure 4.4. As the temperature increases from the lowest temperature of measurement, the $\chi(T)$ curve deviates downward from the $\chi_{ref}(T)$ curve as the temperature approaches T_s, and $\chi(T)$ curves gradually merges to $\chi_{ref}(T)$ beyond T_s. The effect of aging is characterized by a dip formed at T_s. A clear observation of the memory effect along with the above-mentioned critical slowing down at the phase transition temperature strongly suggests that the magnetic phase of the present $TmFe_2O_{4-\delta}$ single crystal is spin glass below 186.2 K.

An aging effect under a magnetic field is also explored for the present $TmFe_2O_{4-\delta}$ single crystal. The experimental protocol was proposed by Bernardi et al.[44] and the process in the present case is as follows. The specimen was zero-field-cooled from 220 K, which was above T_g, to 120 K at a rate of 2 K/min. Afterward, a magnetic field of 100 Oe was applied to the specimen and the susceptibility was measured during the heating process

at a rate of 2 K/min. For the aging process, at T_s, which was 150 and 160 K, the specimen was kept for 6 h under 100 Oe, and then the susceptibility was further measured while the temperature was increased up to 220 K at the same heating rate. On the other hand, the reference was obtained by measuring susceptibility in ZFC process without any halts at certain temperatures. The results are depicted in figure 4.5. As indicated in this figure 4.5, the susceptibility discontinuously increases just after aging for 6 h at T_s. As the temperature is increased from T_s, the susceptibility decreases and eventually merges with the reference curve at a temperature above T_s. The decrease of the susceptibility just above T_s is thought to reflect rejuvenation behavior that is characteristic of nonequilibrium phenomenon in spin glass phase and attributed to a chaotic nature of spin configurations which depend on temperature. The behavior shown in figure 4.5 is similar to that observed for three-dimensional (3D) Ising spin glass $Fe_{0.5}Mn_{0.5}TiO_3$, for which the ZFC susceptibility can be explained by means of droplet theory of spin glass.[44]

Based on the above-mentioned experimental results, it seems that the present single-crystalline $TmFe_2O_{4-\delta}$ exhibits reentrant spin glass-like transition; magnetic moments of Fe ions order ferrimagnetically at T_N ~208 K and then undergo a transition to spin glass phase at T_g ~186.2 K as the temperature is decreased, although I cannot rule out a possibility that ferrimagnetic and spin glass phases coexist at low temperatures. Nonetheless, it is reasonable to consider that the disordered spin state comes from the geometrical spin frustration due to Fe^{3+} and Fe^{2+} ions with antiferromagnetic interactions in a two-dimensional triangular lattice. The oxygen vacancies lead to a situation that Fe^{2+} ions outnumber Fe^{3+} ions, increasing the degree of frustration. Measurement of nonlinear

magnetic susceptibilities around T_g would give rise to a complementary and strong evidence for the spin glass transition[45, 46] although it was not conducted in the present study. It is interesting to compare the glassy state among $LuFe_2O_4$, $YbFe_2O_4$, and $TmFe_2O_4$ with stoichiometric and nonstoichiometric compositions. The relaxation time, τ_0, derived from the dynamic scaling law shown in Eq. (2) is summarized in table 4.1 for those compounds.[24-27, 39] In general, the origin of two types of glassy states, spin glass and cluster glass, is similar to each other, but the relaxation time for cluster glass is much larger than for spin glass because of the difference in the entity that is involved in the relaxation process.[47] It is an individual spin for the spin glass, whereas a magnetic cluster changes the direction of its magnetization with time in the case of the cluster glass. Wang et al.[24] measured temperature and frequency dependence of ac susceptibility for $LuFe_2O_{4+\delta}$ with excess oxygen and concluded that the compound exhibits spin glass transition based on the analysis of critical slowing down. In contrast, Phan et al.[25, 26] performed similar measurements and analyses for $LuFe_2O_4$ single crystal with stoichiometric composition and clarified that the value of τ_0 is 9.18×10^{-8} s, suggesting that the compound undergoes cluster glass transition rather than spin glass transition. They also pointed out that their single-crystalline specimen manifests additional first-order magnetic transition around 170 K, which was not observed for the specimen reported by Wang et al. On the contrary, de Groot et al.[22] reported that stoichiometric $LuFe_2O_4$ single crystal does not exhibit spin glass nor cluster glass transition but clear antiferromagnetic transition at 240 K when the external magnetic field is low enough. The magnetic phase diagram for $LuFe_2O_4$ they proposed includes a region assigned to

neither spin glass nor cluster glass phase in a temperature range from 180 to 260 K at least. On the other hand, Kobayashi et al.[27] reported that the value of τ_0 for stoichiometric $YbFe_2O_4$ nanoparticle is $10^{-14\pm1}$ s, close to the typical value of spin glasses. Sun et al.[39] carried out the ac susceptibility measurements at varied temperature and frequency for polycrystalline $YbFe_2O_4$ and analyzed the resultant data in terms of the Arrhenius relation:

$$f = f_0\exp(-E_a/k_BT), \tag{3}$$

where f is the frequency, T is the temperature, k_B is the Boltzmann constant, and E_a is the activation energy for magnetic relaxation. The pre-exponential factor, f_0, was estimated to be 10^{12} Hz. Although this value might suggest that the polycrystalline $YbFe_2O_4$ shows spin glass transition, they concluded that magnetic clusters are frozen below 80 K on the basis of the fact that frequency and temperature dependence of dielectric constant and loss is relaxor-like and that polar clusters responsible for the behavior of relaxor exhibit a collective freezing at magnetic freezing temperature, i.e., 80 K. In other words, the polar cluster plays a role of a magnetic cluster as well. Also, it should be noted that the nonstoichiometry was not discussed for the polycrystalline $YbFe_2O_4$. Thus, the magnetic structure and transition are rather complicated and their relation to the nonstoichiometry is not clear at this moment. Further investigation is necessary to disclose how the oxygen-related point defects affect the magnetic properties, in particular, the glassy behavior.

4.5. Conclusion

I revealed that $TmFe_2O_{4-\delta}$ single crystal with oxygen vacancies displays reentrant spin glass-like behavior. The spin glass transition was confirmed by the experimental results and analyses; $TmFe_2O_{4-\delta}$ exhibits the aging-memory and rejuvenation effect, and the variation of spin-freezing temperature with the frequency of ac magnetic field is explainable in terms of the dynamic scaling law with critical exponent the value of which is typical of spin glasses. The disordered spin structure of the present single crystal is thought to originate in the strengthened geometrical frustration within the triangular lattice through unequal number of Fe^{2+} and Fe^{3+} ions caused by oxygen nonstoichiometry.

References in chapter 4

1. T. Komori, H. Yoshino and H. Takayama, *J. Phys. Soc. Jpn.* 2000, **69**, 215.

2. V. Cannella and J. A. Mydosh, *Phys. Rev. B*, 1972, **6**, 4220.

3. S. Nagata, P. H. Keesom and H. R. Harrison, *Phys. Rev. B*, 1979, **19**, 1633.

4. C. A. M. Mulder, A. J. Van Duyneveldt and J. A. Mydosh, *Phys. Rev. B*, 1981, **23**, 1384.

5. R. Mathieu, P. Jönsson, D. N. H. Nam and P. Nordblad, *Phys. Rev. B*, 2001, **63**, 092401.

6. S. Reich, Y. Tsabba and G. Cao, *J. Magn. Magn. Mater.,* 1999, **202**, 119.

7. S. K. Upadhyay, P. L. Paulose, K. K. Iyer and E. V. Sampathkumaran, *Phys. Chem. Chem. Phys.*, 2016, **18**, 23348.

8. J. E. Greedan, M. Sato, X. Yan and F. S. Razavi, *Solid State Commun.*, 1986, **59**, 895.

9. H. Lei, M. Abeykoon, E. S. Bozin and C. Petrovic, *Phys. Rev. B*, 2011, **83**, 180503.

10. H. Maletta and W. Felsch, *Phys. Rev. B*, 1979, **20**, 1245.

11. P. –Z. Wong, S. V. Molnar, T. T. M. Palstra, J. A. Mydosh, H. Yoshizawa, S. M. Shapiro and A. Ito, *Phys. Rev. Lett.*, 1985, **55**, 2043.

12. F. C. Montenegro, A. R. King, V. Jaccarino, S. J. Han and D. P. Belanger, *Phys. Rev. B*, 1991, **44**, 2155.

13. J. J. Hopfield, *Proc. Natl. Acad. Sci. U. S. A.*, 1982, **79**, 2554.

14. N. Kimizuka, A. Takenaka, Y. Sasada and T. Katsura, *Solid State Commun*, 1974, **15**, 1321.

15. N. Ikeda, H. Ohsumi, K. Ohwada, K. Ishii, T. Inami, K. Kakurai, Y. Murakami, K. Yoshii, S. Mori and Y. Horibe, *Nature*, 2005, **436**, 1136.

16. T. Mueller, J. de Groot, J. Strempfer and M. Angst, *J. Cryst. Growth*, 2015, **428**, 40.

17. T. Sugihara, K. Siratori, I. Shindo and T. Katsura, *J. Phys. Soc. Jpn.*, 1978, **45**, 1191.

18. M. Tanaka, K. Siratori and N. Kimizuka, *J. Phys. Soc. Jpn.*, 1984, **53**, 760.

19. M. Kishi, S. Miura, Y. Nakagawa, N. Kimizuka, I. Shindo and K. Siratori, *J. Phys. Soc. Jpn.*, 1982, **51**, 2801.

20. S. Lafuerza, J. García, G. Subías, J. Blasco, K. Conder and E. Pomjakushina, *Phys. Rev. B*, 2013, **88**, 085130.

21. W. Wu, V. Kiryukhin, H. –J. Noh, K. –T. Ko, J. –H. Park, I. W. Ratcliff, P. A. Sharma, N. Harrison, Y. J. Choi and Y. Horibe, *Phys. Rev. Lett.*, 2008, **101**, 137203.

22. J. de Groot, K. Marty, M. D. Lumsden, A. D. Christianson, S. E. Nagler, S. Adiga, W. J. H. Borghols, K. Schmalzl, Z. Yamani and S. R. Bland, *Phys. Rev. Lett.*, 2012, **108**, 037206.

23. A. D. Christianson, M. D. Lumsden, M. Angst, Z. Yamani, W. Tian, R. Jin, E. A. Payzant, S. E. Nagler, B. C. Sales and D. Mandrus, *Phys. Rev. Lett.*, 2008, **100**, 107601.

24. F. Wang, J. Kim, Y. –J. Kim and G. D. Gu, *Phys. Rev. B*, 2009, **80**, 024419.

25. M. H. Phan, N. A. Frey, H. Srikanth, M. Angst, B. C. Sales and D. Mandrus, *J. Appl. Phys.*, 2009, **105**, 07E308.

26. M. H. Phan, N. A. Frey, M. Angst, J. de Groot, B. C. Sales, D. G. Mandrus and H. Srikanth, *Solid State Commun.*, 2010, **150**, 341.

27. H. Kobayashi, K. Fujiwara, N. Kobayashi, T. Ogawa, M. Sakai, M. Tsujimoto, O. Seri, S. Mori and N. Ikeda, *J. Phys. Chem. Solids*, 2017, **103**, 103.

28. M. Inazumi, Y. Nakagawa, M. Tanaka, N. Kimizuka and K. Siratori, *J. Phys. Soc. Jpn.*, 1981, **50**, 438.

29. Y. Nakagawa, M. Inazumi, N. Kimizuka and K, Siratori, *J. Phys. Soc. Jpn.*, 1979, **47**, 1369.

30. H. Williamson, T. Mueller, M. Angst and G. Balakrishnan, *J. Cryst. Growth*, 2017, **475**, 44.

31. S. Konishi, K. Oka, H. Eisaki, K. Tanaka and T. Arima, *Cryst. Growth Des.*, 2019, **19 (10)**, 5498-5504.

32. M. Angst, *Phys. status solidi (RRL)–Rapid Research Letters*, 2013, **7**, 383.

33. F. Wang, J. Kim, G. D. Gu, Y. Lee, S. Bae and Y. –J. Kim, *J. Appl. Phys.*, 2013, **113**, 063909.

34. J. Iida, Y. Nakagawa and N. Kimizuka, *J. Phys. Soc. Jpn.*, 1986, **55**, 1434.

35. J. Iida, M. Tanaka, Y. Nakagawa, S. Funahashi, N. Kimizuka and S. Takekawa, *J. Phys. Soc. Jpn.*, 1993, **62**, 1723.

36. K. Yoshii, N. Ikeda and A. Nakamura, *Physica B*, 2006, **378**, 585.

37. M. Kishi, S. Miura, Y. Nakagawa, N. Kimizuka, I. Shindo and K. Siratori, *J. Phys. Soc. Jpn.*, 1982, **51**, 2801.

38. K. Yoshii, M. Mizumaki, K. Matsumoto, S. Mori, N. Endo, H. Saitoh, D. Matsumura, T. Kambe and N. Ikeda, *J. Phys.: Conf. Ser.*, 2013, **428**, 012032.

39. Y. Sun, Y. Liu, F. Ye, S. Chi, Y. Ren, T. Zou, F. Wang and F. Yan, *J. Appl. Phys.*, 2012, **111**, 07D902.

40. A. T. Ogielski, *Phys. Rev. B*, 1985, **32**, 7384.

41. T. D. Thanh, D. H. Manh, T. L. Phan, P. T. Phong, L. T. Hung, N. X. Phuc and S. C. Yu, *J. Appl. Phys.*, 2014, **115**, 17B504.

42. K. Gunnarsson, P. Svedlindh, P. Nordblad, L. Lundgren, H. Aruga and A. Ito, *Phys. Rev. Lett.*, 1988, **61**, 754.

43. P. Nordblad, *J. Phys.: Condens. Matter*, 2004, **16**, S715.

44. L. W. Bernardi, H. Yoshino, K. Hukushima, H. Takayama, A. Tobo and A. Ito, *Phys. Rev. Lett.*, 2001, **86**, 720.

45. L. P. Lévy and A. T. Ogielski, *Phys. Rev. Lett.*, 1986, **57**, 3288-3291.

46. L. P. Lévy, *Phys. Rev. B*, 1988, **38**, 4963-4973.

47. Y. M. Liang, Z. J. Wang, Y. Bai, Y. J. Wu, X. K. Ning, X. F. Xiao, X. G. Zhao, W. Liu and Z. D. Zhang, *J. Mater. Chem. C*, 2019, **7**, 2376.

Table 4.1. A comparison of relaxation time and type of glassy state among with previously reported in $R\text{Fe}_2\text{O}_4$ (R = Lu, Yb, and Tm) compounds with stoichiometric and nonstoichiometric compositions. The nonstoichiometric compounds include excess or deficient oxygen.

| Compound	Relaxation time, τ_0 (s)	Type of glassy state	Ref.
Single-crystalline $\text{LuFe}_2\text{O}_{4+\delta}$	$10^{-13.0\pm2.0}$	Spin glass	24
Single-crystalline LuFe_2O_4	9.18×10^{-8}	Cluster glass	25, 26
YbFe_2O_4 nanoparticle	$10^{-14\pm1}$	Spin glass	27
Polycrystalline YbFe_2O_4	a)	Cluster glass	39
Single-crystalline $\text{TmFe}_2\text{O}_{4-\delta}$	$10^{-13.66(5)}$	Spin glass	This work

a) The temperature and frequency dependence of ac susceptibility was analyzed in terms of the Arrhenius relation: $f = f_0\exp(-E_\text{a}/k_\text{B}T)$, with $f_0 = 10^{12}$ Hz.
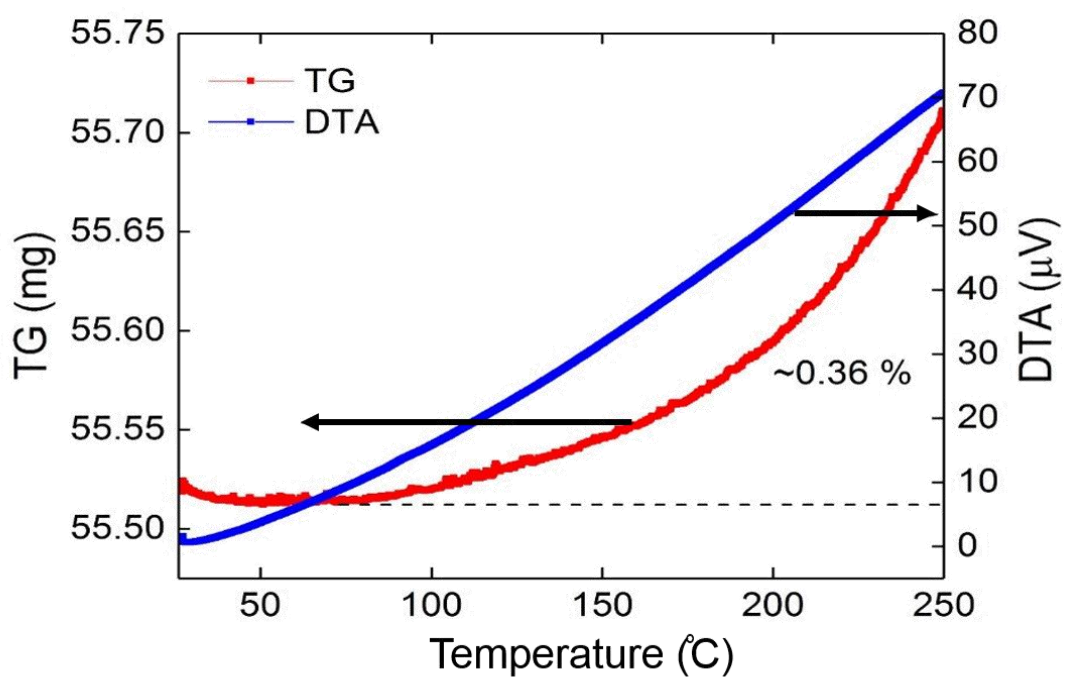
Figure 4.1. Thermogravimetric-differential thermal analysis (TG-DTA) curves for as-grown $TmFe_2O_{4-\delta}$ single crystal. Data were recorded in air at a heating rate of 10 K/min.
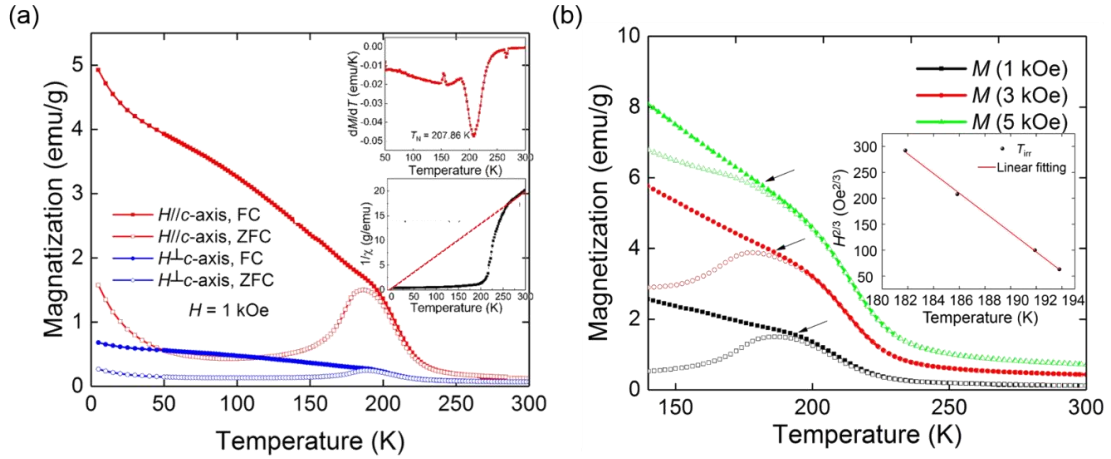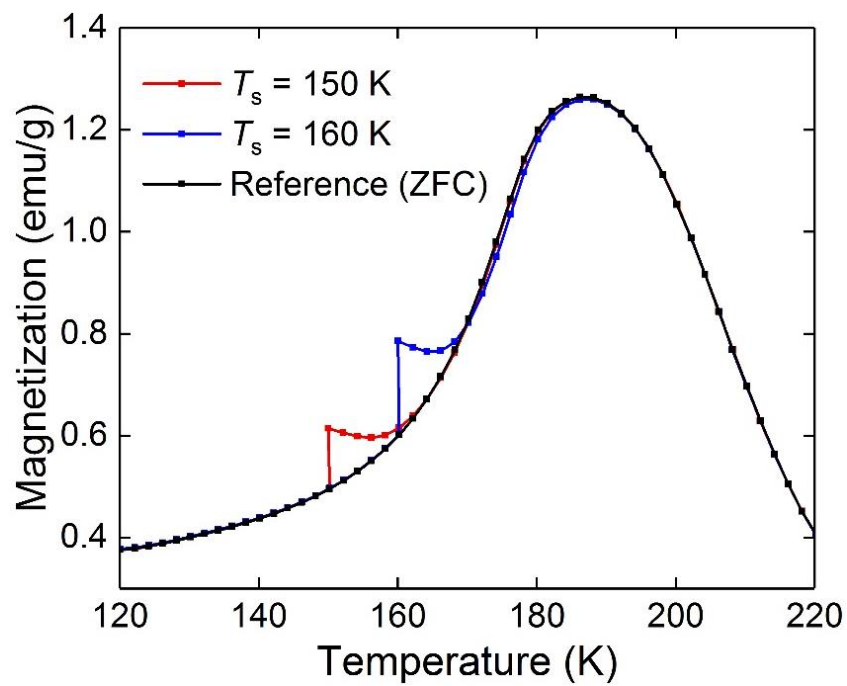
Figure 4.2. (a) Temperature dependence of zero-field-cooled (ZFC) and field-cooled (FC) magnetizations measured under 1 kOe of dc magnetic field parallel and perpendicular to the c-axis. The left inset shows the first-order temperature derivative of FC magnetization, from which the Néel temperature is estimated to be about 208 K. The right inset illustrates temperature dependence of inverse magnetic susceptibility. The data at high temperatures were analyzed with Curie-Weiss law as indicated by the red line. (b) Temperature dependence of ZFC and FC magnetizations measured at varied dc magnetic fields (H = 1, 3, and 5 kOe). Curves denoted by filled and open spheres indicate FC and ZFC magnetizations, respectively. The arrows denote the irreversible transition temperature, T_{irr}. The inset shows the relation between T_{irr} and $H^{2/3}$, indicating that the experimental data can be interpreted in terms of de Almeida-Thouless line (AT-line).
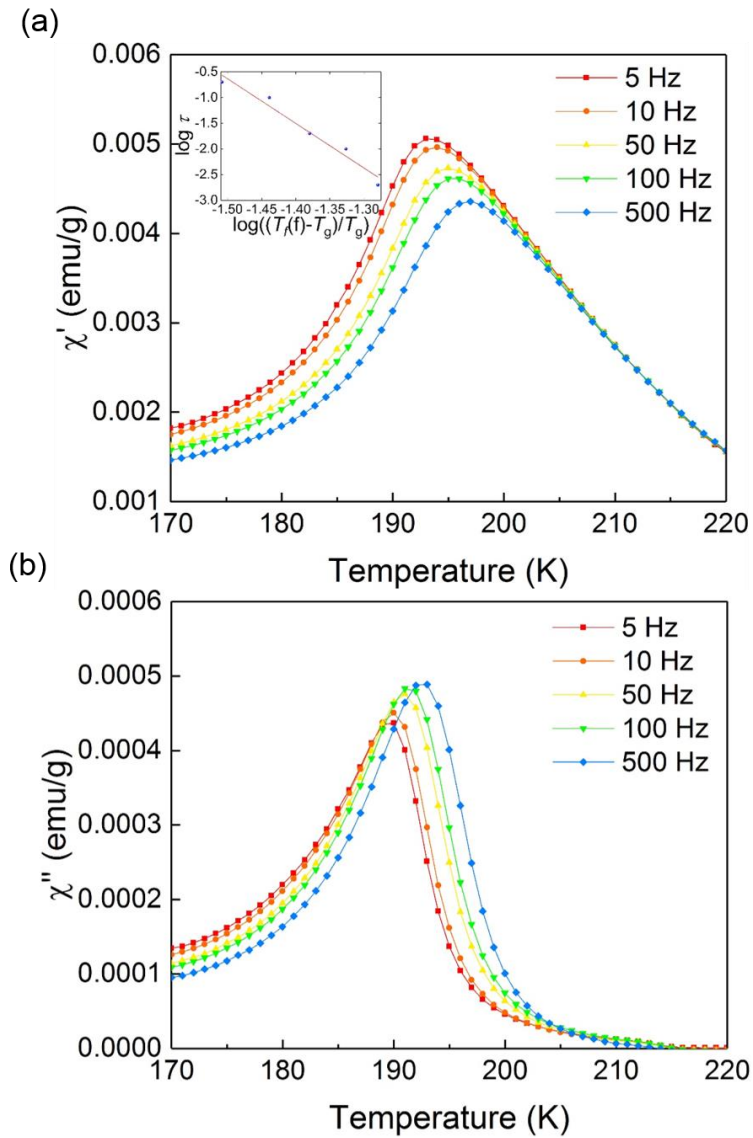
Figure 4.3. Temperature dependence of ac magnetic susceptibility for the $TmFe_2O_{4-\delta}$ single crystal. The frequency f is 5, 10, 50, 100, and 500 Hz and the amplitude of ac magnetic field is $h_{ac} = 3$ Oe. The real and imaginary parts of the susceptibility are shown in (a) and (b), respectively. The inset of (a) indicates the relationship between the relaxation time τ and the spin-freezing temperature $T_f(f)$. The line was drawn on the basis of the scaling low (plots of $\log\left|\frac{T_f(f)-T_g}{T_g}\right|$ versus $\log \tau$, where T_g is the critical temperature).
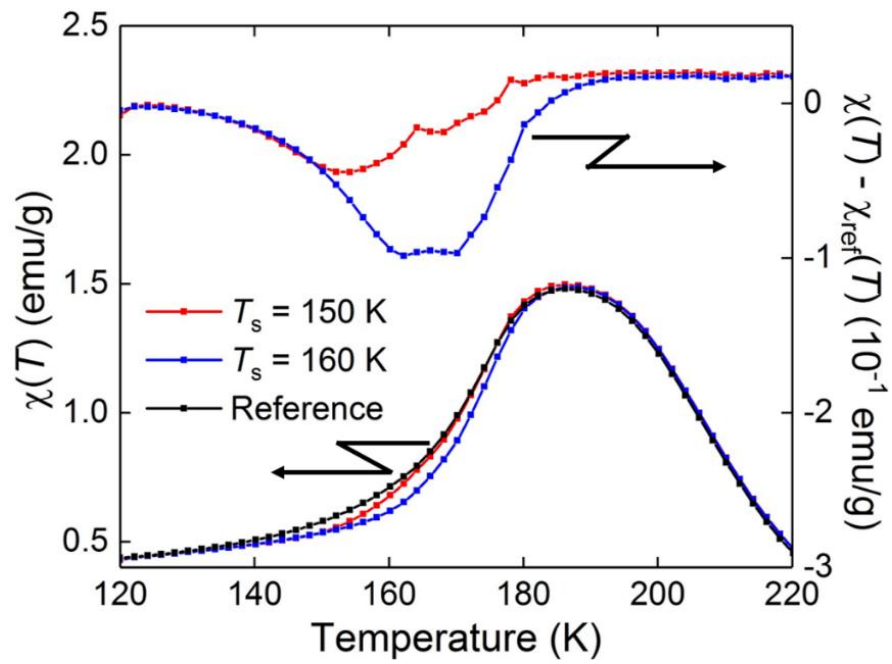
Figure 4.4. Temperature dependence of dc magnetic susceptibilities measured on heating after ZFC process with and without an intermittent stop, i.e., aging at T_s (150 and 160 K). $\chi(T)$ and $\chi_{ref}(T)$ denote the magnetic susceptibilities with and without aging, respectively. The difference between $\chi(T)$ and $\chi_{ref}(T)$ is shown as well.

Figure 4.5. Temperature dependence of dc magnetic susceptibilities ($\chi(T)$) measured on heating with and without an intermittent stop at T_s under an applied magnetic field of 100 Oe after ZFC run. T_s is 150 and 160 K.

Chapter 5: Structural, magnetic, and dielectric properties of multiferroic hexagonal TmFeO₃ nanoparticles

5.1. Introduction

Multiferroicity, which shows more than two ferroic order parameters in a single phase, has attracted great attention over the past decades.[1,2] In particular, materials with the coupling between ferroelectricity and any types of long-range magnetic ordering have been primarily studied due to their anticipated applications for spin transistors, sensors, and memory devices, where it is feasible to control dielectricity (magnetism) by using the magnetic (electric) field.[3,4] However, single-phase multiferroic materials are not so many because of the intrinsically mutual exclusive mechanism between magnetism and conventional displacive-type ferroelectricity.[5] Furthermore, most multiferroic materials with proper ferroelectric mechanism manifest the magnetoelectric (ME) effect in a low temperature region.[6,7] Thus, recent studies have focused on ferroelectricity *via* unconventional mechanisms such as the complicated lattice distortion, charge ordering, and spin ordering.[8]

Among numerous multiferroic materials with improper ferroelectricity, hexagonal rare-earth manganites (h-RMnO₃; R is a rare-earth element) have been extensively studied owing to their unique structure and physical properties like high-temperature ferroelectricity, a magnetically frustrated structure, and a strong ME coupling.[9–11] As is well known, the crystal structure of RMnO₃ is classified into two kinds of phases based on the radius of R cations. Perovskite phase with *Pbnm* emerges for large R (La-Dy),[6,12,13]

and on the other hand, RMnO$_3$ with small cations (Ho-Lu, Y, or Sc) belongs to hexagonal $P6_3cm$ phase.[14–16] Unlike orthomanganites, h-RMnO$_3$ consists of close-packed layers of [MnO$_5$] bipyramids which are separated along the c-axis by R layers and each atom is located on the triangular lattice in the ab-plane. Ferroelectricity is geometrically driven, where tilting of the [MnO$_5$] bipyramid unit eliminates a mirror image on the ab-plane and this phenomenon is associated with a strong hybridization between Y and O ions. [14–16] Magnetic property is dependent on the antiferromagnetic (AFM) order of Mn^{3+} spins that is oriented parallel to the ab-plane with a 120°spin structure and affected by the structural trimerization transition.[15,17–19] Unlike the expected strong ME coupling in h-RMnO$_3$ compounds, the actually observed ME coupling is small that is difficult for practical application because the magnetic ordering temperature is much lower than room temperature and Mn^{3+} spins are feebly coupled to its ferroelectric order. Alternatively, much higher magnetic ordering is anticipated for isostructural hexagonal ferrites (h-RFeO$_3$) owing to enhanced exchange interactions among Fe^{3+} ions,[20] the larger localized magnetic moments, and differences in the local electronic anisotropy between Mn^{3+} and Fe^{3+}.[21]

Unlike two distinct structural polymorphs observed in RMnO$_3$ compounds, only orthorhombic structure (o-RFeO$_3$, Figure 5.1 (a)) can be prepared by the conventional solid-state reaction regardless of the radii of R cations. Most o-RFeO$_3$ compounds are known to preclude ferroelectric property at room temperature except for the improper ferroelectricity in SmFeO$_3$.[22–24] On the other hand, metastable hexagonal RFeO$_3$ (h-RFeO$_3$, Figure 5.1 (b)) can be only obtained with small R cations (Sc, Y, or Ho-Lu) and

limited material processes such as growth of epitaxial thin films by low-pressure metal-organic chemical vapor deposition[25] and pulsed laser deposition,[26–29] nanoparticles through the spray-ICP technique[30] and sol-gel method,[31–33] bulk ceramics by containerless processing[34,35] and incorporation of other elements into Fe or R sites.[36–39] Furthermore, to my best of knowledge, most studies have been devoted to h-LuFeO$_3$ thin films and there exist only few reports on physical properties of h-RFeO$_3$ with other R elements. In the present study, I successfully synthesized h-TmFeO$_3$ nanoparticles and explored their magnetic and dielectric properties. I used the citrate sol-gel method for the preparation. In particular, though nano-sized materials might be suitable for application like miniaturization of electronic circuitry due to their high surface area, flexibility, and good directionality, the size effect on the multiferroic property is still unclear.[40,41] In this chapter, I confirmed that the calcination temperature is an important factor to stabilize the metastable hexagonal phase. The local structure and the chemical state of Fe in h-TmFeO$_3$ nanoparticle were investigated by Mössbauer spectroscopy. The magnetic and dielectric properties of the present nanocrystalline sample were measured and compared to those of h-RMnO$_3$ and h-LuFeO$_3$.

5.2. Sample fabrication

To synthesize single-phase h-TmFeO$_3$ nanoparticles, stoichiometric amounts of Tm(NO$_3$)$_3$·4H$_2$O (Mitsuwa Chemicals Co., Ltd., 99.9 %) and Fe(NO$_3$)$_3$·9H$_2$O (FUJIFILM Wako Pure Chemical Co., Ltd., 99.9 %) were taken as precursors and dissolved in deionized water. The transparent light orange solution was heated to 60℃

with continuous stirring and then mixed with citric acid monohydrate (FUJIFILM Wako Pure Chemical Co., Ltd., 99.5 %) as a chelating agent. In this case, the molar ratio of citric acid and metal nitrates was 2: 1. Afterward, the pH of the solution was adjusted to be neutralized by adding aqueous NH_3 drop by drop under constant stirring. The transparent sol was dried at 90℃ to form a dark green viscous gel and then the obtained gel was fired at 250℃ for 2 h to decompose the nitrates and remove the organic compounds. Finally, the resultant dark brown sponge-like products were sintered at 750℃ for 10 h to obtain red-brown h-TmFeO$_3$.

5.3. Characterization

X-ray diffraction (XRD) analysis with Cu Kα radiation was carried out on a four-circle Rigaku SmartLab diffractometer operating at 45 kV and 200 mA to examine the crystalline phase of the sample. High resolution scanning transmission electron microscopy (HR-STEM) images were acquired on a 300 keV ThermoScientific Titan[3] 60-300 with a double corrector, and energy-dispersive X-ray (EDX) analysis was performed by using Super-X detector. Mössbauer spectroscopy was conducted with a power sample at room temperature in transmission geometry using a [57]Co/Rh source. The velocity scale and the isomer shift were calibrated using α-Fe. The obtained spectra were least-squares fitted using the Lorentzian function. Magnetic measurements were carried out with a superconducting quantum interference device (SQUID) magnetometer (Quantum Design MPMS-SQUID). The temperature dependence of FC and ZFC magnetizations was measured at 100 Oe dc magnetic field over a range from 2 to 300 K.

Magnetization as a function of the magnetic field was measured at 3, 10, 100, and 200 K by applying magnetic fields up to ± 50 kOe. The dielectric properties were measured with an Agilent E4980A LCR meter at different frequencies. The powder sample was pelletized with a diameter of 10 mm and a thickness of 0.53 mm, and a silver electrode was attached to both sides of the pellet to make a capacitor geometry.

5.4. Results and discussion

The effect of calcination temperature on the crystalline phases of $TmFeO_3$ powder samples can be found in the XRD patterns illustrated in Figure 5.2 (a). It is known that general bulk $RFeO_3$ exists as the orthorhombic structure and to stabilize hexagonal phase is difficult in the bulk form compared to thin films. To obtain the single-phase of h-$TmFeO_3$, powders were sintered at various temperatures from 750 to 850 ℃. As shown in the figure, the calcination temperature plays a key role in stabilizing the metastable hexagonal phase. The single phase with the hexagonal structure was obtained at 750 ℃ and the mean size of the particles is calculated as about 13 nm by the Debye-Scherrer equation. Furthermore, the orthorhombic phase with *Pbnm* space group was observed when the calcination temperature was increased. In other words, as the temperature increases, the hexagonal structure transforms into the orthorhombic one that is the thermodynamically more stable. The diffraction peaks at 22.6°and 34.8°attributed to the *P6₃cm* symmetry for this composition are also observed in the enlarged XRD patterns of 20.0°- 26.0°and 32.5°- 36.0°ranges as illustrated in figure 5.2 (b). In particular, the (012) reflection indicates the tilting of [FeO₅] oxygen bipyramids[9,38] and is not allowed in the

centrosymmetric $P6_3/mmc$ space group. That is, h-TmFeO$_3$ nanoparticle prepared by the citrate sol-gel method belongs to the non-centrosymmetric $P6_3cm$ structure.

In order to clarify the shape and size of the present h-TmFeO$_3$ nanoparticles, HR-STEM was performed. As shown in figure 5.3 (a), products are composed of small agglomerated particles and the shape of individual crystallites is nearly square with a side length of about 25 nm (the inset of figure 5.3 (a)) that is somewhat larger than the value derived from XRD patterns. To investigate the elemental distribution, EDX scan elemental profiles were also obtained as given in figure 5.3 (b). The fraction of Tm and Fe is stoichiometric, which means that there is no loss of these elements during the preparation process. In addition, the density of the sample was determined by the Archimedes method to be about 78 % of the theoretical one.

Figure 5.4 shows the Mössbauer spectrum of nanocrystalline h-TmFeO$_3$ at room temperature. The spectrum exhibits a single doublet without any other sets of peaks, which is the evidence of one Fe site. The value of isomer shift (IS) of the doublet is 0.23 mm/s that corresponds to the value of Fe^{3+} (S = 5/2). Also, the observed single doublet suggests a good crystallinity of the present specimen because the reported h-RFeO$_3$ nanosized samples prepared by solution method showed two doublets resulting from the low crystallinity. The rather large quadrupole splitting (QS = 1.58 mm/s) is characteristic of bipyramid oxygen coordination of Fe^{3+} (FeO$_5$) and the value is similar to that of h-Lu$_{0.5}$Sc$_{0.5}$FeO$_3$ bulk previously reported.[36]

In the hexagonal RFeO$_3$ compounds, the antiferromagnetic (AFM) order of Fe^{3+} ions occurs at the Néel temperature (T_N) and it is known that the magnetic unit cell is consistent

with the crystallographic unit cell. The magnetic moments of Fe^{3+} are oriented at the angles of 120˚ within in-plane two-dimensional triangular networks.[16–19] Figure 5.5 (a) shows the temperature dependence of magnetizations (M-T curve, where M is the magnetization and T is the temperature.) of h-$TmFeO_3$ measured under dc 100 Oe magnetic field in the zero-field-cooled (ZFC) and field-cooled (FC) modes. The observed ZFC and FC magnetizations are similar to each other without bifurcation. The inset of figure 5.5 (a) depicts the temperature dependence of the inverse dc magnetic susceptibility ($1/\chi$), and the susceptibility diverges from the linear relation around 120 K. The phenomenon can be understood in terms of the onset temperature of magnetic ordering among Fe^{3+} ions within a short range in the present $TmFeO_3$. The downward deviation from the linear relation suggests that the magnetization is increased by spin-canting.[42,43] Fitting of the Curie-Weiss law, $\chi = C/(T - \Theta)$, to the data of paramagnetic states reveals that AFM interaction might be dominant among Fe^{3+} ions, because of the negative value of Weiss temperature ($\Theta = -51.7$ K) and the estimated degree of frustration is about 0.53, supposing that the ordering temperature is about 120 K. The value for the frustration is similar to that reported for h-$TmMnO_3$.[44] Additionally, the obtained effective magnetic moment is about 4.02 μ_B which is smaller than the spin-only value of the d^5 state of Fe^{3+}, μ_{eff} (Fe^{3+}) = 5.90 μ_B. The discrepancy between the experimental and theoretical magnetic moments might be due to the spin fluctuation near and above T_N by the strong geometrical frustration that produce a short-range magnetic correlation, which results in an increased slope of the inverse χ. [39] Also, the similar phenomenon was also observed in $YMnO_3$ nanoparticles, where the effective magnetic moment decreased with decreasing crystallite

size.[40]

The magnetic field dependence of magnetization (*M-H* loop, where *H* is the magnetic field.) was measured at temperatures of 3, 10, 100, and 200 K within up to ± 50 kOe. The results are shown in figure 5.5 (b). *M-H* loop at 200 K clearly shows a linear variation that is attributed to the typical paramagnetic behaviour. However, 100 K data also manifests a paramagnetic response despite the temperature lower than the observed T_N, which might indicate the large paramagnetic effect of Tm^{3+} ions. On the other hand, *M-H* curves at 3 and 10 K manifest a slight opening in the loop with an unsaturated magnetization that might be ascribed to weak ferromagnetism due to the Dzyaloshinskii-Moriya (DM) interaction among Fe^{3+} ions or Tm^{3+} spins in the *ab*-plane. [26, 45]

The dielectric properties of the present *h*-TmFeO$_3$ nanoparticle were investigated with the capacitor geometry. As shown in figure 5.6 (a), the dielectric constant (ε') exponentially decays as the frequency increases, indicating Debye-like relaxation. Unlike the monotonous variation of dielectric constant, the value of loss tangent (tan δ) decreases with increasing frequency up to about 10 kHz and increases with a peak around 100 kHz. The overall aspect is similar to the result of nanocrystalline *h*-LuFeO$_3$[33] except for the relatively lower dielectric constant and loss tangent in the present study and this discrepancy might be due to the extrinsic contributions like interfacial loss, oxygen deficiencies, or grain boundary defects. Also, the observed low dielectric constant can be explained in terms of the density of the present sample as mentioned above. Figure 5.6 (b) reveals dielectric constants measured at a temperature range from 4 to 300 K under 30 kHz. The dielectric constant decreases with decreasing temperature with an anomaly

around magnetic transition temperature (T_N). Other isostructural materials[33,36,37,46,47] also exhibited a dielectric anomaly which is observed with the electric field along the *ab*-plane but is absent along the *c*-axis,[46] confirming a strong spin-lattice coupling and a consequent magnetoelecric coupling. It is speculated that a characteristic coupling occurs between ferroelectric and antiferromagnetic order parameters at T_N in the present *h*-TmFeO$_3$ nanoparticle.

5.5. Conclusion

Nanocrystalline hexagonal TmFeO$_3$ (*h*-TmFeO$_3$) was synthesized through the citrate sol-gel method and its magnetic and dielectric properties were investigated. The XRD results reveal that the product calcined at 750℃ shows a single phase which belongs to the polar *P*6$_3$*cm* space group. The sample is composed of small square-shaped agglomerated particles with about 25 nm side size and the almost stoichiometric ratio of Tm to Fe was confirmed by EDX scan elemental profiles. Mössbauer spectroscopy proves that there is one Fe site in the present nanoparticle. A short-range antiferromagnetic transition was demonstrated by the negative Weiss temperature below about 120 K, which is considered to be the 120° ordering of Fe^{3+} spins within two-dimensional triangular lattices. Besides, the nonlinear behaviour of magnetization at low temperatures (3 and 10 K) suggested that a weak ferromagnetic ordering among Fe^{3+} ions or Tm^{3+} ions might arise from the Dzyalonshinskii-Moriya interaction. Furthermore, a dielectric constant anomaly was observed around the magnetic transition temperature, which can be ascribed to the magnetoelectric coupling at this temperature.

References in chapter 5

1. N. A. Spaldin and M. Fiebig, *Science*, 2005, **309**, 391–392.

2. K. F. Wang, J.-M. Liu and Z. F. Ren, *Adv. Phys.*, 2009, **58**, 321–448.

3. W. Eerenstein, N. D. Mathur and J. F. Scott, *Nature*, 2006, **442**, 759–765.

4. J. F. Scott, *Nat. Mater.*, 2007, **6**, 256–257.

5. N. A. Hill, *J. Phys. Chem. B*, 2000, **104**, 6694–6709.

6. T. Kimura, T. Goto, H. Shintani, K. Ishizaka, T. Arima and Y. Tokura, *Nature*, 2003, **426**, 55–58.

7. H. J. Zhao, X. Q. Liu, X. M. Chen and L. Bellaiche, *Phys. Rev. B*, 2014, **90**, 195147.

8. N. A. Spaldin and R. Ramesh, *Nat. Mater.*, 2019, **18**, 203–212.

9. A. S. Gibbs, K. S. Knight and P. Lightfoot, *Phys. Rev. B*, 2011, **83**, 094111.

10. S. Picozzi and C. Ederer, *J. Phys.: Condens. Matter*, 2009, **21**, 303201.

11. D. Khomskii, *Physics*, 2009, **2**, 20.

12. A. A. Belik, T. Furubayashi, Y. Matsushita, M. Tanaka, S. Hishita and E. Takayama-Muromachi, *Angew. Chem. Int. Ed.*, 2009, **48**, 6117–6120.

13. H. Katsura, N. Nagaosa and A. V. Balatsky, *Phys. Rev. Lett.*, 2005, **95**, 057205.

14. B. B. Van Aken, T. T. M. Palstra, A. Filippetti and N. A. Spaldin, *Nat. Mater.*, 2004, **3**, 164–170.

15. C.-Y. Ren, *Phys. Rev. B*, 2009, **79**, 125113.

16. H. Lueken, *Angew. Chem. Int. Ed.*, 2008, **47**, 8562–8564.

17. T. Katsufuji, M. Masaki, A. Machida, M. Moritomo, K. Kato, E. Nishibori, M. Takata, M. Sakata, K. Ohoyama, K. Kitazawa, K. Kitazawa and H. Takagi, *Phys. Rev. B*, 2002,

66, 1344341–1344348.

18. X. Fabrèges, S. Petit, I. Mirebeau, S. Pailhès, L. Pinsard, A. Forget, M. T. Fernandez-Diaz and F. Porcher, *Phys. Rev. Lett.*, 2009, **103**, 067204.

19. M.-A. Oak, J.-H. Lee, H. M. Jang, J. S. Goh, H. J. Choi and J. F. Scott, *Phys. Rev. Lett.*, 2011, **106**, 047601.

20. H. Das, A. L. Wysocki, Y. Geng, W. Wu and C. J. Fennie, *Nat. Commun.*, 2014, **5**, 1-11.

21. A. R. Akbashev, A. S. Semisalova, N. S. Perov and A. R. Kaul, *Appl. Phys. Lett.*, 2011, **99**, 122502.

22. R. L. White, *J. Appl. Phys.*, 1969, **40**, 1061–1069.

23. M. Marezio, J. P. Remeika and P. D. Dernier, *Acta Crystallogr. B*, 1970, **26**, 2008–2022.

24. J.-H. Lee, Y. K. Jeong, J. H. Park, M.-A. Oak, H. M. Jang, J. Y. Son and J. F. Scott, *Phys. Rev. Lett.*, 2011, **107**, 117201.

25. A. A. Bossak, I. E. Graboy, O. Y. Gorbenko, A. R. Kaul, M. S. Kartavtseva, V. L. Svetchnikov and H. W. Zandbergen, *Chem. Mater.*, 2004, **16**, 1751–1755.

26. S. M. Disseler, J. A. Borchers, C. M. Brooks, J. A. Mundy, J. A. Moyer, D. A. Hillsberry, E. L. Thies, D. A. Tenne, J. Heron, M. E. Holtz, D. G. Schlom and W. D. Ratcliff, *Phys. Rev. Lett.*, 2015, **114**, 217602.

27. Y. K. Jeong, J.-H. Lee, S.-J. Ahn and H. M. Jang, *Chem. Mater.*, 2012, **24**, 2426–2428.

28. J. A. Moyer, R. Misra, J. A. Mundy, C. M. Brooks, J. T. Heron, D. A. Muller, D. G.

Schlom and P. Schiffer, *APL Mater.*, 2014, **2**, 012106.

29. S.-J. Ahn, J.-H. Lee, H. M. Jang and Y. K. Jeong, *J. Mater. Chem. C*, 2014, **2**, 4521–4525.

30. Y. Mizoguchi, H. Onodera, H. Yamauchi, M. Kagawa, Y. Syono and T. Hirai, *Mater. Sci. Eng. A*, 1996, **A217/218**, 164–166.

31. J. Li, U. G. Singh, T. D. Schladt, J. K. Stalick, S. L. Scott and R. Seshadri, *Chem. Mater.*, 2008, **20**, 6567–6576.

32. L. J. Downie, R. J. Goff, W. Kockelmann, S. D. Forder, J. E. Parker, F. D. Morrison and P. Lightfoot, *J. Solid State Chem.*, 2012, **190**, 52–60.

33. P. Suresh, K. Vijaya Laxmi, A. K. Bera, S. M. Yusuf, B. L. Chittari, J. Jung and P. S. Anil Kumar, *Phys. Rev. B*, 2018, **97**, 184419.

34. A. Masuno, S. Sakai, Y. Arai, H. Tomioka, F. Otsubo, H. Inoue, C. Moriyoshi, Y. Kuroiwa and J. Yu, *Ferroelectrics*, 2009, **378**, 169–174.

35. E. Magome, C. Moriyoshi, Y. Kuroiwa, A. Masuno and H. Inoue, *Jpn. J. Appl. Phys.*, 2010, **49**, 09ME06.

36. A. Masuno, A. Ishimoto, C. Moriyoshi, N. Hayashi, H. Kawaji, Y. Kuroiwa and H. Inoue, *Inorg. Chem.*, 2013, **52**, 11889–11894.

37. L. Lin, H. M. Zhang, M. F. Liu, S. Shen, S. Zhou, D. Li, X. Wang, Z. B. Yan, Z. D. Zhang, J. Zhao, S. Dong and J.-M. Liu, *Phys. Rev. B*, 2016, **93**, 075146.

38. J. Liu, T. L. Sun, X. Q. Liu, H. Tian, T. T. Gao and X. M. Chen, *Adv. Funct. Mater.*, 2018, **28**, 1706062.

39. S. M. Disseler, X. Luo, B. Gao, Y. S. Oh, R. Hu, Y. Wang, D. Quintana, A. Zhang,

Q. Huang, J. Lau, S.-W. Cheong and W. Ratcliff, *Phys. Rev. B*, 2015, **92**, 054435.

40. K. Bergum, H. Okamoto, H. Fjellvåg, T. Grande, M.-A. Einarsrud and S. M. Selbach, *Dalt. Trans.*, 2011, **40**, 7583–7589.

41. T.-C. Han, W.-L. Hsu and W.-D. Lee, *Nanoscale Res. Lett.*, 2011, **6**, 201.

42. A. Muñoz, J. A. Alonśo, M. J. Martínez-Lope, M. T. Casáis, J. L. Martínez and M. T. Fernández-Díaz, *Phys. Rev. B*, 2000, **62**, 9498–9510.

43. K. Yoshii and H. Abe, *J. Solid State Chem.*, 2002, **165**, 131–135.

44. E. S. Stampler, W. C. Sheets, W. Prellier, T. J. Marks and K. R. Poeppelmeier, *J. Mater. Chem.*, 2009, **19**, 4375–4381.

45. B. Raneesh, A. Saha, D. Das and N. Kalarikkal, *J. Alloys Compd.*, 2013, **551**, 654–659.

46. T. Katsufuji, S. Mori, M. Masaki, Y. Moritomo, N. Yamamoto and H. Takagi, *Phys. Rev. B*, 2001, **64**, 1044191–1044196.

47. D. G. Tomuta, S. Ramakrishnan, G. J. Niewenhuys and J. A. Mydosh, *J. Phys.: Condens. Matter*, 2001, **13**, 4543–4552.
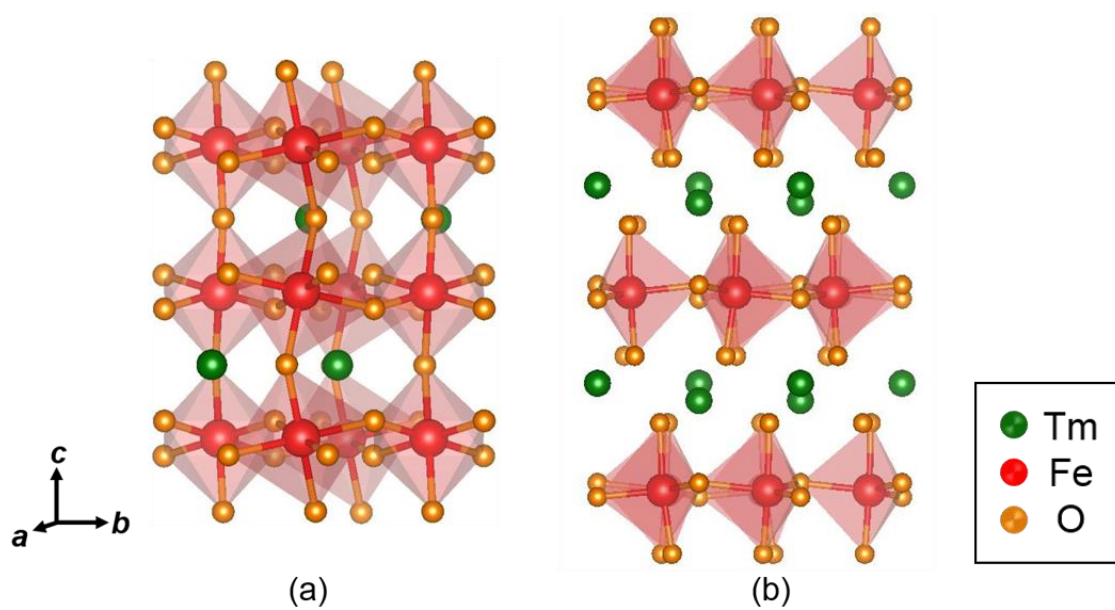
Figure 5.1. Schematic illustration of two $TmFeO_3$ structures. (a) The orthorhombic structure with *Pbnm* space group, where the red octahedra and green spheres represent FeO_6 polyhedra and Tm^{3+}, respectively. (b) The hexagonal structure with *P6₃cm* symmetry, where the red trigonal bipyramids and green spheres depict FeO_5 polyhedra and Tm^{3+} ions, respectively.
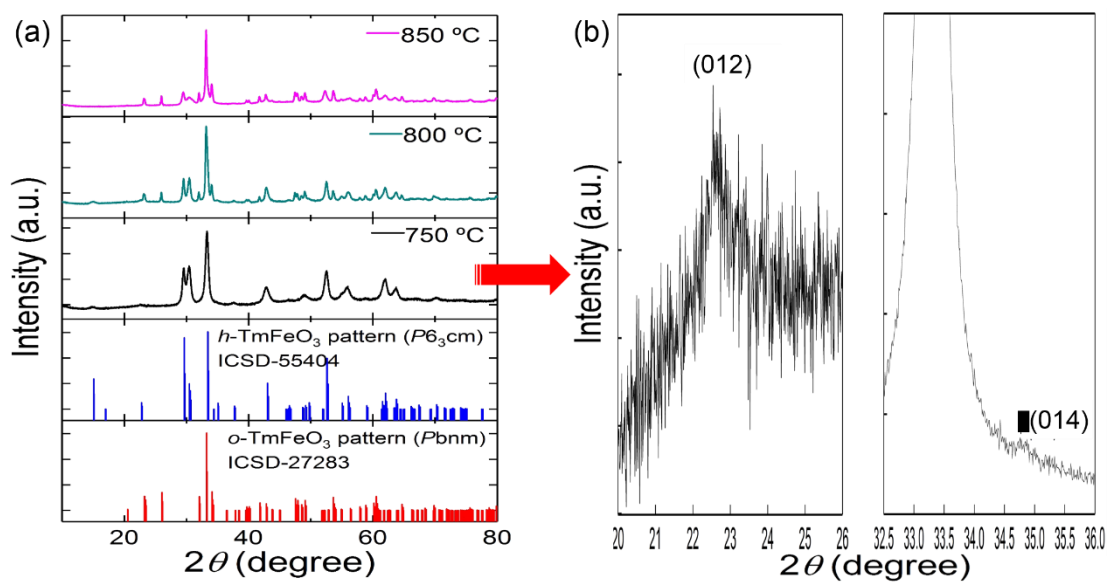
Figure 5.2. (a) XRD profiles for *h*-TmFeO₃ nanoparticles calcined at various temperatures from 750 to 850 ℃. Theoretical XRD patterns for hexagonal and orthorhombic TmFeO₃ are displayed as reference. (b) The enlarged XRD patterns of (012) and (014) Bragg reflections that are only allowed in *P6₃cm* symmetry for the sample sintered at 750℃.
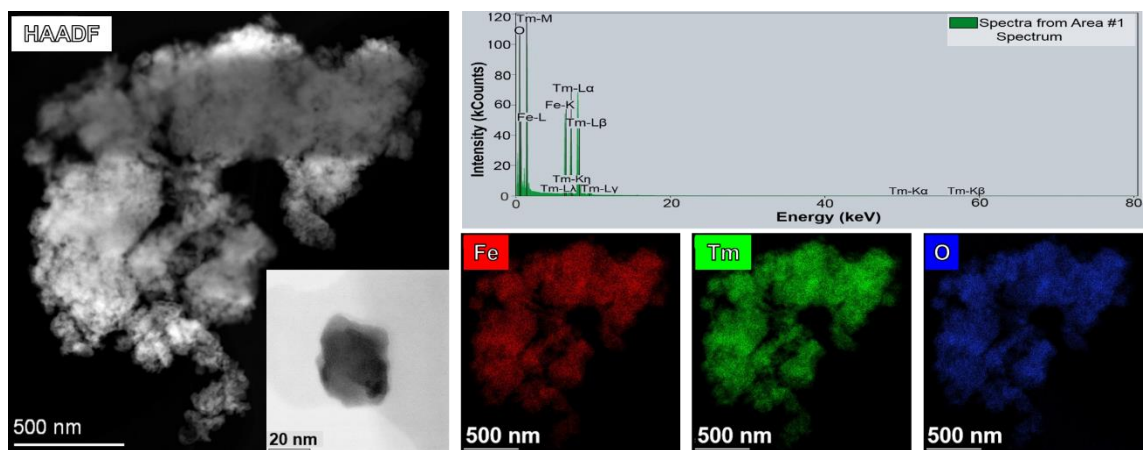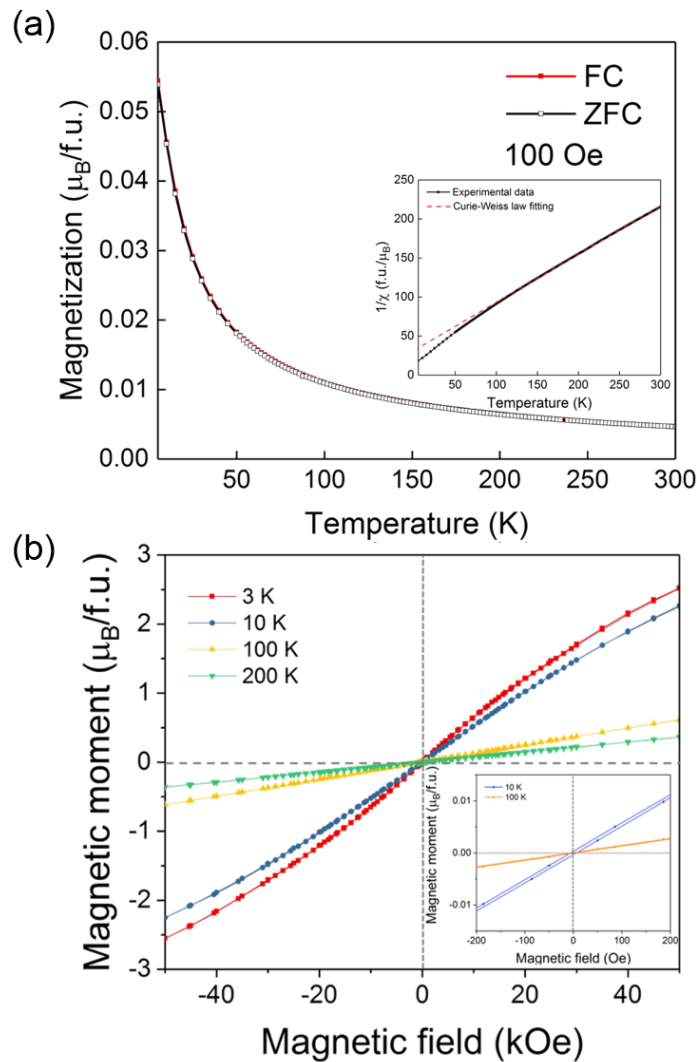
Figure 5.3. HAADF-STEM image of nanocrystalline TmFeO$_3$ and EDX elemental mapping images and spectrum of Fe, Tm, and O. The inset of HAADF image is correspond to the micrograph of individual crystallite with the size of about 25 nm.
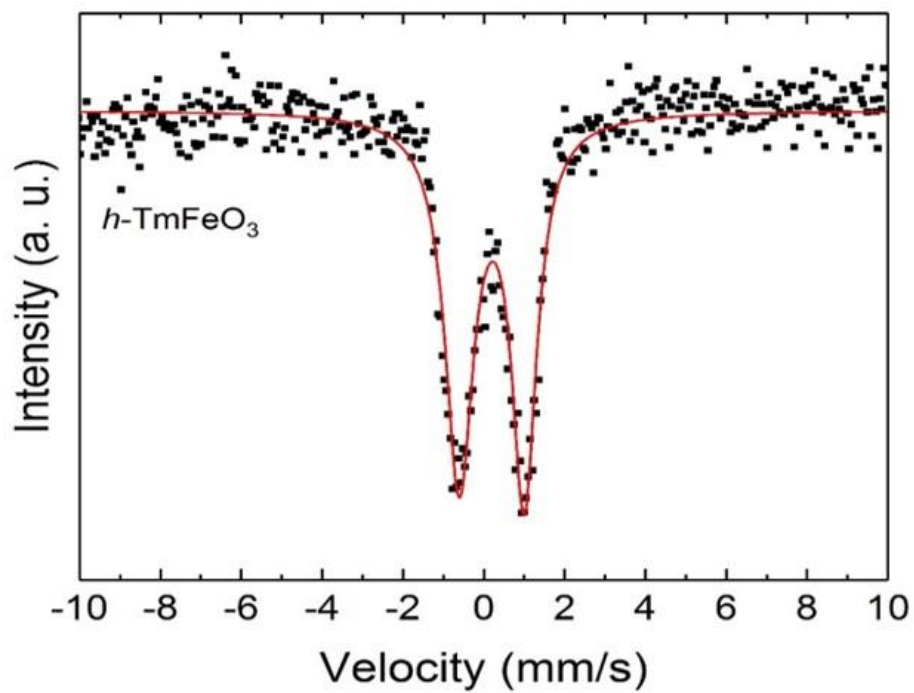
Figure 5.4. [57]Fe Mössbauer spectrum (filled squares) at room temperature and the fitting result (red line) of *h*-TmFeO$_3$ nanoparticle.

Figure 5.5. Magnetic properties of the nanocrystalline *h*-TmFeO₃. (a) The temperature

dependence of zero-field-cooled (ZFC, hollow red symbols) and field-cooled (FC, filled

red symbols) magnetizations measured by applying 100 Oe of dc magnetic field. The

inset shows the temperature dependence of inverse magnetic susceptibility and the data

was fitted by the Curie-Weiss law as indicated by the dotted red line. (b) The magnetic

field dependence of magnetizations measured at various temperatures (3, 10, 100, and

200 K). The inset illustrates the enlarged *M-H* loops measured at 10 and 100 K.
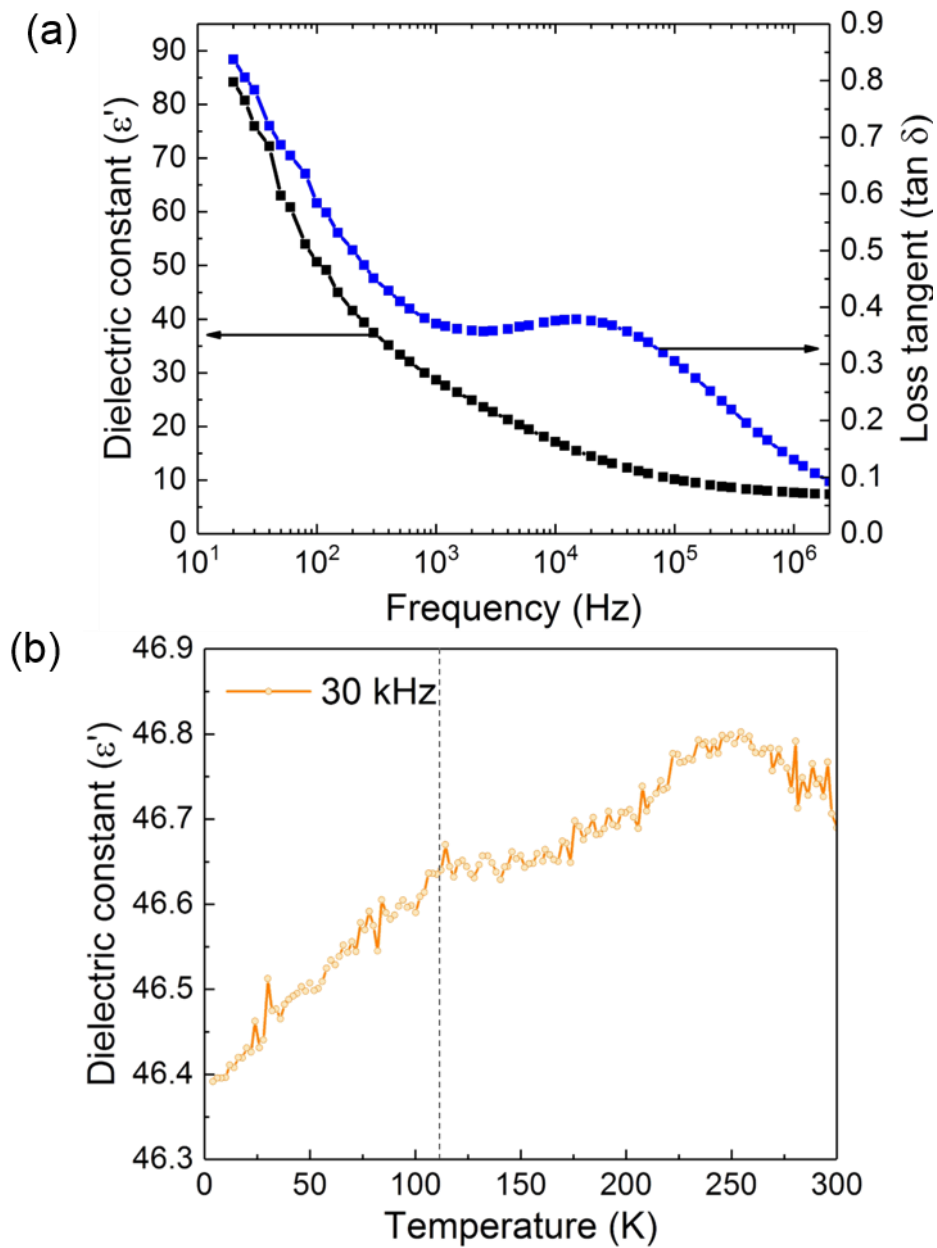
Figure 5.6. Dielectric properties of *h*-TmFeO$_3$ nanoparticles. (a) Frequency dependence of dielectric constant and loss tangent. (b) Dielectric constant at 30 kHz. The dashed line corresponds to the magnetic transition temperature.

Summary

In the present thesis, I have focused on the synthesis and magnetic properties of layered rare-earth ferrites, especially $R\mathrm{Fe_2O_4}$ (R= Lu, Tm) thin films, $\mathrm{TmFe_2O_4}$ single crystal, and hexagonal $\mathrm{TmFeO_3}$ (h-$\mathrm{TmFeO_3}$) nanoparticles as candidates for new functional metal oxide materials. $R\mathrm{Fe_2O_4}$ (R = Sc, Y, In, and Dy to Lu) has attracted great attention because of their interesting dielectric and magnetic phenomena caused by the charge ordering among equal number of $\mathrm{Fe^{2+}}$ and $\mathrm{Fe^{3+}}$ ions, coupled with the spin degree of freedom. Also, each iron ion is located in a triangular lattice, leading to rather complicated ground states of charge and spin structures due to the geometrical frustration. The spin structure of those materials is considered as an Ising system because $\mathrm{Fe^{2+}}$ and $\mathrm{Fe^{3+}}$ ions in the high spin states exhibit a strong anisotropy along the c_{Hex}-axis. Among $R\mathrm{Fe_2O_4}$ family, most studies have been devoted to bulk $\mathrm{LuFe_2O_4}$ materials thus far; numerous papers have been published concerning the structure and physical properties like magnetism, dielectricity, and electrical conductivity. In addition, there exist few reports on the details of preparation and physical properties of $R\mathrm{Fe_2O_4}$ thin films except for $\mathrm{LuFe_2O_4}$. Hence, I have carried out detailed investigations on the synthesis to magnetic properties of $\mathrm{LuFe_2O_4}$ and $\mathrm{TmFe_2O_4}$ thin films. In particular, I found that an unique interface structure with a self-assembled h-$R\mathrm{FeO_3}$-like phase is generated between $R\mathrm{Fe_2O_4}$ thin film and YSZ substrate, which has a significant influence on the magnetic properties never observed in bulk counterparts. On top of that, I also have explored the magnetic properties of single-crystalline $\mathrm{TmFe_2O_4}$ and nanocrystalline h-$\mathrm{TmFeO_3}$ because these studies are

necessary to further understand the observed magnetic phenomena in the present $TmFe_2O_4$ thin film. The results obtained through the present investigation are summarized as follows.

In chapter 1, the outline of multiferroics was briefly reviewed, in particular, the structure and properties of multiferroic materials that is originated from the improper ferroelectric mechanism, which might be a key for strong magnetoelectric coupling, were mainly stated. In addition, the theoretical and experimental background for structure and physical properties of rare-earth ferrites (RFe_2O_4 and $h\text{-}RFeO_3$) were described and the recent progress in related studies was summarized based on their interesting properties as mentioned above.

In chapter 2, the epitaxial $LuFe_2O_4$ thin film was prepared by the PLD method and their structure, magnetic property, and electric conductivity were investigated. The epitaxial relationship between $LuFe_2O_4$ phase and YSZ substrate was confirmed by out-of-plane XRD pattern and the interesting interface structure composed of very thin layers of $h\text{-}LuFeO_3$-like and $Lu_2Fe_3O_7$-like phases was confirmed through HAADF-STEM image and EDX spectrometry. The exact reason for the occurrence of interface structure is unclear, but the very thin layers might be act as a buffer layer, considering the lattice mismatching between the layered lutetium ferrites and YSZ substrate. In addition, the present interface structure induces a large exchange bias effect at 100 K that might be due to the spin competition between different phases. On the other hand, $LuFe_2O_4$ phase itself shows a ferrimagnetic transition around 236 K and spin or cluster glass behaviour below 220 K. For the electrical resistivity, the Arrhenius-type scheme is converted into the Mott-

VRH mechanism at the three-dimensional charge ordering temperature.

In chapter 3, epitaxial thin film of $TmFe_2O_4$, another compound of RFe_2O_4 family, was fabricated on YSZ substrate and an anomalous interface structure was explored at atomistic level. In the interface region, h-$TmFeO_3$-like phase was observed between $TmFe_2O_4$ thin film and YSZ substrate with Tm^{3+}-rich region at the upper side of the substrate, and the results of EEL spectra revealed that some iron and oxygen defects might be generated in the interface region at the early stage of deposition of $TmFe_2O_4$. That is, h-$TmFeO_{3-\delta}$ and $TmFe_2O_{4-\delta}$ phases are formed in the present thin film. Interestingly, this interface structure leads to an intrinsic exchange bias effect at 100 K due to the different magnetic structures of $TmFe_2O_4$ and h-$TmFeO_{3-\delta}$. In addition, $TmFe_2O_{4-\delta}$ itself manifests spin or cluster glass transition, as verified by the fact that the external magnetic field dependence of irreversible transition temperature follows the de Almeida-Thouless line as well as the clearly observed aging-memory effect.

In chapter 4, single-crystalline $TmFe_2O_{4-\delta}$ proved to be categorized as a spin glass system by examining not only ac magnetic susceptibility but also aging-memory and rejuvenation effect. The present $TmFe_2O_{4-\delta}$ develops a long-range magnetic ordering around 240 K and reenters into the spin glass state at 186.2 K, as demonstrated by a maximum of ZFC curve in its temperature dependence and the variation of spin-freezing temperature with frequency of ac magnetic field. Furthermore, clear aging-memory and rejuvenation effects are also observed below the spin-freezing temperature. These facts suggest that the $TmFe_2O_{4-\delta}$ can be regarded as a reentrant spin glass system. The spin glass behaviour stems from the increased degree of spin frustration attributed to the

situation that Fe^{2+} ions outnumber Fe^{3+} ions in a two-dimensional triangular lattice by the oxygen deficiencies.

In chapter 5, nanocrystalline h-TmFeO$_3$ was synthesized by a citrate sol-gel method and its magnetic and dielectric properties were investigated. XRD result indicates that the single phase of h-TmFeO$_3$ having a hexagonal crystal structure with $P6_3cm$ space group can be obtained at the calcination temperature of 750℃ and a further increase of temperature leads to the formation of orthorhombic phase that is the thermodynamically stable phase of this compound. In this regard, the calcination temperature is a critical key for obtaining the metastable hexagonal phase. The magnetic characterization reveals that an antiferromagnetic ordering of the Fe^{3+} sublattices occurs in the present h-TmFeO$_3$ nanoparticles with a Nėel temperature of about 120 K and a negative Weiss temperature of -51.7 K. In addition, a narrow hysteresis loop at low temperatures, like 3 and 10 K, might be associated with weak ferromagnetism due to the DM interaction among Fe^{3+} ions. A dielectric constant anomaly was also observed around the magnetic transition temperature, suggesting the magnetoelectric coupling below this temperature.

List of publications

Chapter 2

"Magnetic and electrical properties of $LuFe_2O_4$ epitaxial thin films with a self-assembled interface structure"

<u>You Jin Kim</u>, Shinya Konishi, Yuichiro Hayasaka, Itsuhiro Kakeya, and Katsuhisa Tanaka

CrystEngComm, 2020, **22**, 1096-1105.

Chapter 3

"Magnetic properties of epitaxial $TmFe_2O_4$ thin film with anomalous interface structure"

<u>You Jin Kim</u>, Shinya Konishi, Yuichiro Hayasaka, Ryo Ohta, Ryosuke Tomozawa, Katsuhisa Tanaka

J. Mater. Chem. C, 2020, in press.

DOI: https://doi.org/10.1039/D0TC01367F

Chapter 4

"Spin glass transition of single-crystalline $TmFe_2O_{4-\delta}$"

<u>You Jin Kim</u>, Shinya Konishi, Mari Okada, Mai Komabuchi, Daisuke Urushihara, Toru Asaka, Katsuhisa Tanaka

J. Phys.: Condens. Matter, 2020, **32**, 405801.

Acknowledgements

The present thesis has been carried out under the direction of Professor Katsuhisa Tanaka at Graduate School of Engineering, Kyoto University.

First of all, I would like to give my deepest gratitude to my supervisor Professor Katsuhisa Tanaka, who gives me constant encouragement and valuable comments all through the duration of the present work. Without his caring and support, I could not be able to accomplish my doctoral study. I also thank to assistant professor Shunsuke Murai for his valuable discussions and helpful assistances.

I deeply grateful to Mr. Shinya Konishi and Mr. Yuichiro Hayasaka for his experimental support for scanning transmission electron microscopy and fruitful discussions. The observed new experimental results are really valuable to discuss physical properties and present the way of this research. I also appreciate to professor Itsuhiro Kakeya for his experimental support for electric transport measurements, magnetic measurements under high magnetic field, and informative discussions. I express my gratitude to the member of the Tanaka laboratory for their assistance and everyday activities.

I sincerely appreciate Japanese government for giving me the opportunity of doctoral course and financial support (MEXT scholarship).

Finally, I would like to greatly thank my family for their support from my back, understanding, and hearty encouragements.

Kyoto, 2020. 06

You Jin Kim